Conversion of a Kerosene-Fuelled Gas Turbine to Run on Propane

by

David Anthony Marsh

Thesis presented in partial fulfilment of the requirements for the degree of Master of Engineering (Mechanical) in the Faculty of Engineering at Stellenbosch University

Supervisor: Prof. T.W. von Backström

Co-supervisor: Mr. R.W. Haines

April 2019

Declaration

By submitting this thesis electronically, I declare that the entirety of the work contained therein is my own, original work, that I am the sole author thereof (save to the extent explicitly otherwise stated), that reproduction and publication thereof by Stellenbosch University will not infringe any third party rights and that I have not previously in its entirety or in part submitted it for obtaining any qualification.

Date: .... April 2019

Plagiarism Declaration

1. Plagiarism is the use of ideas, material and other intellectual property of another's work and to present it as my own.

2. I agree that plagiarism is a punishable offence because it constitutes theft.

3. I also understand that direct translations are plagiarism.

4. Accordingly all quotations and contributions from any source whatsoever (including the internet) have been cited fully. I understand that the reproduction of text without quotation marks (even when the source is cited) is plagiarism.

5. I declare that the work contained in this assignment, except where otherwise stated, is my original work and that I have not previously (in its entirety or in part) submitted it for grading in this module/assignment or another module/assignment.

Abstract

This study forms part of a greater research objective to use air as a heat transfer fluid, and a combined gas and steam cycle in a concentrated solar power plant. Combustion will be used to compensate for solar fluctuations.

The conversion of a Rover 1S/60 gas turbine to run on propane was completed in this study. In a previous study, the Rover gas turbine was run on jet fuel with standard hardware, before being converted to run on LPG at low speed. In this study, the fuel control system was improved for easier throttle control, and for a higher fuel consumption rate. The gas turbine was successfully run on propane at full speed and 77 % of rated power, which is close to the performance previously achieved with jet fuel (88 % of rated power). The power output was constrained by the exhaust gas temperature (EGT) limit.

According to the engine specifications, the power produced with jet fuel and propane was low compared to the EGT and fuel consumption. A few external factors were considered, but the condition of the gas turbine was considered to be the primary cause. Besides this limitation, the conversion was considered a success, and the gas turbine ran well on propane.

A general method for the conversion of a gas turbine from liquid to gaseous fuel was proposed. The method was used to review the conversion of the Rover gas turbine. The conversion was satisfactory within the project scope. The fuel control system requires manual operation and steady load, which was suitable for engine testing. The system could be automated for a broader range of application. For example, in a concentrated solar power plant.

A CFD model was used to compare the cold (non-reacting) flow of the combustion chamber (combustor) with the original liquid atomiser to that with the custom gas injector. The model indicates that the conversion has resulted in significantly different flow, which could affect the flame tube cooling. Without any apparent benefit from the change in flow, it is recommended to modify the gas injector to match the combustor flow with the original atomiser.

Uittreksel

Hierdie studie maak deel uit van 'n groter navorsingsoogmerk om lug as 'n hitteoordragvloeistof te gebruik en die werking van 'n gekombineerde gas- en stoomsiklus in 'n gekonsentreerde sonkragaanleg te ondersoek. Verbranding sal gebruik word om vir wisseling in sonkrag te vergoed.

In hierdie studie is 'n 1S/60 Rover-gasturbine omskep om op propaan te loop. In 'n vorige studie is die Rover-gasturbine met stralerbrandstof en standaardhardeware aangedryf voordat dit omskep is om op vloeibare petroleumgas teen 'n lae spoed te loop. In hierdie studie is die brandstofbeheerstelsel verbeter vir makliker versnellerbeheer en 'n beter brandstofverbruikkoers. Op propaan het die gasturbine suksesvol teen volspoed en 77 % van aangeslane vermoë geloop, wat na aan die werkverrigting is wat voorheen met stralerbrandstof verkry is (88 % van aangeslane vermoë). Die kraglewering is aan bande gelê deur die uitlaatgastemperatuur- (UGT-) perk.

Volgens die enjinspesifikasies was die kraglewering wat met stralerbrandstof en propaan verkry is laag vergeleke met die UGT en brandstofverbruik. 'n Paar eksterne faktore is oorweeg, hoewel die toestand van die gasturbine as die hoofoorsaak beskou is. Afgesien van hierdie beperking, was die omskakeling 'n sukses en het die gasturbine goed op propaan geloop.

'n Algemene metode vir die omskakeling van 'n gasturbine van vloeibare tot gasbrandstof is voorgestel. Die metode is gebruik om die omskakeling van die Rover-gasturbine te beoordeel. Die omskakeling was bevredigend binne die projekomvang. Die brandstofbeheerstelsel vereis handbediening en 'n konstante las, wat geskik was vir enjintoetsing. Die stelsel kan ook vir 'n groter verskeidenheid toepassings geoutomatiseer word, waaronder 'n gekonsentreerde sonkragaanleg.

'n Berekeningsvloeidinamikamodel is gebruik vir 'n vergelyking tussen die koue (nie-reaktiewe) vloei van die verbrandingskamer (verbrander) met die oorspronklike vloeistofverstuiwer, en dié met die pasgemaakte gasinspuiter. Die model dui daarop dat die omskakeling 'n aansienlike verandering in vloei teweeggebring het, wat die vuurbuisverkoeling kan beïnvloed. Aange-

sien die verandering in vloei geen duidelike voordeel inhou nie, word daar aanbeveel dat die gasinspuiter aangepas word om met die verbrandervloei met die aanvanklike verstuiwer ooreen te stem.

Contents

List of Figures

List of Tables

Nomenclature

Abbreviations

CFD   computational fluid dynamics

CSP   concentrating solar power

EDM   eddy dissipation model

EGT   exhaust gas temperature

ETA   engine test automation

CNG   compressed natural gas

HHV   higher heating value (water in liquid phase)

LHV   lower heating value (water in vapour phase)

LNG   liquefied natural gas

LPG   liquefied petroleum gas

MAC   main air casing

NO_x nitrogen oxides

OAC   outer air casing

PLC   programmable logic controller

SO_x sulphur oxides

STERG   solar thermal energy research group

TIT   turbine inlet temperature

UHC   unburned hydrocarbons

Constants

$g = 9.81 \, \text{m/s}^2$ gravitational acceleration

$\bar{R} = 8.314 \, \text{kJ/kmol K}$ universal gas constant

Roman symbols

A	area	$[\text{m}^2]$
D	diameter	$[\text{m}]$
d	diameter	$[\text{m}]$
C	coefficient	$[-]$
c_p	constant pressure specific heat	$[\text{kJ/kg K}]$
c_v	constant volume specific heat	$[\text{kJ/kg K}]$
E	energy	$[\text{kJ}]$
f	fuel-air ratio	$[-]$
h	specific enthalpy	$[\text{kJ/kg}]$
K	coefficient	$[-]$
M	molecular weight	$[\text{kg/kmol}]$
$\dot{m}$	mass flow-rate	$[\text{kg/s}]$
Ma	Mach number	$[-]$
n	engine speed, or	$[\text{RPM}]$
	polytropic constant	$[-]$

p	pressure	[kPa]
$\dot{Q}$	heat transfer rate	[kW]
q_f	calorific value	[MJ/kg]
R	gas constant	[kJ/kg K]
r	pressure ratio	[−]
Re	Reynolds number	[−]
S	sample standard deviation	[−]
SFC	specific fuel consumption	[kg/kW h]
T	temperature	[K]
t	time	[s]
U	impeller tip velocity	[m/s]
u	specific internal energy	[kJ/kg]
V	volume	[m^3]
v	velocity	[m/s]
$\dot{W}$	power	[kW]
w	specific power	[kJ/kg]
WI	Wobbe index	[MJ/m^3]
Y	compressibility factor	[−]

Greek symbols

$\alpha\varepsilon$	compound coefficient	[−]
β	diameter ratio	[−]
γ	specific heat ratio	[−]

η efficiency . . . . [%]

ρ density . . . . [kg/m^3]

σ slip factor . . . . [−]

τ torque . . . . [N m]

ϕ equivalence ratio . . . . [−]

ψ power input factor . . . . [−]

ω angular velocity . . . . [rad/s]

Subscripts and superscripts

a air, or ambient

b combustor

c compressor, or contraction

d discharge, or dynamic

f fuel

g combustion gases

L loss

m mechanical

t turbine

th theoretical

0 stagnation state

25 reference temperature of 25 °C

Auxillary symbols

$\square'$ isentropic process, e.g. T_2'

$\overline{\square}$ arithmetic mean

1. Introduction

The Solar Thermal Energy Research Group (STERG), at Stellenbosch University, is developing a Concentrating Solar Power (CSP) system, which incorporates a combined gas and steam cycle. The system is referred to as the SUNSPOT cycle, in which a gas turbine supplies compressed air to a solar thermal receiver. Combustion will regulate the air temperature due to solar fluctuations, before generating shaft power via the gas turbine. The hot exhaust gases are either used to generate steam to power a steam turbine, or to store thermal energy in a rock bed for later use (Kröger, 2012). Several studies have been done on the utilisation of a Rover 1S/60 gas turbine with a solar receiver. Related to this research, Zhang (2016) ran a Rover 1S/60 gas turbine on jet fuel with standard hardware, before converting it to run on LPG at low speed.

1.1   Problem statement

General combustion knowledge will be required to adapt a gas turbine for the SUNSPOT cycle. Especially to deal with the variable rate of heat supplied by the solar receiver.

The Rover engine performance was limited by the LPG conversion, and the fuel controls had limitations. LPG is a mixture of propane and butane, where the concentration of propane can be increased to achieve higher vapour pressure of the mixture. Further work was required to get the engine to perform as it did on jet fuel with the original fuel system. The ultimate goal is to run the engine on biogas.

1.2   Objectives

- Determine a methodology for the conversion of a gas turbine from liquid to gaseous fuel.
- Improve the performance of the Rover 1S/60 gas turbine fuelled with LPG/propane to match the jet fuel results.

1.3   Project scope

The conversion methodology was intended to be generalised. However, the conversion of the Rover was a key objective, and successful conversion of the

Rover engine is not an indication that the method is universally appropriate. Consideration needs to be given to the low power, low pressure and simple combustor of the Rover engine.

It was beyond the scope of the project to evaluate the merits of fuel conversion; notably emissions, economy, temperature profile, and combustion quality. Although these may be mentioned.

This project did not address the requirements to run the Rover as an industrial gas turbine, although that might be the longer term goal. Instead the test bench facilities were used to meet the performance objective.

The success of the Rover conversion was evaluated on performance indicators such as engine speed, power output, exhaust gas temperature and fuel efficiency, as those measurements were available.

1.4   Motivation

Solar power production is limited by sunlight fluctuations and daylight hours. In the SUNSPOT cycle, combustion between the solar receiver and the gas cycle turbine is used to smooth out the short term fluctuations due to clouds, or even the occasionally longer interruptions, such as a few days of rain. This will make the power supply more dependable, and hence more competitive as a source of power.

Power output can be extended beyond daylight hours by storing excess thermal energy during the day, and then utilising that energy after dark. The stored energy is used to drive a steam turbine in the SUNSPOT cycle. A rock bed is used for thermal energy storage, with air as the heat transfer fluid, as these are potentially more economical than other fluid and storage options (Kröger, 2012).

Combustion knowledge.   This project was intended to provide further insight and knowledge into gas turbine combustion, which will be necessary for the development of the SUNSPOT cycle.

Benefits of gaseous fuel.   The switch to a gaseous fuel was motivated by cleaner combustion (compared with liquid fuels), and the ease of combustion, as good atomisation of liquid fuels can be difficult to achieve. Given the benefits of switching to a gaseous fuel, the project presents a method that may be followed to convert other gas turbines.

Renewable fuel   The combustion of biogas will have zero nett carbon emissions (the process is carbon-neutral), because biogas is produced from renewable biomass.

Engine selection.   The Rover 1S/60 gas turbine has a simple external combustion can, which gives easy access for testing and modification. It was also the only engine available for the study.

1.5   Background

The Rover 1S/60 is an industrial gas turbine from the 1950's, with a single stage centrifugal compressor and a single stage turbine. Under no load the engine speed was governed at $47\,000 \pm 300$ RPM. The engine was rated for a continuous power output of 44.74 kW (60 bhp) at $46\,000$ RPM. More detailed engine specifications can be found in Appendix A.2.

Prinsloo (2008) was involved with the commissioning and instrumentation of a Rover 1S/60 engine at Pretoria University. He designed and tested an air intake, which was used to measure the mass flow-rate and filter the air. A bell mouth inlet was used to measure the flow-rate, and was designed according to the British Standard for performance testing using standardised airways (BS 848: Part 1: 1980).

Prinsloo tested the engine with a recuperator, but without applying load to the engine. He estimated a 10 and 12 % thermal efficiency, with and without the recuperator, respectively. The air intake built by Prinsloo was used in this study, and the intake pressure drop measured in this study was compared with the measurements taken by Prinsloo (see Appendix B.4).

Quarta (2012) used a one dimensional thermal-fluid network model to simulate the standard Rover engine, the engine with a recuperator, and the engine with a solar receiver and thermal storage. The model was developed in Flownex software. Quarta verified his standard model with data from Prinsloo (2008).

Homann (2015) also used Flownex to investigate the effects of solarising the Rover engine. The concept was to divert the compressed air through a solar receiver, and then return the air into the combustor. The heat of combustion was adjusted to maintain the standard turbine inlet temperature (TIT), with different levels of solar heating.

Homann found that increasing the solar heating reduced the fuel consumption, but increased the pressure loss through the solar receiver, and hence reduced the power output. He found that a compressor with a higher pres-

sure ratio could compensate for the pressure loss, and the rated engine power could be maintained.

Zhang (2016) and Luiten (2015) were involved with the set up and instrumentation of the Rover engine on a dynamometer. Initial engine tests were run on jet fuel (Jet A-1) with the *original fuel system* that was supplied by the manufacturer. Thereafter, Zhang replaced the fuel system and successfully ran the engine on LPG at low speed. This is referred to as the *initial fuel system* as it was the first configuration tested as part of this research. Refer to Appendix A.4 for details.

Zhang's jet fuel test data had a no-load speed of $46\,240 \pm 75$ RPM, and a peak power of 39 kW at $39\,300$ RPM. The top speed with LPG was $22\,519$ RPM, and no load was applied to the engine when supplied with LPG. Zhang occasionally observed flames exiting the turbine on start up while running on jet fuel, indicating that the combustion was incomplete before the turbine. This observation was not noted for the LPG tests.

The initial LPG injector design did not work as the fuel failed to ignite. The design was changed to direct the fuel towards the igniter, which resulted in the successful ignition and a stable flame.

Luiten (2015) experimentally and computationally (CFD) analysed the standard Rover compressor, and then designed a new compressor to compensate for the pressure loss through a solar receiver. The compressor efficiency, determined with CFD, was increased from 63.8 % to 85.6 %, and the total-to-static pressure ratio was increased from 2.5 to 3.3. Because of the increased efficiency, the power required by the two compressors differed by only 1.6 %.

1.6   Report overview

Chapter 2 is a literature review relevant to this study. A generalised fuel conversion method is presented in Chapter 3, followed by a description of the propane control system in Chapter 4. The control system was improved to allow a higher fuel flow-rate and better control.

Chapter 5 covers the analysis of the engine cycle, test data and fuel flow-rate prediction. This analysis was used to determine the requirements of the fuel control system, and to provide reference values for a CFD analysis, which is presented in Chapter 7.

The engine test facility, test procedures and results are described in Chapter 6. An overall project discussion and conclusion are presented in Chapter 8.

2. Literature Review

The Rover engine used in this study is a simple open-cycle gas turbine, without any heat recovery mechanism. The following literature review is limited to gas turbine combustion, fuels relevant to this research, and the thermodynamics used to analyse the engine and fuel flow.

2.1   Combustion

The information in this section was taken from Saravanamuttoo *et al.* (2009), unless stated otherwise.

The combustion of a liquid fuel requires the atomisation of the liquid into a fine spray of droplets, mixing the droplets with air, the evaporation of the droplets, the decomposition of heavy hydrocarbons into lighter fractions, the intermolecular mixing of hydrocarbons with oxygen, and finally the chemical reaction.

Enthalpy of reaction

The global reaction of a stoichiometric mixture of a hydrocarbon and oxygen can be expressed as

$$C_xH_y + (x + y/4)\,O_2 \longrightarrow x\,CO_2 + (y/2)\,H_2O \tag{2.1}$$
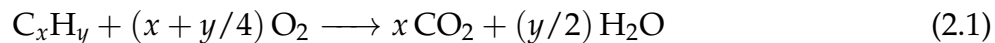
The enthalpy of reaction is the difference in enthalpy between the products and reactants. The *calorific value* of the fuel, or the heat released by combustion per unit mass, is equal to the decrease in specific enthalpy, typically at a reference temperature of 25 °C ($q_f = -\Delta h_{25}$).

The amount of energy released depends on the phase of the water. The *gross calorific value*, or *higher heating value*, represents the heat released when the water is a liquid; and the *nett calorific value*, or *lower heating value*, represents the heat released when the water is a vapour.

Combustion efficiency

The fundamental definition of *combustion efficiency* is the ratio of actual energy released to the theoretically available energy. The efficiency can be determined from a chemical analysis of the combustion products. This is done by comparing the air-fuel ratio to the proportion of incompletely burnt constituents.

Instead of using the fundamental definition, Saravanamuttoo *et al.* (2009) use the following definition,

$$\eta_b = \frac{\text{theoretical } f \text{ for given } \Delta T_0}{\text{actual } f \text{ for given } \Delta T_0} \tag{2.2}$$

where f is the fuel-air ratio, and ΔT_0 is the stagnation temperature rise. They state that the difference between their definition and the fundamental definition is negligible, because most combustion is 98-99 % complete. The mostly complete combustion also makes it difficult to accurately measure the combustion efficiency, and this is discussed further in Section 2.3.

Equivalence ratio

The equivalence ratio is the ratio of oxygen for a stoichiometric mixture to the actual amount of oxygen,

$$\phi = \frac{\text{stoichiometic oxygen/fuel}}{\text{actual oxygen/fuel}} \tag{2.3}$$

Reaction rate

Over most gas turbine operating ranges, the rate of chemical reactions are high. Complete combustion is limited by fuel evaporation and mixing (Lefebvre, 1983). Chemical kinetics (kinetic theory applied to reacting gases) predict that the rate of a simple bimolecular gas reaction will be proportional to square of pressure and some function of temperature,

$$r \propto p^2 f(T) \tag{2.4}$$

Stoichiometric homogeneous mixture tests suggest that the pressure exponent should be 1.8 (not 2). However, the chemical reaction is not the limiting factor for design operating conditions, and mixing plays an important role. For normal operation, an exponent of 1 is more appropriate. Under extreme condition (e.g. high altitude), performance may depend on $p^{1.8}$.

Dissociation

At low temperature, and stoichiometric or lean combustion, only CO_2 and H_2O are produced. However, at high temperatures (above 1800 K), the products can dissociate to form CO, H_2, O, H and OH (Lefebvre, 1983).

The *adiabatic flame temperature* is the temperature that the products of combustion would reach if all the heat of combustion was used to heat them. The adiabatic temperature is reduced by dissociation, and thus the peak temperature is found for a slightly rich mixture ($\phi = 1.1$).

Dissociation is an endothermic and reversible reaction that increases the number of gas molecules (and hence pressure). According to the Le Chatelier's principle, equilibrium will shift so as to counteract a change applied to a system (Brown *et al.*, 2003). Thus dissociation can be increased with temperature, or reduced with pressure (Lefebvre, 1983).

The stoichiometric flame temperature will only increase by about half the increase in inlet (reactant) temperature, because the amount of dissociation increases with temperature. A finite increase in flame temperature will result from a pressure increase, as this drives the reverse reaction of dissociation (Lefebvre, 1983).

2.2   Gas turbine combustors

The information in this section was taken from Saravanamuttoo *et al.* (2009), unless stated otherwise.

Combustors require an upstream diffuser, to slow down flow from the compressor; a recirculation zone, where velocities are low enough for sustained combustion; a dilution zone, to reduce the temperature to suit the turbine; and possibly an intermediate zone, to recover chemical dissociation losses (Lefebvre, 1983). Hot combustion products are mixed with the cold reactants in the recirculation zone to provide the activation energy necessary to ignite the reactants (Boyce, 2006).

The reactant mixture, which is approximately stoichiometric, burns rapidly within the burning zone. In the dilution zone an excess of air is added to cool the mixture to a temperature suitable for the turbine. Typically incomplete combustion is frozen once it reaches the dilution zone (Boyce, 2006).

Combustor criteria

Combustors are required to operate reliably at extreme temperatures, create a temperature distribution suitable for the turbine, and keep pollutants to a minimum over a long life. Flame stability and the ability to relight the combustor at altitude are critical for aircraft.

Improved materials and blade cooling have allowed turbine inlet temperatures (TIT) to increase from 1100 K to 1850 K. The Rover TIT was estimated as 1040 K (766 °C) in Section 5.3. The temperature distribution leaving the combustor also needs to suit the turbine. Local hot spots lead to higher stresses, and ultimately reduce the average TIT limit. The temperature can be higher towards the turbine blade tips, as the centrifugal stress decreases from the root to tip.

Carbon deposits (coking), which form from unburnt hydrocarbons (UHC), must be avoided since the turbine blades can be eroded by small particles, or damaged by larger particles that build up on combustor surfaces, and then break free due to vibration. It is also important to minimise exhaust smoke and emissions.

Combustion must remain stable, despite a high velocity stream (typically between 30 & 60 m/s), and overall lean mixture. The overall air-fuel ratio for a simple gas turbine is between 60 and 120:1, or between 100 and 200:1 if a recuperator is used. Whereas the stoichiometric ratio is about 15:1 for a typical hydrocarbon fuel.

The stability of a combustor can be evaluated by finding the rich and lean extinction limits for different air flow-rates; see Figure 2.1. Most control systems limit the rate-of-change of fuel flow to avoid blow-out, as well as high transient temperatures. For aircraft, the stability needs to be checked for the compressor delivery pressure at the highest altitude. The stability is improved by higher pressure ratios, because of the increased reaction rate. The ignition performance can be expressed by an ignition loop, which is similar in shape, but smaller than the stability loop.
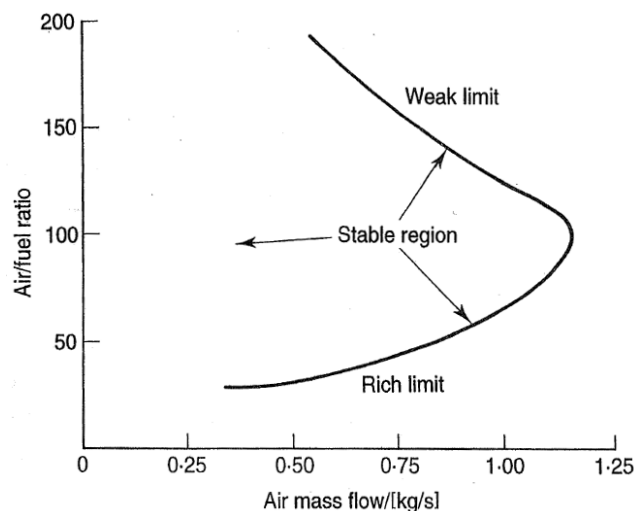
Figure 2.1: Combustor stability limits (Saravanamuttoo *et al.*, 2009)

Correct mixing and stable combustion is required across a range of flow-rates. The fuel flow-rate at idle might be as little as 1 % of the full load rate. Although the air-fuel ratio might only vary by a factor of three (Boyce, 2006).

Types of combustors

Can or *tubular* combustors are well suited to centrifugal compressors. Engines might have several cans, spaced radially about the engine axis (shaft), with a separate fuel supply for each can. Tubular combustors are cheap to design and test, because the cans can be tested separately. They are no longer used for aircraft because of their high weight, and large volume and frontal area. Small gas turbines, such as those used as auxiliary power units (APU) or for vehicles, often use a single combustion can. The Rover gas turbine is an example of such.

Cannular or *tubo-annular* combustors have individual flame tubes uniformly spaced in annular casing, and are widely used in industrial engines.

Annular combustors maximise the use of space within a specified diameter, and minimise the pressure loss. However, it is difficult to obtain even fuel-air distribution and outlet temperature, the structure is inherently weaker, and testing must be performed on the complete combustor (unlike tubular combustors). All modern aircraft use annular combustors, because of the size and weight advantage.

Combustion intensity

The combustion chamber size is largely determined by the rate of heat released. A larger chamber will make it easier to minimise the pressure loss, maximise efficiency, and produce uniform temperature distribution, and achieve stable operation.

The reaction rate will increase with both pressure and temperature, and the rate of fuel evaporation will increase with temperature. An engine with a higher pressure ratio, will also have a higher compressor outlet temperature, and hence a higher reaction rate.

The combustion intensity is defined as the heat release rate, divided by the combustor volume and pressure ($CI = \dot{Q}/Vp^a$). The units of CI depend on whether $a = 1$ or 1.8 in the definition (refer to the reaction rate dependence on pressure in Section 2.1). Aircraft have combustion intensities between 20 and $50\,\mathrm{MW/m^3}$ atm. Industrial combustion intensities can be much lower, especially if a recuperator is used.

Flame tube

The flame tube contains the combustion, distributes the air supplied by the compressor into the different zones, and is a radiation shield for the surrounding hardware. Air is introduced in stages due to the high air-fuel

ratio. Between 15 and 20 % of the air enters the primary zone, about 30 % enters the secondary zone, and the remaining air enters the tertiary (dilution) zone. The different zones in the Rover flame tube are illustrated in Figure 2.2.

The primary zone anchors the flame, and provides sufficient time, temperature and turbulence to essentially achieve complete combustion. At low altitudes, dissociation losses are recovered in the secondary (intermediate) zone, which also allows imperfectly mixed pockets of fuel and air to combust completely. At high altitudes, the reaction rate is slower, and the secondary zone serves to extend the primary zone (Lefebvre, 1983). The dilution zone achieves the correct temperature distribution.
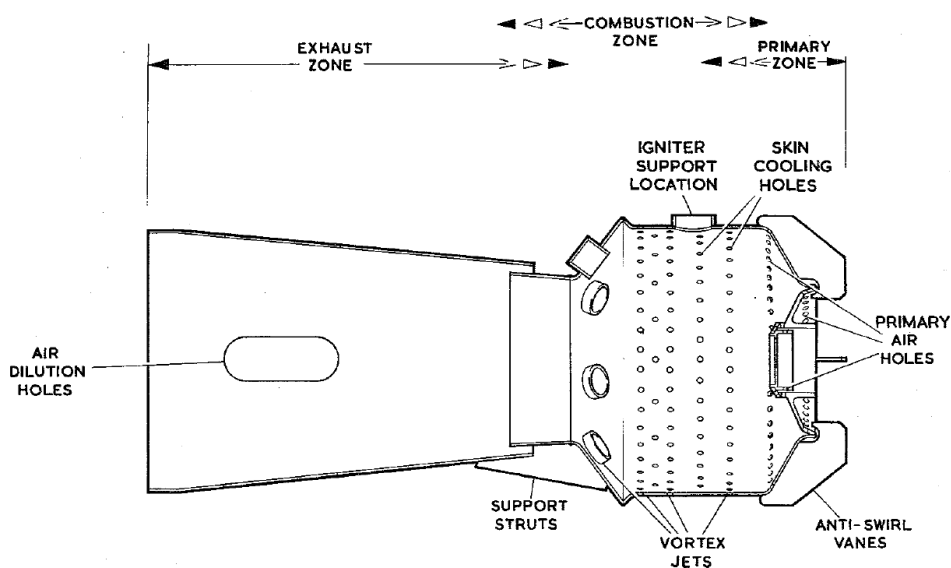
Figure 2.2: Typical Rover flame tube (Overhaul Manual, 1972)

A recirculation zone is required near the combustion zone to maintain a stable flame, because the air speed is about an order of magnitude greater than the flame speed. The recirculation also provides the heat necessary to ignite the fresh mixture. Vortex jets on the Rover flame tube create a toroidal vortex within the combustion zone (refer to Figure 7.2).

Under normal operation the reaction rate is limited by the mixing rate, and will be increased by turbulence. A trade off is required between high turbulence, which improves combustion; and pressure loss, which reduces the engine efficiency.

The pressure loss can be attributed to hot and cold losses. The pressure loss for cold flow (no combustion) results from skin friction and turbulence, and

is about twenty times the inlet dynamic pressure. The fundamental (hot) pressure loss is from the heat of combustion that causes the gases to expand and accelerate. The hot loss is only about one or two times the inlet dynamic pressure.

Flame tube cooling

The air entering the combustor is used to cool the flame tube, which is irradiated by the hot combustion gases. A narrow gap (annulus) between overlapping sections will create a film of cooling air along the inner surface. Wiggle strips may be used to join successive tube lengths (spot welded to tube sections).

Alternatively, a similar result can be achieved with a circumferential row of holes that impinge air onto an internal splash ring. An annular gap is shown above the support strut on the typical Rover flame tube (Figure 2.2). However, the flame tube used in this study only had skin cooling holes.

A more recent development uses transpiration cooling, where air flows through a network of passages within the flame-tube wall before exiting, to form an insulating film of air. The cooling air flow can be reduced by up to 50 % with this technique.

As the TIT limits increase with improved turbine materials and cooling, pressure ratios may also be increased, which leads to higher engine cycle efficiencies. A pressure increase results in hotter compressed air, and reduced cooling. New industrial turbines have pressure ratios between 17:1 and 35:1, with combustor inlet temperatures between 454 and 649 °C (Boyce, 2006). Transpiration cooling will probably become essential as TIT reach 1850 K (Saravanamuttoo *et al.*, 2009).

Flame tube temperature prediction

Convective heat transfer and flame tube temperatures have been correlated empirically. However, the flame and flame tube can vary so widely that it is not possible to accurately predict the flame tube temperature from an energy balance. Final development is still a matter of trial and error.

The flame emissivity varies with fuel type, and tends to increase with specific gravity. Carbon dioxide and water vapour are the principle emitters for non-luminous flames, while soot particles are the principle emitters in luminous flames. Flame luminosity for pre-mixed fuel vapour and air is lower than that for droplet-air mixtures.

Emissions

By the early 1970s gas turbine design had achieved high combustion efficiency, flame stability and the elimination of visible smoke. At this stage emissions had received little attention, because the large air-fuel ratios led to the assumption that gas turbine combustion was relatively clean. However, with increased pressures and temperatures, which were required to achieve high cycle efficiencies, NO_x production rapidly increased. Emission control is probably the most important factor for modern industrial gas turbines.

Emissions include carbon monoxide (CO), nitrogen oxides (NO_x), unburnt hydrocarbons (UHC), and sulphur oxides (SO_x). NO_x is responsible for smog; acid rain; and, at high altitude, ozone depletion. CO is toxic at sufficiently high concentration levels, and UHC may contain carcinogens.

NO_x formation increases with residence time in the combustion zone, while CO & UHC are reduced. NO_x reaches a maximum close to the stoichiometric mixture, while CO & UHC are close to a minimum. NO_x production increases exponentially with flame temperature, where NO_x can be halved by reducing the flame temperature from 1900 K to 1800 K. After the combustion process, nitric oxide (NO) can oxidise further to produce nitrogen dioxide (NO_2), which might react with water to form nitric acid (HNO_3).

Similarly, if sulphur is present in the fuel, then sulphuric acid (H_2SO_4) may be produced from sulphuric oxide (SO_3) and water. This will only occur once the temperature is low enough for condensation to occur, for example in heat recovery components or once exhausted into the atmosphere. However, if alkali metals are present in the fuel, then sulphur can lead to corrosion in the hot section of an engine (Boyce, 2006).

Carbon emissions refer to the release of carbon dioxide into the atmosphere. As a greenhouse gas, it is beneficial to reduce carbon dioxide emitted in power generation. The consumption of bio-fuels is carbon neutral (nett carbon emission is zero), because the amount of carbon dioxide released by burning the fuel is equal to that consumed in the production of the fuel. Carbon emissions per unit of energy produced depends on the ratio of hydrogen to carbon of the fuels.

Emissions control

Smoke is mostly formed in local fuel-rich regions, and is eliminated with leaner primary zones ($\phi = 0.9...1.5$). Carbon monoxide will only form in rich mixtures, and is generally not a problem with gas turbines, which have an overall lean mixture. Unburnt hydrocarbons are only produced if combustion is incomplete, which is typical of idle conditions (Boyce, 2006).

Improved atomisation and higher local temperatures can improve the combustion efficiency, and hence reduce UHC & CO. It is not economical to prevent the formation of sulphuric acid during the combustion process. Instead sulphur is removed from the fuel (Boyce, 2006).

NO_x formation can be reduced by reducing the flame temperature, and this can be achieved by injecting water into the combustion zone, selective catalytic reduction (SCR), or with rich or lean combustion (dry low NO_x). Injection of water, with a water-fuel ratio of 1:2 (by mass), can reduce NO_x by about 40 %, resulting in NO_x levels of about 77 ppmvd (parts per million volume dry). Water-fuel ratios can even exceed 1:1. The reduced thermal efficiency is offset by the increased power due to increased mass flow-rate across the turbine. Unfortunately CO & UHC increase with reduced NO_x levels.

SCR uses a catalyst and a controlled amount of ammonia (NH_3) to reduce NO_x into nitrogen (N_2) and water. The reaction only takes place between 285 and 400 °C, and as a result SCR can only be used with a waste heat recovery application. The SCR is installed midway through the heat recovery steam generator.

Dry low NO_x is the current focus of all gas turbine designers, which reduces emissions without water. The rich-burn/quick-quench option uses a rich primary zone, followed by rapid dilution to avoid smoking. The more popular method is lean premixed combustion.

Dry low emission systems can have combustion instability with pressure pulsations. Pre-mixed combustion can lead to more abrupt combustion than diffusion, which can cause resonance and mechanical failure.

2.3   Combustor experimentation

The information in this section was taken from Saravanamuttoo *et al.* (2009), unless stated otherwise.

Combustion efficiency

It is very difficult to accurately determine the combustion efficiency from a chemical analysis, because of the high combustion efficiency and air-fuel ratio, and the potentially high velocity stream. Saravanamuttoo *et al.* (2009) recommend using the fuel-air ratio and mass-weighted average temperature rise to calculate the efficiency (Equation 2.2).

The average temperature is determined by dividing the boundary into sev-

eral small areas, and taking measurements at the centre of each area.

$$\overline{T}_0 = \frac{\sum \dot{m}_i T_{0i}}{\dot{m}} \qquad \text{where } \dot{m}_i = \rho_i A_i \sqrt{2 p_{di}/\rho_i} \, , \quad p_{di} = \tfrac{1}{2}\rho_i v_i^2 \, , \qquad (2.5)$$

and p_{di} is the dynamic pressure. By dividing the boundaries into equal areas, and assuming simple axial flow with no swirl, the equation can be reduced to an expression with just the dynamic pressure and stagnation temperature,

$$\overline{T}_0 = \frac{\sum \sqrt{p_{di} T_{0i}}}{\sum \sqrt{p_{di}/T_{0i}}} \qquad\qquad\qquad (2.6)$$

The dynamic pressure can be measured with a pitot tube. The combustor outlet temperature is not often measured on an engine, because failure of the thermocouple support could lead to turbine damage. Instead the exhaust gas temperature is measured.

High temperature measurements

High temperature measurement accuracy will be affected by:

- conduction along wires vs. convection onto wires
- radiation from flame, and radiation onto walls (error can be up to 60 K for 1300 K)
- friction heating from airflow
- the fraction of the dynamic temperature that is measured, $T_d \approx 40\ K$ for 300 m/s

To account for these possible measurement errors, thermocouples are placed in tubes to allow adiabatic deceleration of gas flow (same principle as pitot tube). Radiation shields are required for high temperature. Wires run parallel with flow stream (isothermal stream) for about 2-3 cm to reduce the conduction error. Chromel-alumel thermocouples can maintain accuracy up to 1300 K. With all of these features, 1300 K can be measured within 5 K of the true value.

Isolated combustor testing

The combustor can be tested in isolation to avoid the risk of engine damage, and to make it easier to instrument the combustor. For example, combustion induced vibration or pressure pulsation, flashback, and excessive temperatures could damage the turbine.

Isolated testing simplifies independent air and fuel regulation. Whereas with engine testing, if the fuel rate is reduced, then the engine speed and air flow

will drop (for no load conditions). Thus an isolated combustor will simplify stability testing; where the flammability limits of the combustor can be tested for different air flow speeds, as shown in Figure 2.1.

Jayasuriya and Manrique (2005) describe the test procedure of an isolated Rover 1S/60 flame tube with variable air and fuel (propane) flow; refer to Figure 2.3. The flow-rates, pressure drop, gas species (O_2, CO & CO_2), and average outlet gas temperature were measured. Ambient air was drawn through the flame tube under the action of a downstream fan, and the flow-rate was regulated with a valve.
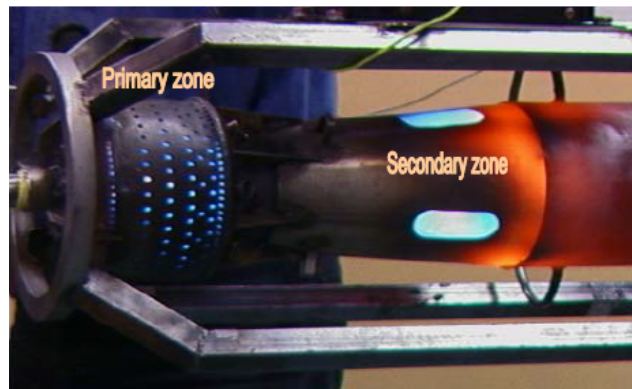
Figure 2.3: Rover 1S/60 flame tube testing (Jayasuriya and Manrique, 2005)

Similarly, Meyers (2009) tested an isolated flame tube. The outlet temperature profile was determined with a rake of thermocouples, and the outlet velocity was measured at different locations with a pitot tube. The pressure drop, and images of the flame and carbon deposits were also captured.

Cold flow testing

An isolated combustor can also be tested without combustion (cold/non-reacting flow). High combustion temperatures will make some measurements more difficult, and testing combustion will be more hazardous than doing cold flow tests.

Meyers (2009) used stereoscopic particle image velocimetry (PIV) to obtain three-dimensional velocity vectors on a plane in the flow-field of a perspex combustor. An oil mist was injected into the air flow, and a laser sheet illuminated a plane in the flow-field. The reflected light was captured by two cameras, and the velocities were determined from the displacement of the oil droplets.

The study was performed to provide data that could be used to validate a CFD model of the combustor. The outlet velocities were also measured with a pitot tube, and correlated with the measurements taken for reacting flow.

This technique could be used to aid the design of the flame tube jets and the recirculation zone. It could also be used to determine the effect of changing a fuel on the flow pattern.

2.4 Fuel injection

The information in this section has been taken from Lefebvre (1983), unless stated otherwise.

Early combustors injected fuel directly into the combustion zone (i.e. non-premixed/diffusion flames). Combustion was stable, but emissions were high. Modern combustors use lean pre-mix systems, which greatly reduce emissions, but lead to instability, flame out, aerodynamic or acoustic vibration, and mechanical durability issues.

Atomisers

Liquid fuel must be atomised before it enters the combustion zone. *Atomisation* is the process of breaking liquid fuel into tiny droplets, resulting in a higher surface area to volume ratio, and hence more rapid evaporation of the fuel. Liquid fuel does not combust, and thus inadequate atomisation can lead to poor or incomplete combustion. Gaseous fuel does not require atomisation, and generally will result in clean complete combustion.

Liquid fuel injectors that atomise the fuel are also referred to as *atomisers*. Several atomiser designs have arisen from the difficulty of producing a fine spray of fuel for a wide range of fuel and air flow-rates. The majority of designs either inject a high velocity liquid into slow moving air (e.g. simplex atomiser), or apply high velocity air to a slow moving liquid (e.g. air-assist or airblast atomiser).

In a *simplex*, or *swirl*, atomiser, pressurised fuel enters a swirl chamber through tangential ports. Then the fuel is sprayed through an orifice into the primary/combustion zone of the combustion. The fuel is swirled so that it forms a conical spray.

Simplex atomisers have a narrow fuel flow range, low combustion efficiency and inadequate relight capabilities at altitude. The fuel flow-rate is proportional to the square root of the supply pressure. The minimum supply

pressure of kerosene is 100 kPa. To increase the flow-rate twenty times, the supply pressure would need to be raised to 40 MPa.

A *shroud cap* can aid cooling of the atomiser face, and keep it free of deposits. It can also aid the atomisation quality at low fuel flows, improve light up, and reduce the weak extinction limit. *Wide range* atomisers try to achieve good atomisation and cone angles across a wide range of flow-rates. For example the duplex, dual orifice, or spill atomiser.

Air-assist atomisers use high velocity, but a low flow-rate of, air from a compressor or cylinder to aid atomisation. Fuel and air either mix internally (within the atomiser), or externally (air and fuel are injected separately). Internal mixing results in good atomisation down to zero flow, which is good for viscous fuel. For external mixing, the spray angle remains constant, and there is no risk of fuel in air line, but the use of air is less efficient. External air supply at high pressure is generally required at start-up, which is not ideal for an aviation application.

Airblast atomisers use a lower air velocity (<120 m/s), but a higher flow-rate than an air-assist atomiser. As a result, the required pressure is also lower. The airblast atomiser is ideal for high pressure gas turbines. It requires a lower fuel pressure, and produces a finer spray. Thorough mixing is achieved, with low soot formation, and a blue flame with low luminosity. This results in a cooler flame tube and less smoke. Fuel and flame distribution remain fairly constant across the flow range.

Uniform mixing leads to a narrow stability/combustion range compared with poor mixing, due to rich pockets that are still flammable. An air-fuel ratio of 1000 is a typical weak-extinction limit of a pressure system, versus a ratio of only 100 for a well mixed system.

Hybrid or piloted systems employ both systems for easy light up, satisfactory combustion efficiency, and high weak extinction limits at low fuel flow; and avoid a highly luminous flame, copious smoke, and pattern sensitivity to fuel flow at high air pressure. An example of such a system would use a simplex atomiser as a pilot, and an airblast atomiser for higher fuel rates.

Gas injection

Gaseous fuel combustion tends to be clean, with little soot and NO_x formation, provided the energy density is high. The main challenge is to achieve the correct level of mixing. Narrow stability limits will result from excessive mixing, and combustion-induced pressure oscillations may result from inadequate mixing. Typical injectors include simple slots or orifices, swirlers, or venturi nozzles.

Industrial gas turbines might be equipped with a dual fuel system that enables the engine to be run on either liquid or gaseous fuel. During the changeover from one fuel to the other, careful control of both fuels, and matching of fuel flow patterns, is required to avoid blow-out, over-temperature, and variation in the outlet temperature distribution.

Flashback

Flashback is an intrinsic tendency of all pre-mixed combustion systems. Lefebvre (1983) defines flashback in practical combustors as fast chemical reaction in the premixing section of the combustor, owing to upstream propagation of a flame from the main combustion zone. The fast chemical reaction is accompanied by significant heat release.

Flashback may either occur in the free stream, or in low velocity regions, such as the boundary layer along the flame holder. Flashback can occur in the free stream if the combustor bulk flow reverses due to compressor surge, a blockage, or combustion instability. Flashback can occur in the premixed section if the turbulent flame speed is greater than the bulk flow. The flame speed can be increased by high temperatures, pressures, and turbulence; and by pre-ignition due to extended residence times at high temperatures.

2.5   Fuel selection

There are several factors that need to be considered when selecting fuel for a gas turbine. Some of these factors are briefly discussed, followed by a description of the fuels relevant to this project.

2.5.1   Fuel criteria

Gas turbines are versatile with regards to the type of fuel. To achieve the same power output, the rate of chemical energy released during combustion must remain the same. The calorific value is a measure of energy density. Typically it is listed as the amount of chemical energy per unit mass for liquid fuel, or per unit volume for gaseous fuel. The calorific value will influence the fuel storage size and the consumption rate required by the engine/process.

The Wobbe index is the ratio of the lower heating value (on a volumetric basis) to the square root of specific gravity (air is typically used as the reference). It is used to determine whether gaseous fuels are interchangeable in the same fuel system. Essentially if fuels have similar indices, then the energy supplied at the same pressure drop will be similar and a direct substitution can be made. Gases with indices within $\pm 10\,\%$ can be substituted without

changes to the fuel system (Kurz and Mokhatab, 2012).

$$WI = LHV / \sqrt{SG} \tag{2.7}$$

The critical temperature and vapour pressure of a fuel will affect how it is stored and injected in the combustion chamber. A fluid cannot be liquefied above its critical temperature, and cannot be injected as a gas if the injector pressure is higher than the vapour pressure. Sufficient injector pressure is required to overcome the combustor pressure, and to achieve adequate mixing. Fuel impurities can affect the calorific value, emissions, and can lead to corrosion of the fuel supply system and engine components.

2.5.2 Suitable fuels

The fuels properties have been summarised in Table A.1, which is in Appendix A. The fuels discussed below have similar calorific values ($46 \pm 4\,\text{MJ/kg}$).

Methane, ethane, propane, and butane are saturated hydrocarbons that are commonly referred to as alkanes (Brown *et al.*, 2003). They have been listed in increasing molecular size, and hence also in increasing density. The smaller molecules have lower carbon to hydrogen ratios, and hence produce less carbon dioxide per unit energy (ESCAP, 1993; Ariztegui *et al.*, 2015).

Jet fuel is a high grade kerosene (paraffin oil) and gets its name from common use in jet engines. It is liquid at standard conditions, and has a relatively high calorific value making it a good choice for aviation (Shell, 2003). Most aeronautical gas turbines use liquid petroleum distillates, such as jet fuel (Saravanamuttoo *et al.*, 2009). The Rover engine used in this study was previously run on jet fuel, specifically Jet A-1, before the fuel conversion (Zhang, 2016).

Natural gas is rich in methane, 85-96 % by volume (Perry and Green, 2008), but also contains impurities such as hydrogen sulphide, water and carbon dioxide. Gas extracted from oil and gas wells is refined to remove impurities (Brown *et al.*, 2003). The terms *sour* and *sweet* refer to the absence or presence of hydrogen sulphide (Perry and Green, 2008).

Natural gas has a low density and can only be liquefied at very low temperatures. It is piped at 3.5 to 5 MPa (Brown *et al.*, 2003); transported as Compressed Natural Gas (CNG) at 20 MPa at ambient temperatures; or as Liquefied Natural Gas (LNG), which is kept at -161 °C and ambient pressures (ESCAP, 1993).

Natural gas is the preferred fuel for industrial applications, because it has few impurities, and does not require atomisation or vaporisation. However,

it is expensive relative to residual oil and coal. Residual oil is the leftover residue from the distillation of profitable light fractions from crude oil (Saravanamuttoo *et al.*, 2009). Coal cannot be used directly in a gas turbine, but it can be gasified (processed) to produce syngas, which contains methane, carbon monoxide and hydrogen (Brown *et al.*, 2003).

Some industrial gas turbines are fitted with a dual fuel system, where natural gas is used for normal operation, and liquid fuel for short periods (when natural gas is unavailable). The injectors may also accommodate steam or water injection for NO_x control.

Liquid petroleum gas (LPG) is primarily a mixture of propane & butane, which can be stored as a liquid if kept under moderate pressures at standard temperature; 850 kPa & 220 kPa for propane and butane respectively (Afrox, 2016). LPG is a relatively clean fuel as it has low impurities, short molecular chains and is typically supplied to a combustor in a gas state (Ariztegui *et al.*, 2015).

LPG is extracted together with crude oil and natural gas. It is also produced by refining petroleum (Ariztegui *et al.*, 2015). It is readily available in South Africa, however on an energy basis it is more expensive than common fuels (Department of Energy, 2017, 2018).

LPG has similar properties to natural gas, except for a higher volumetric energy density. LPG can be used as a natural gas substitute by diluting it with air, which is referred to as SNG (synthetic natural gas). The required mixture is too rich be flammable, but obviously there is a risk of creating a flammable mixture, which makes SNG more hazardous than natural gas. This presents a possible option to mimic natural gas combustion, without having to source it.

Biogas is a renewable fuel that is produced by anaerobic digestion of organic waste. It typically contains 50-75 % methane, 25-45 % carbon dioxide, and 2-7 % water. It also contains small fractions of oxygen, nitrogen, hydrogen sulphide and ammonia. Biogas can be used as a substitute for natural gas, but the impurities must be removed. The methane concentration must be increased to 98 % before feeding biogas into a natural gas pipeline (Biogas, 2013).

The presence of hydrogen sulphide in both biogas and natural gas can present a problem for both storage and combustion of the fuels, given its corrosive nature. Natural gas consumers specify limits to the gas composition and energy content. Impurities must be removed from natural or biogas to meet these requirements (Biogas, 2013; Cho *et al.*, 2009).

2.6 Gas dynamics

The information in this section has been taken from Moran and Shapiro (1998), unless stated otherwise.

Specific heats

The specific heats c_v and c_p are respectively defined as the partial derivatives, with respect to temperature, of internal energy with constant volume and enthalpy with constant pressure,

$$c_v = \left.\frac{\partial u}{\partial T}\right)_v \qquad c_p = \left.\frac{\partial h}{\partial T}\right)_p \tag{2.8}$$

They are related by the gas constant $c_p = c_v + R$, and the specific heat ratio $\gamma = c_p/c_v$.

The specific heats of *real gases* over normal pressure and temperature ranges are approximately dependent on temperature only. If the relation between specific heat and temperature is known or approximated, then the change in enthalpy (or internal energy) can be found by integration with respect to temperature (Saravanamuttoo *et al.*, 2009).

The equation of state of an *ideal gas* is given by $pV = mRT$, where p, V, m, R, T are the pressure, volume, mass, gas constant and temperature of the gas. The specific heats of an ideal gas are only dependent on temperature. A *perfect gas* is an ideal gas with constant specific heats.

Constant specific heat

A common approximation is to treat the specific heat as constant. The accuracy of this will depend upon the temperature range and fluid involved.

$$h(T_2) - h(T_1) = c_p(T_2 - T_1) \tag{2.9}$$

Ideally the mean specific heat $\bar{c}$ for the temperature range will be used, where the mean value is calculated as (Saravanamuttoo *et al.*, 2009)

$$\bar{c} = \frac{\int_{T_1}^{T_2} c(T)dT}{T_2 - T_1} \tag{2.10}$$

Saravanamuttoo *et al.* (2009) state that normally it is sufficiently accurate to use the following values for a gas turbine analysis.

- compression of air: $c_{pa} = 1.005\,\text{kJ/kg K}$, $\gamma_a = 1.40$

- expansion of combustion gases: $c_{pg} = 1.148\,\text{kJ/kg\,K}$, $\gamma_g = 1.333$
- liquid hydrocarbon fuels $c_{pf} \approx 2\,\text{kJ/kg\,K}$

For exhaust gases from typical hydrocarbon fuels, the mean molecular mass M_g is similar to that of air M_a. And thus the gas constant for air R_a can be used for the exhaust gases.

$$M_g \approx M_a \rightarrow R_g \approx R_a = 0.287\,\text{kJ/kg\,K} \tag{2.11}$$

Dissociation has a significant effect on the specific heat values, and is very dependent on pressure above about 1500 K (Saravanamuttoo *et al.*, 2009). The Rover turbine inlet temperature is closer to 1000 K, as will be shown in Section 5.3. So this effect has little significance for the Rover engine.

The error in calculating Δh due to the approximate c_p value, is typically reduced by the error in calculating ΔT due to the approximate γ value. This is because c_p increases, while γ decreases, for a given change in temperature. The temperature values are thus less accurate than the change in enthalpy (Saravanamuttoo *et al.*, 2009).

Isentropic process

The change in entropy of an ideal gas is given by the following equation.

$$s(T_2, p_2) - s(T_1, p_1) = \int_{T_1}^{T_2} c_p(T)\frac{dT}{T} - R\ln(p_2/p_1) \tag{2.12}$$

For an isentropic process, where the specific heats are assumed constant, the equation is reduced to

$$p_2/p_1 = (T_2/T_1)^{\frac{\gamma}{\gamma-1}} \tag{2.13}$$

Stagnation properties

Stagnation properties represent the state a fluid would reach if brought to rest adiabatically. A subscript zero will be used to indicate stagnation properties. For example specific stagnation enthalpy, which is the sum of static enthalpy and kinetic energy; $h_0 = h + \frac{1}{2}v^2$.

For a perfect gas, where $h = c_p T$, the stagnation temperature is,

$$T_0 = \overbrace{\underbrace{T}_{\text{static temp.}} + \underbrace{\tfrac{1}{2}v^2/c_p}_{\text{dynamic temp.}}}^{\text{stagnation temperature}} \tag{2.14}$$

Stagnation enthalpy is constant if no work is done nor heat transferred, and by extension so is stagnation temperature. However, for constant stagnation

pressure, the flow must also be frictionless. Thus a drop in stagnation pressure can be a measure of fluid friction (Saravanamuttoo *et al.*, 2009).

Stagnation temperature is easier to measure than static temperature in high speed flow (Saravanamuttoo *et al.*, 2009). Stagnation pressure is calculated for isentropically arresting the fluid, which accounts for compressibility.

$$p_0 = p(T_0/T)^{\frac{\gamma}{\gamma-1}} = p\left(1 + \tfrac{1}{2}\mathrm{v}^2\frac{\rho}{p}\left(\frac{\gamma-1}{\gamma}\right)\right)^{\frac{\gamma}{\gamma-1}} \tag{2.15}$$

Whereas, for incompressible flow, which is typically assumed for liquids and low speed gas flow, the stagnation pressure is

$$p_0^* = p + \tfrac{1}{2}\mathrm{v}^2\rho \tag{2.16}$$

Compressible flow

The speed of sound is the rate at which small pressure disturbances can propagate through a medium. The speed of sound for an ideal gas is $c = \sqrt{\gamma RT}$. The *Mach number* is the fraction of the velocity of a fluid to the speed of sound of that fluid, $Ma = \mathrm{v}/c$.

Flow with a Mach number below 0.3 can generally be assumed to be incompressible (Munson *et al.*, 2002). For higher speeds the density variations become significant. The conservation of mass and energy are often used to evaluate the change in state across a control volume. Where possible, idealisations, such as assuming an ideal gas or an isentropic process, can be used to provide the necessary information to determine the change in state. The relevant equations have been summarised below.

$$\begin{aligned}
\dot{m} &= \rho \mathrm{v} A && \textit{continuity} \\
\rho &= p/RT && \textit{ideal gas} \\
T_0 &= T + \tfrac{1}{2}\mathrm{v}^2/c_p \ \text{ or } \ T_0/T = 1 + \tfrac{\gamma-1}{2}Ma^2 && \textit{conservation of energy} \\
p_0/p &= (T_0/T)^{\frac{\gamma}{\gamma-1}} = \left(1 + \tfrac{\gamma-1}{2}Ma^2\right)^{\frac{\gamma}{\gamma-1}} && \textit{isentropic process}
\end{aligned} \tag{2.17}$$

Choked flow

Figure 2.4 shows a converging-diverging nozzle, where the back pressure is varied with a valve and the inlet pressure is fixed. Initially the valve is shut, hence there is no flow and uniform pressure across the nozzle (case a). For a small reduction in back pressure, gas will flow from the inlet to the exhaust, but will remain subsonic throughout the nozzle (case b). For subsonic flow the diverging section will act like a diffuser, and thus the highest velocity and lowest pressure will be at the throat.
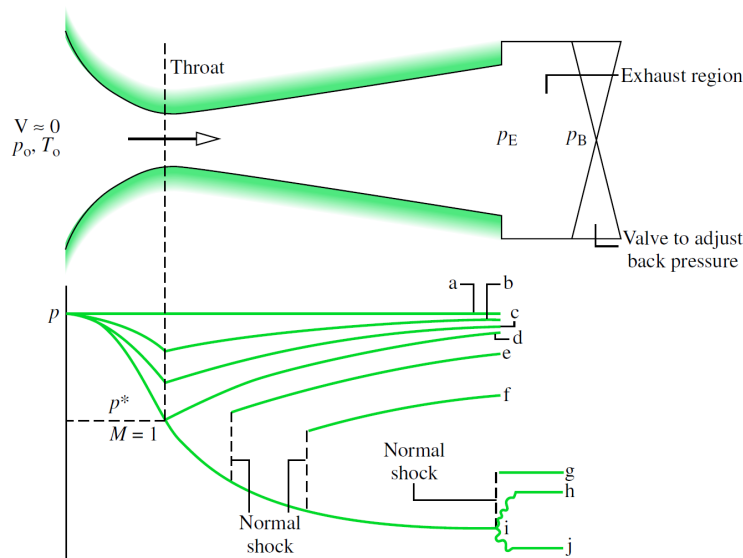
Figure 2.4: Effect of back pressure on a converging-diverging nozzle (Moran and Shapiro, 1998)

Case c represents a further reduction in back pressure that will result in an increased mass flow-rate, and the flow will be qualitatively similar to case b (i.e. subsonic). If the back pressure is sufficiently reduced, then the throat velocity will become sonic (case d). Pressure disturbances cannot propagate faster than the speed of sound, so the flow upstream of the throat will become independent of further reductions in pressure. This condition is referred to as *choked*, as the mass flow will remain constant with further reductions in the back pressure.

A further reduction in back pressure will cause the flow to become supersonic just after the throat. A normal shock wave will occur at some point along the divergent section. The region between the throat and shock wave is referred to as a diverging nozzle, as the flow is accelerated through this region of increasing area. The shock wave is a narrow region where the flow rapidly decelerates from supersonic to subsonic, resulting in a partial pressure recovery (case e). The shock wave will move down the nozzle as the back pressure is reduced (case f), until oblique shock waves occur outside of the nozzle.

2.7   The Brayton cycle

The information in this section has been taken from Moran and Shapiro (1998), unless stated otherwise.

Gas turbine thermodynamics can be idealised by the *Brayton cycle*, which

describes a constant pressure heat engine. The cycle consists of adiabatic compression, isobaric heat addition, adiabatic expansion, and then isobaric heat removal (see Figure 2.5). Constant volume combustion is theoretically more efficient than constant pressure, but it requires valves and intermittent flow. (Saravanamuttoo *et al.*, 2009, pp 3)

An *ideal Brayton cycle* is simplified further by assuming that there are no irreversibilities in the cycle. This implies that there is no pressure loss, and the compressor and turbine behave isentropically. The points 2′ and 4′ indicate the state after isentropic compression and expansion on the temperature-entropy diagram (Figure 2.5).
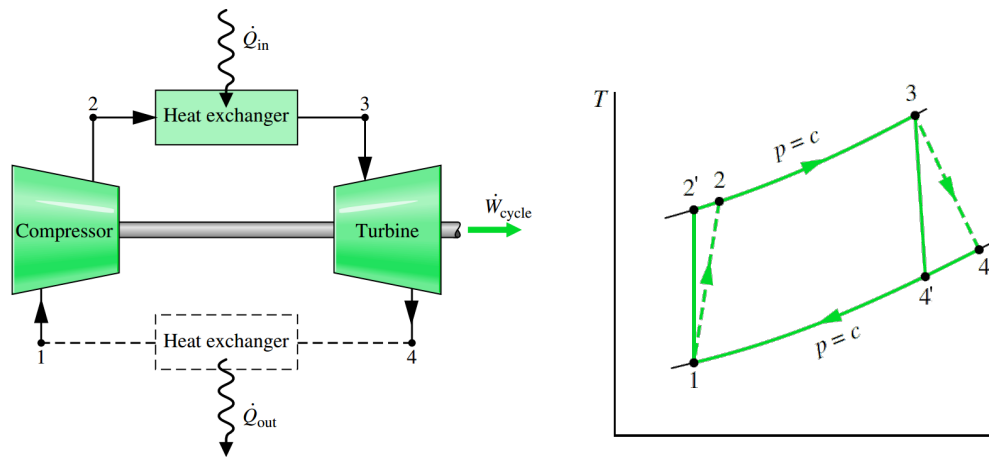
Figure 2.5: The Brayton cycle (adapted from Moran and Shapiro (1998))

An *air-standard analysis* is simplified by treating the working fluid as air and an ideal gas. Combustion is treated as a heat transfer process, where the mass flow-rate and gas composition remain unchanged. A *cold* air-standard analysis additionally assumes that the specific heats are constant, and properties of air at standard temperature and pressure are used.

Isentropic vs. polytropic efficiency

The *isentropic efficiency* of a compressor, η_c, is the ratio of ideal and actual compressor power, $\dot{W}_c'$ & $\dot{W}_c$, for the same pressure rise and mass flow-rate.

$$\eta_c = \frac{\dot{W}_c'}{\dot{W}_c} = \frac{\dot{m}c_p(T_{02}' - T_{01})}{\dot{m}c_p(T_{02} - T_{01})} = \frac{(T_{02}' - T_{01})}{(T_{02} - T_{01})} \tag{2.18}$$

Equation 2.13 is used to find the ideal (isentropic) compressor outlet temperature, T_{02}',

$$r_c = p_2/p_1 = (T_{02}'/T_{01})^{\frac{\gamma}{\gamma-1}} \tag{2.19}$$

Similarly the turbine isentropic efficiency, η_t, can be expressed as:

$$\eta_t = \frac{T_{03} - T_{04}}{T_{03} - T'_{04}} \qquad\qquad r_t = p_3/p_4 = (T_{03}/T'_{04})^{\frac{\gamma}{\gamma-1}} \qquad (2.20)$$

Polytropic efficiency, η_∞, is the isentropic efficiency for an elemental stage. It originates from assuming equal isentropic efficiencies for each stage of a multi-stage compressor or turbine, while the overall efficiency will vary with the number of stages. Polytropic efficiency tends to be used when predicting performance across a range of pressures, for which constant polytropic efficiency is assumed (Saravanamuttoo *et al.*, 2009). The actual temperatures and pressures are related by,

$$T_{02}/T_{01} = (p_2/p_1)^{\frac{n_c-1}{n_c}} \qquad \text{where} \qquad \frac{n_c - 1}{n_c} = \frac{\gamma - 1}{\gamma \cdot \eta_{\infty,\,c}} \qquad (2.21)$$

$$T_{04}/T_{03} = (p_4/p_3)^{\frac{n_t-1}{n_t}} \qquad \text{where} \qquad \frac{n_t - 1}{n_t} = \frac{\eta_{\infty,\,t}\,(\gamma - 1)}{\gamma} \qquad (2.22)$$

The resultant isentropic efficiencies will vary with the pressure ratio.

$$\eta_c = \frac{r_c^{(\gamma-1)/\gamma} - 1}{r_c^{(n_c-1)/n_c} - 1} \qquad\qquad \eta_t = \frac{1 - r_t^{(n_t-1)/n_t}}{1 - r_t^{(\gamma-1)/\gamma}} \qquad (2.23)$$

The rise in stagnation temperature across a centrifugal compressor can be approximated from the following equations,

$$T_{02} - T_{01} = \frac{\psi\sigma U^2}{c_{pa}} \qquad\qquad \sigma = 1 - 0.63\pi/n \qquad (2.24)$$

where ψ is the power input factor (typically between 1.035 and 1.04), σ is the Stanitz slip factor, and U is the impeller tip velocity. The slip factor is a ratio of the tangential speed of the air leaving the compressor to impeller tip velocity, and hence indicates how much the air slips relative to the impeller. It can be approximated by utilising the number of impeller vanes (n), as shown above (Saravanamuttoo *et al.*, 2009).

Combustion

The heat of combustion, which in the case of an air-standard analysis is conceptually transferred to the air with a heat exchanger, can be quantified as the product of fuel mass and enthalpy of reaction.

$$\dot{Q}_{in} = -\Delta h_{25} \cdot \dot{m}_f \qquad (2.25)$$

This assumes complete combustion and that the working fluid is heated by all of the available heat of combustion. For gas turbines, where the exhaust temperatures are high, the nett calorific value, or lower heating value (LHV), is applicable (Saravanamuttoo *et al.*, 2009).

Saravanamuttoo *et al.* (2009) use the following equation to relate combustor temperatures for complete combustion of a theoretical fuel fraction f_{th},

$$
\begin{aligned}
0 =& c_{pg} \left(1 + f_{th}\right) \left(T_{03} - 298\right) + f_{th}\Delta h_{25} + c_{pa} \left(298 - T_{02}\right) \\
& + f_{th} \cdot c_{pf} \left(298 - T_f\right)
\end{aligned}
\tag{2.26}
$$

where T_f and c_{pf} are the fuel temperature and specific heat, and Δh_{25} is the enthalpy of reaction at a reference temperature of 25 °C (298 K).

Thermal efficiency

The thermal efficiency and specific fuel consumption of a power cycle are respectively

$$
\eta = \dot{W}/\dot{Q}_{in} \qquad\qquad SFC = \dot{m}_f/\dot{W}
\tag{2.27}
$$

where $\dot{W}$ is the nett shaft power of the cycle (Moran and Shapiro, 1998). When an ideal Brayton cycle is analysed on a cold air-standard basis, the thermal efficiency can be expressed in terms of the pressure ratio and the specific heat ratio γ,

$$
\eta = 1 - T_1/T_2 = 1 - (p_1/p_2)^{(\gamma-1)/\gamma}
\tag{2.28}
$$

By comparison the Carnot cycle is the most efficient power cycle, and differs from the Brayton cycle in that the heat transfer is isothermal. Resulting in a rectangular temperature-entropy diagram. The Carnot efficiency is

$$
\eta = 1 - (T_C/T_H)
\tag{2.29}
$$

where the units of temperature are in Kelvin (K). The Carnot cycle assumes perfect heat exchangers and insulators, and the resultant efficiency is much higher than can be achieved practically. The Chambadal-Novikov-Curzon-Ahlborn cycle places a limit on the conductivity and time available for heat transfer, and the *maximum thermal efficiency* is much closer to the practical upper limit of a power cycle (Bejan, 1996),

$$
\eta = 1 - \sqrt{(T_C/T_H)}
\tag{2.30}
$$

Modern gas turbines have pressure ratios up to 45, and TIT exceeding 1800 K (Saravanamuttoo *et al.*, 2009). By comparison, the Rover engine has a pressure ratio of 2.8, and the TIT was estimated as 766.3 °C (1039.5 K) for standard operating conditions (see Section 5.3 & Appendix A.2). These values were used to compare the different efficiencies.

- 72.3 % Carnot efficiency; for $T_C = 15\,°C$ & $T_H = 766.3\,°C$
- 47.3 % maximum thermal efficiency; for $T_C = 15\,°C$ & $T_H = 766.3\,°C$
- 25.5 % Brayton efficiency; for $p_r = 2.8$ & $\gamma = 1.4$

An actual engine efficiency of 9.7 % was determined from the Rover specifications (Appendix A.2). The Carnot cycle efficiency is much higher than what a practical system could achieve. However, the maximum thermal efficiency is not too unrealistic, as efficiencies for a combined gas and stream cycle can be as high as 60% (Saravanamuttoo *et al.*, 2009). The Brayton efficiency seems fairly representative of the possible gas turbine efficiency, given the many idealisations upon which it is based.

Specific power

The *specific power* (nett work per unit mass flow) can be maximised for a turbine inlet temperature (TIT), which is limited by the turbine's material. There is a trade off between specific power, which improves the power-to-weight ratio of the engine; and thermal efficiency, which decreases with specific power. The specific power for an air-standard ideal Brayton cycle,

$$\frac{\dot{W}}{\dot{m}} = c_p T_1 \left[\frac{T_3}{T_1} - \frac{T_3}{T_1} \left(\frac{p_1}{p_2} \right)^{(\gamma-1)/\gamma} - \left(\frac{p_2}{p_1} \right)^{(\gamma-1)/\gamma} + 1 \right] \qquad (2.31)$$

If the specific power is maximised, then the pressure ratio becomes:

$$\frac{p_2}{p_1} = \left(\frac{T_3}{T_1} \right)^{\gamma/[2(\gamma-1)]} \qquad (2.32)$$

For a TIT of 766.3 °C, and ambient temperature of 15 °C, the specific power would be maximized with a pressure ratio of 9.44, resulting in a theoretical specific power of 234 kJ/kg. Whereas the Rover engine only has a specific power rating of 74.2 kJ/kg.

3. Conversion Methodology

A general method for the conversion of a gas turbine from a liquid to gaseous fuel is presented in this chapter.

3.1   Fuel characteristics

Consideration of the change in fuel properties is a key step in the conversion process. A major benefit of gaseous fuel is that it does not require atomisation, which simplifies the injection process. The calorific value, critical temperature, vapour pressure and density of the fuel are important when deciding on how to store, regulate and supply fuel to the engine.

The fuel density and calorific value will affect the required mass and volume of fuel to store. The (energy) density can be significantly increased by liquefying the fuel. To achieve this, the fuel must be stored above its vapour pressure, and below its critical temperature. For example, LNG is stored at $-161\,°C$ (ESCAP, 1993), given that methane has a critical temperature of $-82\,°C$ (Moran and Shapiro, 1998).

Gas injection is only possible if the supply pressure to the injector is below the vapour pressure. However, the injection pressure must be sufficiently greater than the combustor pressure to produce correct mixing. For example, at $20\,°C$ the vapour pressure of propane is 8.1 bar (Afrox, 2016)), which is below the operating pressures of modern gas turbines (17 to 35 bar, Boyce (2006)).

The use of low calorific gases can lead to a mismatch between the compressor and turbine, especially for multi-fuelled engines. They can have low reaction rates, requiring additional combustion zone volume. The fuel supply system needs to handle a higher volumetric flow-rate. It is also difficult to achieve ideal mixing rates; excessive mixing can lead to poor lean-blowout behaviour, while low mixing can lead to rough combustion (Lefebvre, 1983).

The presence of impurities may also present a problem. Both natural gas and residual oil contain impurities that need to be removed to avoid corrosion of the engine components. Magnesium compounds have also been used to neutralise vanadium that is present in residual oil (Saravanamuttoo *et al.*, 2009).

3.2 Fuel injection

It is important not to alter air and fuel flow patterns in the conversion, unless the change is intentional for improved combustion. Flow changes will affect mixing, stability, fuel and temperature distributions, and flame tube cooling (Lefebvre, 1983). A more detailed investigation will also be required to validate the conversion.

Gas injector requirements will be less stringent compared to the liquid injector, as the fuel does not require atomisation. The injection orifice/port will need to be enlarged because of the lower density.

The overall air-fuel ratio is large in gas turbines, and changes to the volumetric flow-rate will mostly have limited effect. However, the air-fuel ratio is nearly stoichiometric in the primary zone, where the effect will be most significant. The volumetric flow-rate of gaseous and liquid fuels will differ significantly at the injection point. However, if the fuels have similar calorific values, then the volumetric flow-rates will become similar as the liquid fuel evaporates.

3.3 Fuel control

If the switch to gaseous fuel has little affect on the combustion characteristics, then the adaptation/modification of the fuel controls might be the most challenging aspect of the conversion. It might be possible to use the original control system, otherwise a new system will be required.

The system could be partially or fully automated. Manual control runs the risk of operator error causing damage or injury. However, fully automated control requires careful consideration of all possible events. Automated throttling will be required to cater for an application with variable load, or to stabilise the turbine inlet temperature of a solarised gas turbine.

Regardless of automation, a mechanism is required to throttle the fuel from idle to full load. A few throttle options are discussed in Section A.5.3. The rate of change of the fuel rate should be limited to avoid a flame out and high transient temperatures. The fuel rate must be adjusted to ensure that the engine is operated within its limits; for example oil pressure and exhaust gas temperature.

On start-up, fuel should not be supplied until the engine has reached a certain speed, and the igniter has been actuated. The best way to address a flame out will depend on the engine application (aviation or industrial). The shut-down procedure should be considered. Large gas turbines require

gradual speed reduction to idle to allow thermal transients to pass, before shutting off the fuel supply (Saravanamuttoo *et al.*, 2009).

Engine faults and operator errors need to be considered in order to minimise risk. If the fuel is stored under pressure, then unintentional operation of the control valves could result in fuel being supplied to the engine when it is not running. If the fuel fails to ignite during start-up then liquid fuel might build up inside the engine, but gaseous fuel is more likely to be blown out of the engine and potentially form a combustible mixture in the exhaust.

3.4 Isolated combustor testing and modelling

The conversion of the fuel supply could be tested on an isolated combustor, before performing an engine test. Isolated tests avoid the risk of engine damage, and make it easier to instrument the combustor. The pressure drop, temperature and velocity distributions at the combustor outlet, and possibly the flame tube temperature are accessible for measuring.

Changes to the air and fuel flow within the combustion chamber will affect mixing, cooling and the outlet temperature distribution. A CFD model could be used to investigate the effects of the fuel conversion on the combustor flow. Cold flow testing, with a flow-field measurement technique, could be used to validate the combustion chamber design and to obtain additional data to support CFD computation. Refer to Section 2.3 for examples of hot and cold flow tests on an isolated combustor.

3.5 Engine tests

Ultimately engine testing will need to be performed to ensure that the conversion is successful. This includes testing the control system functionality. Long term performance (service intervals and component life) can be determined from endurance testing and scheduled inspections. Industry specific tests might be required. For example aviation engines must sustain combustion with large amounts of water entering the air intake.

3.6 Emissions

The most challenging requirement of modern gas turbine design is the reduction of emissions. If a clean fuel with high calorific value is used, and the flow regime and mixing changes insignificantly, then it is probable that the emissions will remain the same or be reduced. If the operation of an

engine must comply with emission standards, then emission testing will be required. Initial testing can be done with an isolated combustor.

4. Fuel Control System

4.1   Introduction

A Rover 1S/60 gas turbine was used for testing. The *original fuel system*, as supplied by the engine manufacturer, was designed to run on a liquid distillate fuel. Zhang (2016) used the original system to run the gas turbine on jet fuel. The system was not used in this research, but the data obtained by Zhang (2016) was used to analyse the engine and as comparison to the test results (Section 5.3 & 6.4).

After running tests on the original system, Zhang (2016) developed a system to run the engine on LPG. Zhang (2016) designed a *custom gas injector* to replace the original liquid atomiser. He intentionally limited the maximum fuel flow-rate by under-sizing the injector orifice, so that initial tests could be conducted safely. This resulted in the top speed being less than half the maximum speed, and no appreciable load could be applied to the engine.

This system was tested with LPG at the start of this research, and thus it is referred to as the *initial* or *LPG system*. The LPG was supplied from a 9 kg cylinder, and the valve on the cylinder was used to supply fuel during start-up. Once the engine speed stabilised, a needle valve was used to throttle the LPG. The original and initial systems are described in Appendix A.

In the current study the LPG system was improved for safe operation at the engine's design point, and tests were run on propane. It is referred to as the *final* or *propane system*. The ultimate goal was to run the engine on biogas, and the changes necessary to run the engine on biogas or natural gas are discussed in Section 4.4.

4.2   Requirements

The initial fuel system was modified to meet the following requirements:

- Provide safe fuel supply to the engine
- Match jet fuel performance results
- Throttle the fuel across a reasonable flow range, with gradual adjustment and control
- Be compatible with the engine test facility

Additionally, the following criteria were considered favourable, but non-essential:

- Low cost of capital
- Compatible with methane (natural gas/biogas)
- Ability to operate independently of the test equipment (e.g suitable for an industrial application)

4.3   Final system - propane

The initial system was modified to have increased and safer control over the range of fuel delivery, as was considered necessary before running the engine at its rated output. A previously installed gas line and two 48 kg propane cylinders, which were stored outside of the engineering building, were used.

The two cylinders were connected to a three-way (change over) ball valve, which facilitated gas flow from one or both cylinders into the supply line. Refer to the flow circuit in Figure 4.1. A list of devices has been included in the appendix (Table A.2).

1. gas cylinder
2. cylinder valve
3. three-way ball valve
4. ball valve
5. regulator
6. emergency shut-off
7. master valve
8. quick release valve
9. wall
10. control valve
11. venturi
12. remote shut-off
13. custom injector
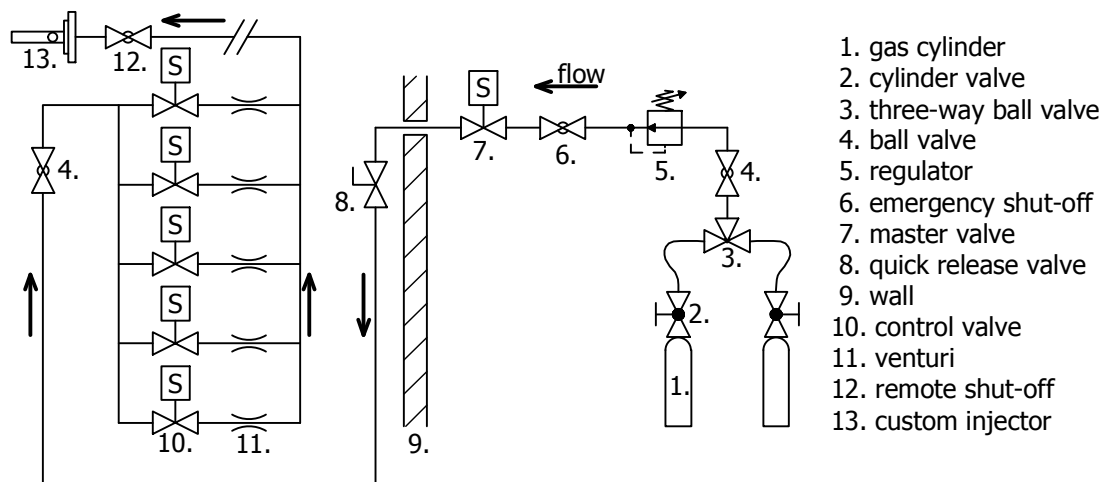
Figure 4.1: Final fuel system; test cell is to the left of the wall, and the outside to the right

A high pressure regulator was installed close to the cylinders for consistent supply pressure (which directly affects the injector flow-rate), and to reduce the risk of condensation within the gas line (by keeping the pressure below the saturation pressure). The regulator had a capacity rating of 230 kg/h for LPG, while it was calculated that the engine would require 36 kg/h of

propane. The difference in density and calorific value between LPG and propane are small, so the regulator would be more than adequate for the system. The intention was to set the regulator output to an absolute pressure of 600 kPa.

The fuel system was designed for an absolute pressure of 600 kPa, which has a corresponding saturation temperature of less than 8 °C. Ambient temperatures below 8 °C are uncommon in Stellenbosch (Stellenbosch University, [s.a.]), and the selected pressure was considered to be adequate.

There was already an emergency shut-off valve installed in the line next to an entrance to the building. This was a manually operated ball valve. In addition a *master* valve was installed in the line before it entered the test cell. The quick release valve from the initial system was relocated to just after the line entered the test cell, and could be shut from the control room.

The master valve was a normally closed solenoid valve, and would cut off fuel supply to the test cell in the event of a power failure, activation of the emergency-stop switch, automated shutdown due to critical sensor readings, or gas detection within the test cell. A gas detector was installed in the test cell, which would sound an alarm and close the master valve if 10 % of the lower explosion limit of LPG was detected.

A parallel network of five *control* solenoid valves was installed, and a venturi was inserted into each valve to regulate the flow-rate. A venturi with a 1.5 mm diameter was used for the pilot valve, while the other four control valves each had a 1.9 mm venturi. The effective diameter of the combined venturis was 4.09 mm. After successfully testing this configuration, the injector orifice was enlarged from 2 mm to 3.2 mm to allow more fuel flow. Refer to Section 5.2 for flow calculations.

When the initial system was tested, the copper tubing and brass fittings were found to heat up, and the thermocouple reading was seen to be affected. Because the flow-rate calculation depends on the fuel temperature, the flow-meter was moved further away from the combustor. Section 6.1 includes a description of the flow-meter.

Refer to Appendix A.5 for a description of the design decisions and alternative options that were considered.

4.4   Future system - natural or biogas

The final system successfully supplied the engine with propane, and could be adapted to work with natural or biogas with relative ease. A suitable

pressure regulator, and mechanism to heat the expanding gas, will need to be procured, as the inlet pressure limit of the current regulator is well below that of CNG (compressed natural gas). A suitable fuel tank would also need to be sourced.

A couple of CNG reducers for autogas systems (car conversions) were found with suitable outlet pressures for the Rover engine (up to 1000 kPa). They would be a good choice because they are suitable for natural gas, can handle the high inlet pressures for CNG, and include a mechanism for heating the expanding gas. Unfortunately no distributor was found.

The current supply line and valves could handle the full vapour pressure of propane up to a temperature of 45 °C. However, given the much higher pressures of CNG (20 MPa), additional safety measures may be required in case the regulator fails to maintain the correct supply pressure.

Methane has lower energy density than that of propane, and thus a higher mass flow-rate will be required to match the propane performance. This can be achieved with either larger orifice sizes or a higher supply pressure. A simple flow model indicated that equivalent performance could be achieved with methane at an absolute pressure of 870 kPa, to that of propane at 600 kPa, with the same orifice sizes (see Section 5.2).

Otherwise the rest of the system should be suitable for either fuel, as the valves and piping can all handle the different type of fuel and the slightly higher pressure (see Table A.2). The LPG detector, however, cannot detect methane, and it has been positioned at floor level, which is appropriate for LPG. A suitable methane detector should be installed at ceiling level.

There is a methane variant of the detector that could be connected to the LPG detector, such that if either detector is triggered, then the master valve will be shut. So by adding a methane detector at ceiling level, the facility would be able to detect either LPG or natural gas.

4.5   Discussion

The final control system met all of the requirements and most of the non-essential criteria (Section 4.2). The safety of the system was improved, and the flow-rate required to meet the engine specifications was quantified and successfully supplied to the engine. The flow was throttled to produce a range of flow-rates and engine operation states.

The solution was cost effective and worked well with the existing test facility. However, this system is not suitable for general (industrial) use, and relies

on the dynamometer controller to regulate the engine speed. Nonetheless, it is suitable to run on natural and biogas, apart from the fuel storage and regulator, which are only suitable for LPG and propane.

The final system utilised propane cylinders that were stored outside, which has the added benefit of removing the fuel from the control room. The fuel supply can be remotely and automatically shut with the master control valve, which was located away from the test cell hazards.

Although all of the requirements were met, there were still some operational limitations and installation difficulties. The control system was designed for an absolute supply pressure of 600 kPa. However, the cylinder pressure can drop below this value in midwinter or when the cylinder levels are very low. This problem was overcome by placing the cylinders in containers of water. Warm water was occasionally used in midwinter.

The propane system was considered to be an interim installation, because the ultimate goal was to run the engine on biogas. However, if LPG or propane is to be used for future testing, then it is recommended to install a vaporiser. A more detailed description can be found in Appendix C.1.

The greatest limitation with the fuel system was that the venturis were sized for a particular supply pressure. If the flow was too low with all of the valves open and the regulator pressure was increased to compensate, then the flow-rate for all valve combinations would increase.

In this regard a metering/proportional flow valve would have been superior, as the valve position can be adjusted to compensate for low or high supply pressure due to cold weather or adjustment of the pressure regulator. A proportional valve would also be a good choice if the system is to be automated. Refer to Appendix C.2 for more information.

A serious installation difficulty was the elimination of leaks in fittings. Copper pipes and brass compression fittings were used to construct the valve flow network, or manifold. The application of a drop of thread locker onto the ferrule was found to eliminate the leaks, and an illustration and description illuminating this aspect can be found in Appendix C.7.

No natural gas supplier was found in the Western Cape, which will make sourcing it difficult for future work. However, an anaerobic digester was being commissioned in Athlone, Cape Town, at the time of writing, from which biogas might be sourced. The company is called New Horizons Energy.

5. Thermofluid Analysis

This chapter covers the analyses of the engine and fuel supply. The engine analysis was used to evaluate test data, determine CFD boundary conditions, and to quantify the required fuel supply from engine specifications and test data. Analysis specific to the engine test data is described in Section 6.3.

5.1   Engine analysis

The following analysis was used to process test data, and to provide a comparison to the test results and engine specifications. The specifics of the comparative and test data analyses are detailed in Sections 5.1.1 and 6.3, respectively. The variable subscripts refer to the stages of the Brayton cycle as illustrated in Figure 2.5. The same subscripts were used for the engine instrumentation (Figure 6.1).

Assumptions

- Steady state
- Adiabatic inlet, compressor and turbine
- Perfect gases with the specific heats discussed in Section 2.6 (Saravana-muttoo *et al.*, 2009)
    - $c_{pa} = 1.005 \, \text{kJ/kg K}$, $\gamma_a = 1.40$
    - $c_{pg} = 1.148 \, \text{kJ/kg K}$, $\gamma_g = 1.333$
- Chemical equilibrium through turbine (gas species are frozen after combustor)
- Negligible potential energy
- Negligible exhaust back pressure; $p_4 \approx p_a$
- Parasitic loads (fuel & oil pumps) neglected

The exhaust back pressure was assumed to be negligible as there was a gap between the jet pipe (engine exhaust) and the flue (exhaust duct) that carried exhaust gases outside. Significant back pressure in the duct would result in exhaust flow into the test cell.

Stage equations

The compressor power for adiabatic compression is (Saravanamuttoo *et al.*, 2009),

$$\dot{W}_c = \dot{m} c_{pa} (T_{02} - T_{01}) \tag{5.1}$$

where $\dot{m}$ is the air mass flow-rate, c_{pa} is the specific heat of air, and T_{01} & T_{02} are stagnation temperatures. The change in kinetic energy is taken into account by using stagnation, rather than static, temperatures. When the kinetic energy is neglected, the static and stagnation temperatures are equal.

The turbine and compressor are coupled with a shaft running on rolling element bearings. Taking the mechanical efficiency of the shaft η_m into account, the power required to drive the compressor is (Saravanamuttoo *et al.*, 2009),

$$\dot{W}_c = \dot{m}c_{pa}(T_{02} - T_{01})/\eta_m \tag{5.2}$$

Similarly the turbine power (stage 3-4) is

$$\dot{W}_t = (\dot{m} + \dot{m}_f)c_{pg}(T_{03} - T_{04}) \tag{5.3}$$

where c_{pg} is specific heat of the combustion gases. The nett shaft power $\dot{W}$ is simply the difference between the power produce and consumed by the turbine and compressor, respectively.

$$\dot{W} = \dot{W}_t - \dot{W}_c \tag{5.4}$$

The thermal efficiency and the specific fuel consumption (SFC) were defined with Equation 2.27. The temperature rise across the combustor was calculated from the fuel-air ratio with Equation 2.26, which requires the combustor efficiency (Equation 2.2).

The ideal and actual change in temperature across the compressor and turbine depend on the pressure ratio, and efficiencies of both the compressor and turbine (Equation 2.18 to 2.20).

Pressure loss

The inlet stagnation temperature T_{01} is equated to the ambient temperature T_a, as the ambient air is effectively stationary and the air intake was assumed adiabatic. However, frictional losses through the air intake and filter will result in a stagnation pressure drop (Δp_i). Thus

$$T_{01} = T_a \qquad p_{01} = p_a - \Delta p_i \tag{5.5}$$

The combustor pressure drop Δp_b was specified as a fraction of p_{02} as it is dependent on the flow-rate.

$$p_{03} = p_{02} \cdot (1 - \Delta p_b/p_{02}) \tag{5.6}$$

5.1.1 Comparative analysis

The comparative analysis was used as a comparison to the test data, to evaluate the engine specifications, and to determine boundary conditions for CFD analysis. Test data, engine specifications, and values from literature were used as inputs to the comparative analysis.

The mechanical efficiency, η_m, of a directly coupled turbine and compressor is typically 99 %, $\Delta p_b / p_{02}$ is typically 2-3 % for an industrial turbine, and 6-8 % for an aeronautical turbine (Saravanamuttoo *et al.*, 2009).

An iterative solver was used for the comparative analysis, where any combination of parameters could be specified, as long as sufficient parameters were specified and a solution existed. The solver would return values for T_{02} and T_{03}, even when an algebraic approach indicated that it was not possible. The compressor and turbine efficiencies, which depend on T_{02} and T_{03}, would vary greatly for small changes in the input variables. There was also some uncertainty in the measured compressor outlet temperature (T_{02}). As a comparison to the measurements, the change in temperature across the compressor was calculated with the Stanitz slip factor (σ), and by assuming a power input factor (ψ) in Equations 2.24.

The velocity at different locations was determined from the continuity equation (Equation 2.17), by specifying the flow area and calculating the density at the point of interest. The results are presented in Section 5.3.

5.2   Fuel flow analysis

The fuel flow-rate was modelled to determine the required supply pressure and flow area to achieve various engine outputs. The initial LPG tests and jet fuel data from Zhang (2016) were used to quantify the fuel flow required at different operating points. The engine specifications (power and specific fuel consumption) were used to determine the upper limit required for fuel.

5.2.1 Approach

The fuel flow into the combustor was modelled to determine the required supply pressure and orifice size of the custom injector. The flow would be throttled upstream of the injector, and the effect of such a flow restriction was also modelled.

Once the multi-valve throttle mechanism had been selected, the model was used to size the valve orifices, which were used to regulate the flow-rate through the control valves. These were treated as a single restriction (point a

in Figure 5.1). Later on the orifices were replaced with venturis to improve the pressure recovery. For simplicity, they are commonly referred to as orifices or restrictions in this section.
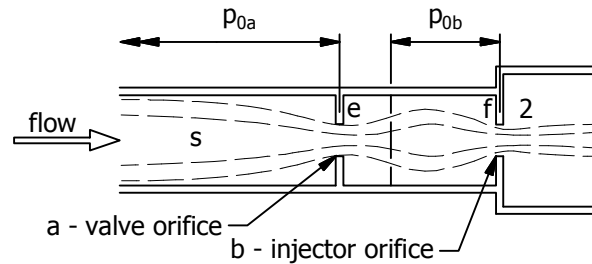
Figure 5.1: Simplified flow network

Point s refers to the supply line (and supply pressure) running from the gas cylinders. Points f and 2 refer to the fuel pressure (at the flow-meter) and combustor pressure, respectively, which are the same subscripts that are used in the engine testing and analysis sections. The fuel at b is injected into the combustor (2). The pressure at e (after the valve orifice) might differ from that of f due to shock waves after the orifice. This possible difference in pressure has been indicated by the vertical dashed line.

As was discussed for a converging-diverging nozzle (Section 2.6), once the flow has become choked, the mass flow-rate remains constant for further decreases in downstream pressure. If the upstream orifice chokes, then the downstream pressure is found from the conservation of mass and energy (Equations 2.17).

To account for subsonic pressure drop across the valve orifice, flow from the upstream pipe to the orifice was assumed to be isentropic, while the flow from the orifice into the downstream pipe was assumed to be adiabatic (but not isentropic). This has has been indicated in Figure 5.1 by constant stagnation pressure regions up to the orifices.

The flow from the upstream pipe to the injector orifice was also assumed to be isentropic. However, instead of calculating a pressure drop, the orifice pressure was assumed to equal the combustor pressure for subsonic flow. But once the flow choked, it would exceed the combustor pressure. Essentially the flow into the combustor was treated as a sudden expansion into a large reservoir, where all of the kinetic energy is dissipated (i.e. no pressure recovery).

Pressure losses in the pipe and the sudden contraction of the orifices are neglected by assuming that the flow upstream of the orifices is isentropic.

This is a reasonable assumption because the pipe diameter is much larger than the orifice diameter (refer to Table A.2), and because the pressure loss of the orifice is far greater on the expansion side than the reduction side (Miller, 1984).

The mass flow-rate will however, be overestimated from the isentropic assumption. It will also be overvalued if the orifice area is used as the narrowest restriction, because of additional throttling caused by a vena contracta (Miller, 1984). To account for this, the mass flow-rate was calculated with the vena contracta area A_{ca}, which will be smaller than the orifice area A_a. The relative area is expressed by the coefficient of contraction, $C_{ca} = A_{ca}/A_a$. The subscript a refers to the valve orifice, but the same would apply for b (the injector orifice).

Miller (1984) suggested looking up coefficients of contraction based on the flow geometry and for incompressible flow. A correction factor can be used to account for the compressibility. Initially this was done, and thereafter the coefficients were quantified from tests with compressed air. This resulted in better correlation between the predicted and measured flow of propane. Miller suggested that the coefficients could be used to estimate the loss of stagnation pressure,

$$K_0 = (1 - A_{ca}/A_e)^2 = (p_{0b} - p_{0a})/(p_{0a} - p_a) \tag{5.7}$$

5.2.2   Flow model

Assumptions
- Perfect gas (ideal and constant specific heat)
- The flow up to the orifices is isentropic (adiabatic and inviscid), but expansion from the valve to the downstream pipe is only adiabatic.
- The injector orifice pressure is equal to the combustor pressure until it chokes, thereafter it may exceed the combustor pressure.
- Orifice flow area reduced by vena contracta.
- Flow losses are negligible compared to the throttle restriction.
- The flow is steady state.

Equations

The following equation can be derived from the continuity, conservation of energy, ideal gas and isentropic equations (Miller, 1984), which were grouped as Equation 2.17.

$$\frac{\dot{m}\sqrt{RT_0}}{A_i p_{0i}} = \sqrt{\gamma} Ma_i \left(1 + \tfrac{1}{2}(\gamma - 1)Ma_i^2\right)^{-\frac{\gamma+1}{2(\gamma-1)}} \tag{5.8}$$

The mass flow rate $\dot{m}$ and stagnation temperature T_0 remains constant throughout the control volume, while all the other properties may vary with position (as indicated by the subscript i). The stagnation pressure p_{0i} will drop due to loses, which have been assumed to only occur as the flow exits the orifice. Otherwise the stagnation pressure will remain constant. To calculate the flow-rate through the orifice, the vena contracta area A_{ci} is used instead of the orifice area A_i.

As the flow exits the restriction, it will do so adiabatically and hence lose stagnation pressure. The adiabatic condition implies the same conservation of energy equation as before, but the isentropic equation does not apply. So additional information is required to determine the downstream state. The conservation of momentum was used for a sudden expansion, which has been illustrated in Figure 5.2 for simplified geometry. The resulting momentum equation will be

$$A_y(p_x - p_y) = \rho_y v_y^2 A_y - \rho_x v_x^2 A_x \tag{5.9}$$

The pressure immediately after the orifice (point x) has been assumed to be uniform, which is only valid for subsonic flow (i.e. before the orifice chokes). Substituting density with the ideal gas and isentropic process equations will give

$$\frac{p_x}{p_y} = \frac{1 + \gamma Ma_y^2}{1 + \gamma Ma_x^2 A_x / A_y} \tag{5.10}$$

If A_y is very large (like the combustion chamber), then $p_x \approx p_y$ since $Ma_y \approx 0$ and $A_x / A_y \approx 0$. Manipulation of the above equation together with the continuity, conservation of energy, ideal gas and isentropic equations can result in the following equation

$$\frac{p_{0x}}{p_{0y}} = \frac{A_y Ma_y}{A_x Ma_x} \left[\frac{1 + \frac{1}{2}(\gamma - 1)Ma_y^2}{1 + \frac{1}{2}(\gamma - 1)Ma_x^2} \right]^{-\frac{\gamma+1}{2(\gamma-1)}} \tag{5.11}$$
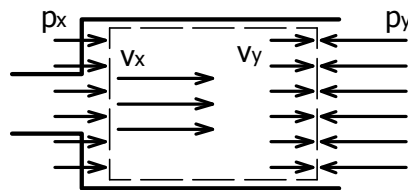
Figure 5.2: Sudden expansion

Moran and Shapiro (1998) use the same method to analyse the change of state across a shock wave, where the points x & y are located to either side of

an infinitesimally thin shock wave. They arrive at Equation 5.11, except that A_x and A_y are equal.

Equation 5.11 can also be obtained by equating Equation 5.8 for point x, with the same equation for point y, given that the mass flow-rates and stagnation temperatures will be equal. Thus Equation 5.11 is valid between any two points with equal mass flow-rate and stagnation temperature, which is why generic subscripts (x & y) have been used.

Despite being universally valid, acceptable results were only obtained by finding the change in stagnation pressure between the valve orifice and downstream pipe as long as the orifice was not choked. Therefore Equation 5.11 was used for points a & e, instead of x & y. If the valve orifice flow was subsonic, then the result was used (if $Ma_a < 1$ then $p_{0b} = p_{0e}$).

The orifice Mach numbers were limited to a value of one (Ma_a & $Ma_b \leq 1$). If the injector orifice Mach number was below one, then its pressure was equated to that of the combustor (if $Ma_b < 1$ then $p_b = p_2$). Otherwise injector pressure could be greater than that of the combustion chamber.

Four scenarios were solved with these equations, and then the realistic solution was used. The scenarios were for a choked condition at the first orifice, the second orifice, both orifices, or neither orifice. The first scenario, where $Ma_a = 1$, will be used as an illustration. If p_{0a}, T_0 and p_2 are specified, then $\dot{m}$ can be found with Equation 5.8,

$$\frac{\dot{m}\sqrt{RT_0}}{A_{ca}p_{0a}} = \sqrt{\gamma}Ma_a\left(1 + \tfrac{1}{2}(\gamma - 1)Ma_a^2\right)^{-\frac{\gamma+1}{2(\gamma-1)}} \tag{5.12}$$

where $A_{ca} = C_{ca}A_a$. Equations 5.11 & 2.15 can be used to solve for p_{0b} & Ma_b simultaneously,

$$\frac{\dot{m}\sqrt{RT_0}}{A_{cb}p_{0b}} = \sqrt{\gamma}Ma_b\left(1 + \tfrac{1}{2}(\gamma - 1)Ma_b^2\right)^{-\frac{\gamma+1}{2(\gamma-1)}} \tag{5.13}$$

$$p_{0b}/p_b = (T_0/T_b)^{\frac{\gamma}{\gamma-1}} = \left(1 + \frac{\gamma-1}{2}Ma_b^2\right)^{\frac{\gamma}{\gamma-1}} \tag{5.14}$$

where $A_{cb} = C_{cb}A_b$ and $p_b = p_2$.

5.3 Results

5.3.1 Results of the comparative engine analysis

The comparative analysis was run with various input data. Table 5.1 lists three key data sets that were used. The first row used the engine specifications for standard operating conditions (refer to Appendix A.2). The second

two rows used jet fuel test data from Zhang (2016), except for the intake
pressure loss (Δp_i), which was approximated from the current test data (see
Appendix B.4).

Table 5.1: Input parameters

Description	n [RPM]	$\dot{m}$ [kg/s]	p_a [kPa]	T_a [°C]	Δp_i [kPa]	p_{02} [kPa]	T_{04} [°C]	$\dot{W}$ [kW]
Engine specs	46 000	0.603	101.3	15.0	0.00	283.6	580.0	44.74
Peak power	39 270	0.525	99.9	46.7	0.75	251.3	686.3	38.99
No load	46 450	0.663	100.1	28.5	1.11	261.1	431.3	0.00

The impeller has a tip diameter of 164 mm and 17 vanes. The following
values were assumed for all of the scenarios; $\Delta p_b / p_{02} = 8\,\%$, $\eta_b = 98\,\%$,
$T_f = 25\,°C$ and $\Delta h_{25} = 43.69\,MJ/kg$ (see Appendix A.1).

Table 5.2: Results

Description	$\dot{m}_f$ [kg/h]	η [%]	η_c [%]	η_t [%]	p_{d2} [kPa]	p_{d4} [kPa]	v_4 [m/s]	T_{04} [°C]
Engine specs	37.1	9.93	69.1	86.4	0.14	1.6	81.0	766.3
Peak power	36.5	8.81	93.6	73.7	0.12	1.4	80.5	839.0
No load	26.1	0.0	66.2	78.5	0.19	1.6	74.5	557.3

The Overhaul Manual (1972) specifies the maximum specific fuel consumption, for standard operating conditions, as $0.852\,kg/kWh$. This implies a fuel
consumption of $38.1\,kg/h$. It thus seems reasonable that the calculated fuel
consumption for these conditions ($37.1\,kg/h$) was slightly lower than this
value; refer to the first row of Table 5.2.

The compressor efficiency is equal to the ratio of the isentropic to actual
temperature rise of air passing through the compressor (Equation 2.18).
The actual temperature rise was approximated with Equation 2.24. The
accuracy of this equation is clearly limited, because the computed compressor
efficiency varies significantly, and the value is unrealistically high for the
peak power data. Refer to Appendix C.4 for comparative values of efficiency.

The dynamic pressures at points 2 and 4 have been included in the table.
These were assumed to be zero when processing the test data, which is
covered in the next chapter. The exhaust gas velocity and temperature were
included, because other sections refer to these values.

5.3.2   Required fuel flow-rate

The required fuel flow-rate was determined from the engine specifications and test data. The comparative engine analysis was repeated with the values that were present in the last section, but with the calorific value of propane ($\Delta h_{25} = -46.0\,\text{MJ/kg}$).

A propane flow-rate of 35.22 kg/h was calculated to meet the engine specifications (44.74 kW at 46 000 RPM). While a flow-rate of 34.62 kg/h was calculated to match the peak power produced with jet fuel (38.99 kW at 39 270 RPM). The large difference in power output relative to the difference in flow-rates was attributed to the different engine speeds and air temperatures.

Data from the initial LPG tests were extrapolated to determine fuel flow-rates and combustion chamber pressures for different engine speeds with no load. The combustion chamber pressure was required as it affects the fuel flow-rate. Fitted curves were used to extrapolate data, and these were only slightly lower than the propane results obtained later. However, there was a lot of variance in the flow-rates at low engine speeds (refer to Figure 5.3). The following functions represent the fitted curves,

$$\dot{m}_f = 6.92 \times 10^{-9} n^2 + 9.58 \times 10^{-6} n + 7.21 \tag{5.15}$$

$$p_2 = 7.59 \times 10^{-8} n^2 - 7.66 \times 10^{-4} n + 105.9 \tag{5.16}$$

where $\dot{m}_f$ is in [kg/h], n is in [RPM], and p_2 is in [kPa].

The maximum required flow was set to achieve the rated power from the engine specifications. The function fitted to the LPG data was used to estimate the required flow for no load. A linear relationship between power output and fuel flow-rate was assumed to bridge the gap, as shown in Table 5.3.

Table 5.3: Required flow-rate

n [RPM]	$\dot{W}$ [kW]	$\dot{m}_f$ [kg/h]	p_2 [kPa]
10 000	0	8.00	105.8
20 000	0	10.17	121.0
30 000	0	13.73	151.3
40 000	0	18.67	196.7
46 000	0	22.30	231.3
	15	26.63	
46000	30	30.96	283.6
	45	35.30	
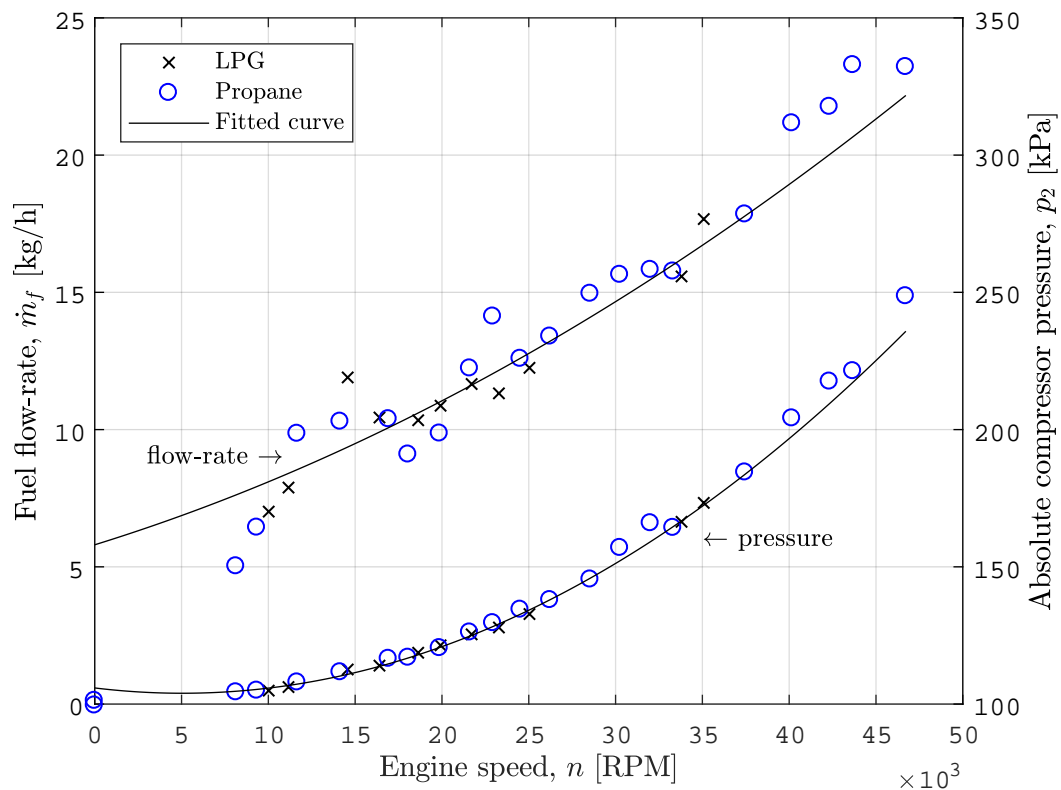
Figure 5.3: Extrapolation of LPG test data

5.3.3   Results of the fuel flow analysis

LPG and initial propane tests used the initial gas injector (2 mm orifice). The injector and valve orifices were then sized to give a fuel range of 7.6 to 35.5 kg/h (with $p_{0a} = 600$ kPa & $T_0 = 20\,°C$). The valve orifices were of different sizes, allowing different flow-rates depending on the combination of open valves. At most the change in flow-rate was expected to be 7.6 kg/h, however, a needle valve was used to gradually adjust the flow.

The coefficients of contraction for orifice plates were used to estimated the orifice values (Miller, 1990, Figure 14.2). These values were adjusted for compressible flow (Miller, 1984, Figure 14). The coefficient from test data with the 2 mm injector was close to 1, and this value was used when determining the new injector size.

Table 5.4 summarises the estimated values, versus those measured with compressed air. The combined row represents a single orifice equivalent to opening all of the valves. An area weighted average was used to estimate contraction coefficients for valve combinations.

Table 5.4: Orifice coefficients of contraction

	Diameter [mm]	Contraction coefficient Estimated	Measured
Small	1.2	0.74	0.889
Pilot	1.5	0.74	0.901
Large	1.9	0.76	0.762
Max	3.0	0.77	0.455
Injector	2.9	1.00	0.827
Combined	4.04	0.76	0.429

The injector and maximum orifice coefficients were overestimated. The injector orifice could easily be enlarged to compensate, while the valves were found to have an internal flow restriction of 3 mm in diameter, which was unexpected given their 6 mm ports. This resulted in poor flow characteristics (flow-rate & pressure recovery) relative to the orifice size, and the combined flow was capped at 27 kg/h, instead of the predicted value of 35 kg/h for the same conditions.

A second iteration was done, where the valve orifices were replaced with simple venturis in order to improve the pressure recovery, while achieving the same throttling effect under choked conditions. The venturi sizes were also kept well below the valve restriction size (3 mm), as high velocities within the valve would result in greater pressure loss.

An additional valve was added to compensate for the smaller venturi sizes. A 1.5 mm pilot venturi, and four 1.9 mm venturis were selected. This selection was expected to provide flow between 8.2 and 36 kg/h. Venturi contraction coefficients were assumed to be 0.8, slightly more conservative than those measured for the same sized orifices, while it was assumed that the injector orifice coefficient would remain constant. Table 5.5 shows the results.

Table 5.5: Venturi coefficients of contraction

	Diameter [mm]	Contraction coefficient Estimated	Measured
Pilot	1.50	0.80	0.820
Equal	1.90	0.80	0.750
Injector	3.20	0.826	0.81
Combined	4.09	0.80	0.61

The coefficients were again measured with compressed air flow, and, using these valves, the propane flow would be capped at 33.7 kg/h. This was

just short of the desired flow-rate, and was overcome by increasing the supply pressure at the regulator. These sizes were considered adequate to supply the desired flow range with reasonably small increments. The system performance was discussed in Section 4.5.

5.4   Discussion

The engine cycle analysis was used to gain insight into the engine's performance. The engine specifications were used as a comparison to the test data. The flow areas at the jet pipe and compressor outlet pressure measurement point were used to justify neglecting the kinetic energy in the test data analysis (Section 6.3).

The model was used to quantify the combustor temperatures for CFD modelling. The compressor temperature rise was approximated with Equation 2.24, as there was uncertainty surrounding the representativeness of the measured values (discussed in Appendix C.4). However, the calculated compressor efficiency is unrealistic for low speed.

The model could be improved by finding an approximation to the turbine efficiency and combustor pressure drop, instead of relying on the compressor efficiency approximation and a typical pressure loss factor. Parasitic loads, such as the fuel and oil pumps, were not considered, but might be significant given the low thermal efficiency of the engine.

The model was used to determine the equivalent propane flow-rate. The engine operation and combustion efficiency were assumed to be the same for the different fuels. The equivalent flow-rates depend on the respective calorific values, and essentially were found from the combustor energy balance (Equation 2.26). Given the high air to fuel ratio, and the similar calorific values of the different fuels, a similar answer could have been obtained by simply equating the supplied heat (chemical energy); $\dot{Q}_{in} = \dot{m}_a q_{f,\,a} = \dot{m}_b q_{f,\,b}$.

For example, a 35.22 kg/h flow-rate of propane was calculated from the engine analysis. Scaling the equivalent jet fuel value with the above equation results in a flow-rate of 35.24 kg/h, which is a negligible difference given the much larger modelling assumptions.

6. Engine Testing

6.1   Apparatus

The Rover gas turbine was coupled to a dynamometer, and they were set up in a *test cell* (engine room). Tests were operated from a control room that overlooked the test cell. The dynamometer controller regulated the engine speed by adjusting the load. Refer to Table B.1 in the appendix for product details.

The engine and dynamometer were monitored and controlled with a computer via a PLC (programmable logic controller) and dynamometer controller. A software package called ETA (Engine Test Automation) provided a user interface, and could display and record sensor readings. Extension modules connected to the PLC provided sensory inputs.

ETA controlled the starter motor and ignition relays, and adjusted the dynamometer's speed set point. Automated procedures were also configured within ETA, such as shutting down the engine if a critical temperature was reached.

Instrumentation

Temperatures and pressures were measured at several points as shown in Figure 6.1 and Table 6.1. The dynamometer speed and torque were measured with a shaft encoder and a load cell, respectively.

The air and fuel flow-rates were determined from the dynamic pressure in the bell mouth air inlet and the venturi in the fuel line, respectively. The relevant equations are introduced in Section 6.3.

The limit to the number sensors that can be connected to the PLC was reached. An additional data acquisition device will be required to increase the number of simultaneous measurements. Alternatively, if similar tests are run with different measurements, then the common measurements can be used to compare and overlay the data sets. This was done to estimate the intake pressure loss (refer to Appendix B.4).

Calibration

Sensors were calibrated across a range greater than that expected during engine testing, and often less than the sensor range. Calibration data was en-
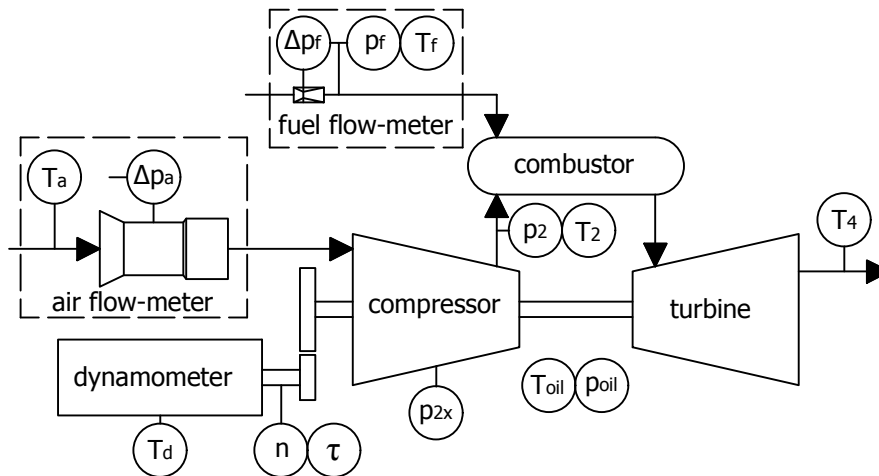
Figure 6.1: Engine instrumentation

Table 6.1: Sensor selection

Variable	Description	Product
n	Dynamometer shaft speed	Rheintacho Type 5515 shaft encoder
τ	Dynamometer torque	Wägezelle load cell Type U2A
Δp_a	Inlet pressure differential	Wika Air2Guide Model A2G-50
p_{2x}	Impeller tip pressure	
p_2	Diffuser outlet pressure	Wika Model A-10
p_{oil}	Oil pressure	
p_f	Fuel pressure	
Δp_f	Fuel pressure differential	Foxboro Model 823DP-I3K1NM2
T_a	Air intake temperature	
T_2	Diffuser outlet temperature	K-type thermocouple
T_4	Exhaust temperature	
T_{oil}	Oil temperature	
T_f	Fuel temperature	J-type thermocouple
T_d	Dynamometer cooling water	

tered into ETA, which applied linear interpolation or regression to determine sensor readings for display and data logging. Measurement uncertainties were quantified by considering the rated accuracy of the sensor and the calibration equipment. Refer to Appendix B.3 for more detail.

6.2   Procedure

The engine test procedure was straight forward. The dynamometer controller was set to speed control, where it would regulate the braking load to match the dynamometer shaft speed to the set-point specified in ETA. A set-point of 3100 RPM would be entered before starting the engine. This value equates to a turbine shaft speed of $47\,532$ RPM[1], which is slightly larger than the governed speed that the original engine would reach with no-load ($47\,000 \pm 500$ RPM).

The igniter would be turned on once the starter motor brought the turbine up to 6000 RM, and the pilot valve would be opened once the turbine speed was between 7000 and 8000 RPM. If the fuel was successfully ignited, the engine would quickly accelerate to $10\,000$ RPM, at which point the starter relay would be opened. If the engine continued to accelerate, and the exhaust gas temperatures were indicative of combustion, then the igniter would be turned off.

Once the engine speed stabilised, further control valves would be opened to allow for gradual spooling up, until the top speed was reached ($47\,000$ RPM). No load would be applied if the actual speed was less than the set-point. Once the engine readings had stabilised, the dynamometer speed set-point was reduced to 3000 RPM, equivalent to the rated on-load speed of the turbine ($46\,000$ RPM). Then further control valves were opened, and the dynamometer would increase load to counter the increased fuel flow.

In the case of LPG tests, which were done initially, the only throttle mechanism was a needle valve. The engine was started with the needle valve fully open, and once the engine reached the top speed that could be achieved with the LPG configuration, the fuel could be throttled back to run the engine at lower speeds. The engine was started on full throttle as the flow-rates for other positions, as well as the implications of starting the engine with inadequate fuel supply, were unknown.

6.3   Data analysis

The engine test data were analysed with the thermodynamic model (Section 5.1), but additional calculations and assumptions were required. The jet fuel data from Zhang (2016) were also analysed for comparison. The test instrumentation was discussed in Section 6.1, and the following parameters were

---

[1]The turbine and engine output shafts were coupled through a 15.3:1 reduction gearbox.

- Known: Δp_a, $p_{2x,gauge}$, $p_{2,gauge}$, $p_{f,gauge}$, Δp_f, T_a, T_2, T_4, T_f, $\dot{W}$
- Unknown: p_a, Δp_i, p_3, p_4, T_1, T_3

Additional assumptions

- Negligible kinetic energy, $p_0 = p$ & $T_0 = T$
- Constant combustor pressure, $\Delta p_b = 0$
- Frictional shaft power losses neglected, $\eta_m = 1$
- Jet fuel temperature, $T_f = 25\,°C$

Barometric data from a Stellenbosch weather station was used for the ambient pressure (p_a). The intake pressure drop Δp_i was only measured during two tests, the results of which were used to estimate the compressor inlet pressure for all of the other tests (see Appendix B.4). Gauge pressures were changed to absolute values by adding the ambient pressure,

$$p_{abs} = p_a + p_{gauge} \tag{6.1}$$

Flow-rates

The air flow-rate was determined from the pressure differential (Δp_a) between the ambient air and the throat of the bell-mouth inlet (air flow-meter). The air intake and flow-meter were designed by Prinsloo (2008). The following equation was used to calculate the mass flow-rate $\dot{m}$,

$$\dot{m} = 0.25\pi \cdot \alpha\varepsilon \cdot d_t^2 \sqrt{2\rho_a \cdot \Delta p_a} \qquad \alpha\varepsilon = 0.96,\ d_t = 0.11\,\text{m} \tag{6.2}$$

where $\alpha\varepsilon$ is the compound coefficient, d_t is the throat diameter, and ρ_a is the ambient air density. Prinsloo (2008) stated that the accuracy of the compound coefficient is $\pm 1.5\,\%$ for $Re > 300\,000$, which equates to a mass flow-rate greater than 0.46 kg/s. The air flow-rate is 0.603 kg/s at the design point (refer to Appendix A.2). The low speed accuracy is unknown. The density was calculated from the ambient air temperature and pressure with the ideal gas law ($\rho_a = p_a / R_a T_a$).

Similarly the flow-rate of propane was determined from the change in pressure from the fuel supply line to the throat of a venturi (Δp_f),

$$\dot{m} = C_d Y_a A_d \sqrt{\frac{2\rho_f \Delta p_f}{1 - \beta^4}} \qquad A_d = 0.25\pi d_f^2,\quad \beta = d_f / D_f \tag{6.3}$$

The coefficient of discharge was determined from the calibration process; $C_d = 0.929 \pm 0.020$. A_d is the flow area of the venturi throat, and β is the ratio of the venturi throat diameter to the pipe diameter; where $d_f = 4.6\,\text{mm}$

and $D_f = 6.3\,\text{mm}$. Y_a is the compressibility factor, which accounts for the density variation through the venturi,

$$Y_a = \left[r^{2/\gamma} \left(\frac{\gamma}{\gamma - 1} \right) \left(\frac{1 - r^{(\gamma-1)/\gamma}}{1 - r} \right) \left(\frac{1 - \beta^4}{1 - \beta^4 r^{2/\gamma}} \right) \right]^{\frac{1}{2}} \tag{6.4}$$

where r is the ratio of venturi to upstream pressure, $r = (p_f - \Delta p_f)/p_f$; and γ is the specific heat ratio. In the test data Y_a ranged between 0.97 and 1. Equations 6.3 & 6.4 were taken from Fluid Meters (1959). The fuel density ρ_f was determined from temperature and pressure measurements upstream of the venturi (T_f & p_f). Property data was interpolated to determine the density and specific heat ratio, except for the use of the ideal gas law for air and LPG.

Jet fuel data

Zhang (2016) stated that it was not possible to record the jet fuel flow-rate. The flow-rate data had large fluctuations, with a vague correlation to the engine operation. The fluctuations had a large periodicity, and could not be filtered out without losing relevant flow variations. Thus the flow-rate data were not used in this study.

The fuel temperature was assumed to be 25 °C for the jet fuel tests, because it was not recorded. This effectively neglects the difference in enthalpy at the actual fuel temperature and at 25 °C, which will be small compared to the calorific value of the fuel (see equation 2.26).

Compressor outlet temperature, T_2

The compressor power was calculated from T_1 & T_2, allowing the calculation of the turbine power from the nett power $\dot{W}$, and then finally the calculation of T_3. Having calculated T_3, and measured the pressure ratio, the turbine and compressor isentropic efficiencies were calculated. However, T_2 data did not appear representative (as discussed in Section 6.5), hence these calculated values are questionable.

Combustion

A fuel flow-rate was calculated to determine the combustion efficiency, and as a comparison to the measured flow-rate. Initially Equation 2.26, which relates the fuel flow to the combustor temperatures T_2 & T_3, was used to calculate $m_{f,\,calc}$. However, due to concern over the validity of T_2, and thus also T_3, these were substituted by $\dot{W}$ (with Equations 5.2 & 5.3). This was only possible by assuming that $\eta_m = 100\,\%$. In hindsight, the two routes are effectively the same.

The fuel flow-rates in the resulting equation were changed to the calculated value, so that the calculation was independent of the measured flow-rate. This was necessary in order to process the jet fuel data, given the invalid fuel flow-rate data. The resulting equation was

$$\dot{m}_{f,\,calc} = \frac{\dot{W} + \dot{m}c_{pg}(T_4 - 298) + \dot{m}c_{pa}(298 - T_1)}{c_{pg}(298 - T_4) - \Delta h_{25} + c_{pf}(T_f - 298)} \qquad (6.5)$$

The heat of combustion was calculated from the measured fuel flow-rate, $\dot{m}_f$ (when available). Otherwise the calculated value, $\dot{m}_{f,\,calc}$, was used. Similarly for the thermal efficiency.

$$\dot{Q}_{in} = -\Delta h_{25} \cdot \dot{m}_f \qquad\qquad \dot{Q}_{in,\,calc} = -\Delta h_{25} \cdot \dot{m}_{f,\,calc} \qquad (6.6)$$

$$\eta = \dot{W}/\dot{Q}_{in} \qquad\qquad \eta_{calc} = \dot{W}/\dot{Q}_{in,\,calc} \qquad (6.7)$$

Data selection & averaging

Tabulated values in the results section are average values for short time intervals, where the engine operation was close to steady state. Some measurements were prone to signal noise, necessitating averaging. Where appropriate, the standard deviations have been indicated.

Comparison of results requires steady engine operation at the same speed and load, with similar ambient conditions. Temperature measurements required more time to stabilise than other measured parameters, due to the thermal capacitance of the engine and thermocouples.

Uncertainty analysis

Measurement accuracy was quantified as part of the calibration process, and this was used in an uncertainty analysis of the test data calculations (refer to Appendix A). The uncertainty in the specific heat values were assumed to be zero.

6.4   Results

The Rover engine was first run on LPG using the initial fuel control system, and the results closely match those of Zhang (2016). The control system was then changed and the engine was run on propane. To begin with, the fuel flow-rate was still limited, but orifice sizes were gradually increased, as described in Section 5.3.3, until the target flow-rate was achieved.

Figure 6.2 illustrates a typical test result. The dynamometer speed set-point, $n*$, was initially set just above the top speed rating. Once the engine was

up to speed, the speed set-point was reduced (at $t \approx 120 \; s$), resulting in the dynamometer applying a braking torque τ. The throttle was fully opened, resulting in a further increase in torque, before the speed set-point was reduced further, resulting in the three largest torque peaks ($t \approx [170; 200] \; s$).
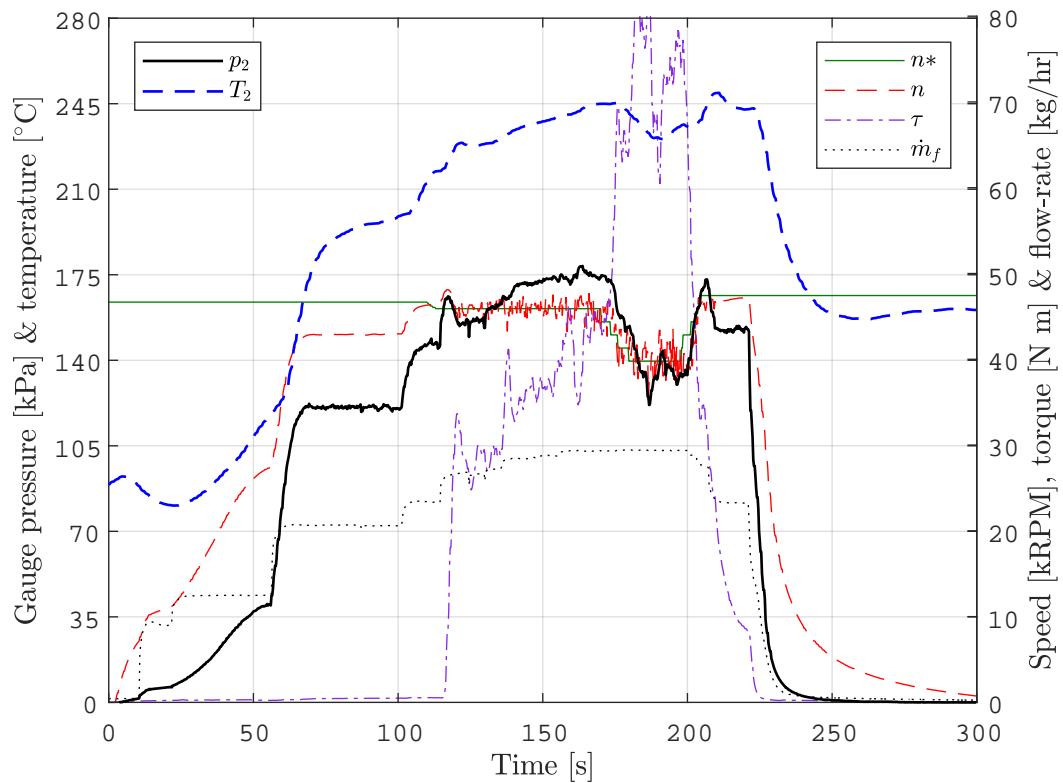
Figure 6.2: Typical load test result with propane

The engine was successfully run on propane up to its top speed, and produced a peak power output of 34.35 kW. Table 6.2 contains a few variables for on-load and no-load test conditions (see Table B.5 in the appendix for all the variables). The average and the standard deviation for a two second time interval are shown, together with the typical values listed in the Rover documentation (see Appendix A.2). The on-load data is the moment when the peak power was produced, and the no-load data is for top speed operation. Most of the measured parameters are close to the typical values, although the on-load engine speed was slightly below the rated range. The excessive exhaust gas temperatures (T_4) were of great concern.

Table 6.2: Analysis results

Var	Units	On-load			No-load		
		Mean	Std dev	Typical	Mean	Std dev	Typical
n	kRPM	45.2	± 1.8	45.5 to 46.5	47.2	± 0	46.7 to 47.3
T_1	°C	37.3	± 0.2	-55 to 50	37.8	± 0.2	-55 to 50
T_4	°C	663	± 0.6	< 610	471	± 0.4	< 400
ΔT_4	°C	72	± 0.3	< 150	87	± 0.4	< 150
p_a	kPa	100		58 to 101	101.5		58 to 101
Δp_i	kPa	1.2	± 0.09	0 to 0.5	1.2	± 0.03	0 to 0.5
p_2	kPa	202	± 1.4	179 to 214	160	± 0.5	179 to 214
$\dot{W}$	kW	34.4	± 1.8	0 to 44.74	-0.2	± 0.0	0
$\dot{m}_a$	kg/s	0.686	± 0.025	0.603	0.678	± 0.009	0.603
$\dot{m}_f$	kg/h	41.5	± 0.07		28.0	± 0.03	
$\dot{m}_{f,calc}$	kg/h	42.1	± 1.3		26.8	± 0.4	
η	%	6.5	± 0.3		-0.1	± 0.0	
η_c	%	47	± 0.3		51	± 0.3	
η_t	%	88	± 1		86	± 0.3	
T_{oil}	°C	95	± 0.2	< 110	52	± 0.3	< 110
p_{oil}	kPa	138	± 0.4	110 to 124	167	± 0.8	124

All pressures are gauge except for p_a.

High exhaust gas temperatures

The no-load exhaust gas temperature (EGT) is not a problem in itself, but rather a possible indication of a problem elsewhere. The maximum intermittent EGT, which was specified as 610 °C in the Maintenance Manual (1967), was exceed before reaching the rated power with both propane or jet fuel (refer to Table 6.3). The manual warns that high EGT is indicative of excessive load, however, the power produced is well below the rated power.

High exhaust temperatures were often noted during start up, as additional fuel was required to accelerate the engine. The temperature tended to drop at higher speed, under steady state and no load. Start up temperatures were not specified in the Rover documentation. However, once stabilised, the exhaust temperatures were high compared to those in the Engine Catalogue [s.a.] for similar power or fuel flow-rate.

Figure 6.3 is an illustration of the high start-up and stabilisation of the EGT. The curves have been normalised by the range of all test data. The range of the plotted data has been included in the legend.
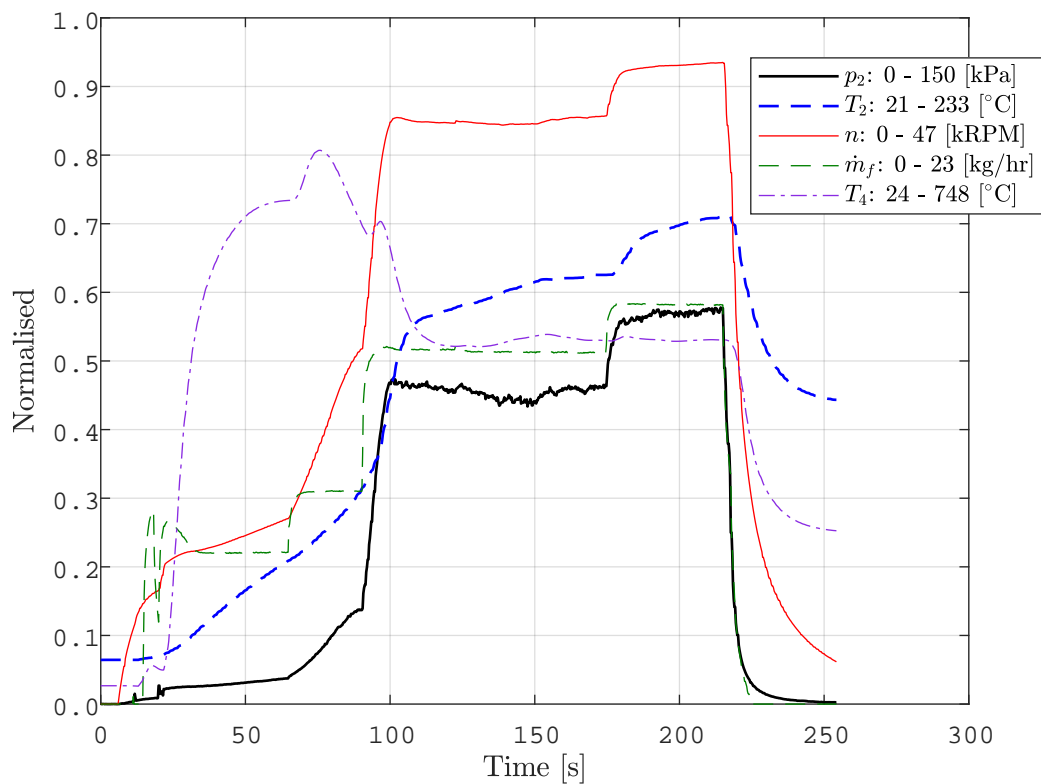
Figure 6.3: Normalised plot of a propane test without load

Power output

Table 6.3 contains the peak power and relevant conditions produced with the two fuels. The rated power under standard operating conditions is included for comparison, which specifies a speed of 46 000 RPM. However, the peak power for both the jet fuel and propane tests occurred at slower speeds. The engine was underpowered in both tests, and the exhaust temperatures were higher than expected. However, it is not a fair comparison, due to the different inlet temperatures and engine speeds.

The Engine Catalogue [s.a.] contain performance charts for different ambient and exhaust temperatures at the design speed (46 000 RPM). Table 6.4 includes the peak power output of the test data near the design speed, and comparative data interpolated from the performance charts. The chart power output has been reduced by 1 % for altitude and a further 1 % for every 0.25 kPa intake pressure drop. The fuel density and calorific value were assumed in order to make use of the engine specifications and performance charts (refer to Appendix A.2).

Table 6.3: Rated power under standard operating conditions, and peak power data with uncertainties

Variable	Units	Engine specs	Jet fuel[1]		Propane	
n	RPM	46000	39270	±100	45180	±100
p_a	kPa	101.3	99.9	±0.2	100.0	±0.2
Δp_i	kPa	0	0.8		1.2	
T_a	°C	15	47	±2	37	±2
T_4	°C	580	686	±200	663	±70
ΔT_4	°C	< 150	182	±10	72	±10
$\dot{Q}_{in}$	kW	462	434	±100	530	±20
$\dot{W}$	kW	44.74	39.0	±0.4	34.4	±0.5
η	%	9.88	9.0	±2	6.5	±0.2

[1] $\dot{Q}_{in}$ & η are calculated from an energy balance, and not from measured flow-rate.

Table 6.4: Performance chart data, and peak power at $46\,000 \pm 500\,$RPM with uncertainties

Variable	Units	Chart	Jet fuel[1]		Chart	Propane	
n	RPM	46000	45510	±100	46000	45600	±100
p_a	kPa	101.3	100.1	±0.2	101.3	101.5	±0.2
Δp_i	kPa	1.0	1.0		1.2	1.2	
T_a	°C	32	32	±2	38	38	±2
T_4	°C	497	497	±100	541	541	±70
ΔT_4	°C	150	125	±10	150	73	±10
$\dot{Q}_{in}$	kW	376	359	±100	396	432	±20
$\dot{m}_f$	kg/h	31	30	±8	33	34	±1
$\dot{W}$	kW	24.4	10.9	±0.5	27.8	14.5	±0.5
η	%	6.5	3.0	±0.8	7.0	3.3	±0.2

[1] $\dot{Q}_{in}$ & η are calculated from an energy balance, and not from measured flow-rate.

Chart performance

Chart performance curves and test data are shown in Figures 6.4, 6.5 & 6.6. The same test data are shown in the different figures, and are for engine speeds within 500 RPM of the design speed from several tests on different days. Plots of fuel consumption are in equivalent propane rates based on calorific values. The jet fuel flow-rates are calculated from an energy balance, as measured values were not available. These values are best compared with the calculated propane flow-rates, which are shown together with the

measured propane values.
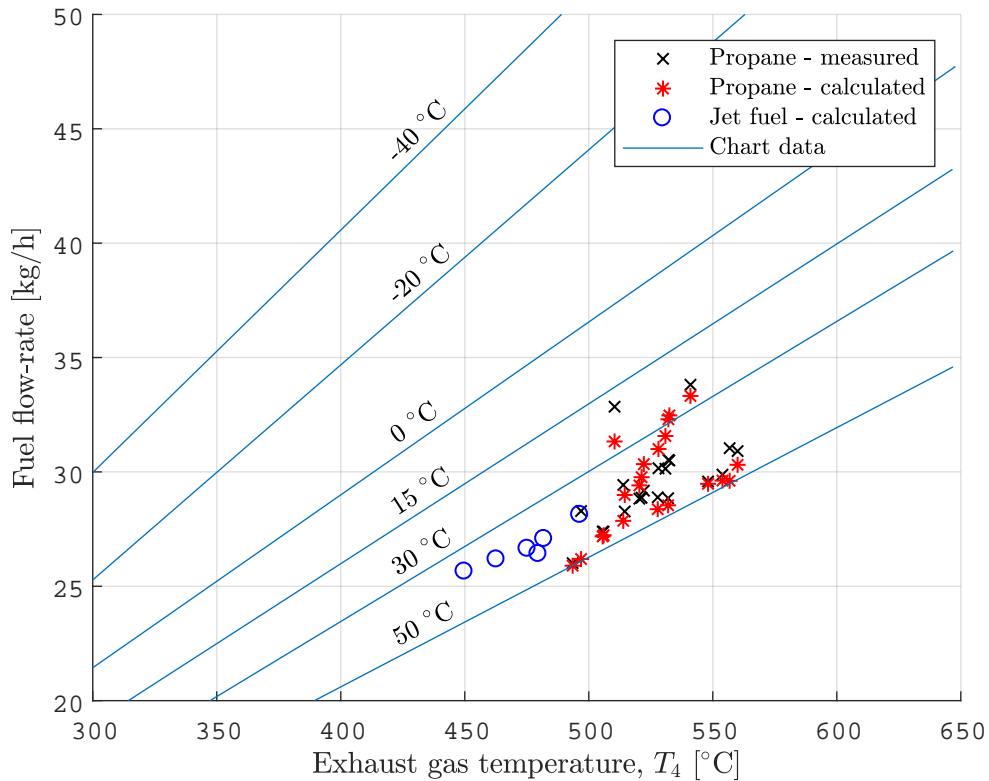
Figure 6.4: Propane equivalent fuel consumption vs EGT ($46\,000 \pm 500\,$RPM)

The use of error bars to show the exhaust gas temperature or calculated mass flow-rate uncertainty, made the plots unclear and cluttered. This is due to the large uncertainty of the exhaust gas temperature, which was used to calculate the flow-rates.

The ambient temperatures are indicated on the performance curves. The calculated jet fuel flow-rates are a bit lower than expected, given inlet temperatures between 26.7 and 32.3 °C. The propane flow-rates mostly fell within the expected region, given the broader inlet temperature range of 29.1 to 49.6 °C. Initially the inlet temperatures were indicated on the plots by the size or colour of the markers. However, while some data points followed the expected trend of lower consumption for higher inlet temperatures, overall no trend was apparent. Thus the inlet temperatures are not indicated.

The chart power curves were for an ambient pressure of 1 atm and zero intake pressure loss. So the test data power were increased by 1 % for altitude and a further 1 % for every 0.25 kPa intake pressure drop (refer to Appendix A.2).
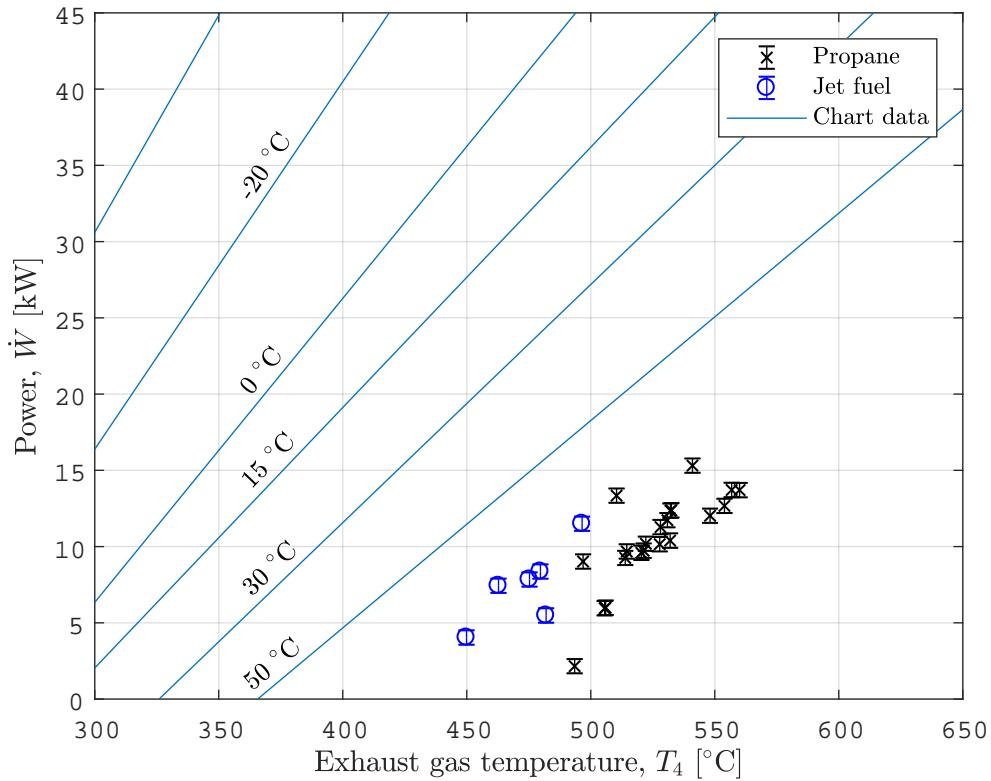
Figure 6.5: Power, with error bars, vs EGT ($46\,000 \pm 500\,\text{RPM}$)

The power output was well below what was expected given the EGT (see Figure 6.5). It appears as though jet fuel tests marginally outperformed the propane tests in this regard. It is unclear whether this was due to differences in calibration, position of the exhaust duct (which may affect EGT measurements), or engine condition. It was considered unlikely that the change in fuel should cause a shift in power for the same EGT.

The curves of fuel consumption and power versus exhaust gas temperatures (EGT) were combined to produce fuel consumption versus power curves (see Figure 6.6). The measured propane data points, which are independent of the EGT, indicate that the engine underperformed. The inlet temperature is less significant with regards to the combined curves, as can be seen by their overlap, and hence the inlet temperatures were only indicated for the top and bottom curves.

Unsteady speed and load

The engine speed measurement became noisy when load was applied, which is evident in Figure 6.2. As the measured speed (*n*) fluctuates around the
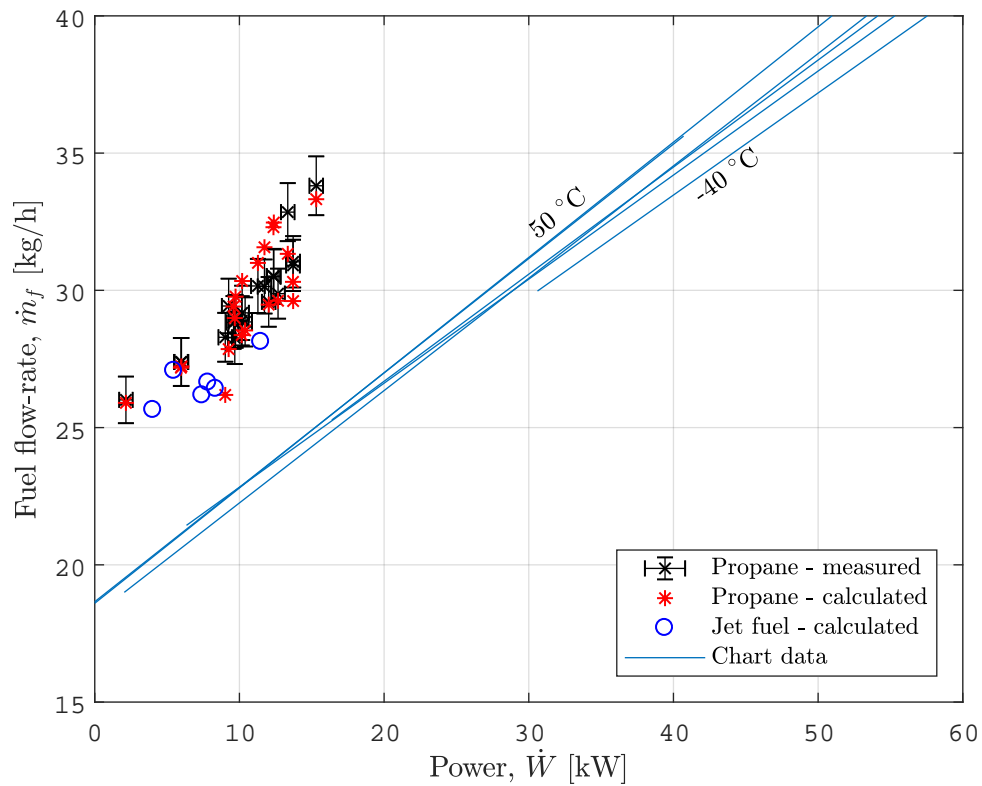
Figure 6.6: Propane equivalent fuel consumption vs power($46\,000 \pm 500\,\text{RPM}$), with error-bars for the measured flow-rate data

speed set-point ($n*$), the dynamometer tries to compensate by adjusting the torque(τ), which also fluctuates, but at a lower frequency. The speed variation is too rapid to be representative of the true speed; although the dynamometer might be able to rapidly slow the engine, the engine would be unable to recover as quickly as the data suggests.

6.5   Discussion

The propane results are considered to successfully match the jet fuel results, within the operational limits of the engine. More power was produced with jet fuel than propane at part speed (Table 6.3). Near the design speed, however, more power was produced with propane (Table 6.4).

Fuel flow-rates

The propane peak power was produced with full throttle, and changes to the fuel system would be required to produce more power. However, this would result in even higher exhaust temperatures, which could lead to

engine damage. A target flow-rate of 35 kg/h was determined from the engine specification in order to produce the rated power, while 41.5 kg/h was supplied to produce 76% of rated power (peak power produced).

The jet fuel peak power was produced well below the design speed. This might be due to faulty or incorrect adjustment of the governor. If incorrectly set, then insufficient fuel fuel would be supplied at the design speed to produce full power. However, given the underperformance with propane, this seems unlikely.

Validation

The engine clearly underperformed compared with the engine specifications and performance charts. The power output was low for the fuel consumption and the exhaust gas temperature (EGT). The engine speed and fuel flow-rate measurements, and the compressor inlet pressure were checked to see if they were the cause.

At the rated turbine speed (46 000 RPM), the output shaft could be 3000 or 3600 RPM, depending on the engine variant. Because the output shaft speed was measured, and not the turbine speed, it was possible to run the engine at the incorrect speed if the gear ratio was mistaken. The gear ratio was however confirmed to be correct (15.33:1).

The engine speed measurement became noisy when load was applied. It was unclear how much fluctuation was due to electrical noise, and how much as actual engine speed variation. A secondary device was used to verify the speed measurement. The speeds were found to closely match while no load was applied, but once load was applied, the regular measurement under-read by as much as 15 %. Thus the calculated power output could be 15 % below the true reading. Refer to Appendix C.3 for more information and recommendations.

The pressure drop across the air intake duct was not initially measured. Instead the pressure loss was estimated from the loss coefficient reported by Prinsloo (2008), who designed and tested the ducting. Although the air filters and ducts had been inspected before testing, the pressure loss was measured once the the engine was seen to underperform. The pressure loss was found to be about half that measured by Prinsloo (refer to Appendix B.4). The test results were adjusted for the pressure loss in accordance with the Maintenance Manual (1967), as indicated in the results section.

The fuel flow-meter was initially calibrated with a commercial flow-meter, which had a fairly large uncertainty. The flow-meter was then re-calibrated with a venturi flow-meter, which reduced the calibration uncertainty. The

calibration curves overlap for high flow-rates, which is of more importance. However, they differ for low flow-rates (refer to Appendix B.3).

The power output was about half of the chart values for the same operating conditions (refer to Table 6.4). The measured power might be undervalued by 10 to 20 % due to the signal noise, but this still leaves the engine under-powered. The loss of power is most likely due to the engine's condition.

Compressor outlet temperature

The thermocouple that measured the compressor outlet temperature, and its mounting, were exposed to radiation from the combustor outlet volute. The measurement was the most affected by thermal lag, and due to other test limitations it was not always possible to wait for the temperature to stabilise. These factors affected the calculation of the turbine inlet temperature, and the compressor and turbine efficiencies. Refer to Appendix C.4 for more information.

Exhaust gas temperature

The uncertainty in the average exhaust gas temperature (T_4) is partly due to the individual thermocouple accuracy. However, variation in temperature and the small number of measurements form a greater portion of the uncertainty. Refer to the uncertainty analysis in Appendix B.2. There were four equispaced points on the jet pipe for the measurement of the exhaust gas temperature, however, only three of these were used due to the PLC input limit.

Combustion efficiency

The combustion efficiency can be calculated from the theoretical and actual fuel flow-rates (Equation 2.2). The calculated rates assume complete combustion, and were intended to represent the theoretical flow-rates; while the measured flow-rate could be used for the actual value.

Combustion efficiencies are typically high, 98-99 % (Saravanamuttoo *et al.*, 2009); and thus require accurate measurement. However, the calculated flow-rate uncertainties were large (typically 20 %) because they were calculated from the exhaust gas temperatures (EGT), for which there were large uncertainties. As a result the calculated efficiencies were too inaccurate to be used in evaluating the combustor performance.

However, the combustion efficiencies for the no-load and on-load data in Table 6.2 are 96 % and 101 %, respectively. These values are more realistic than

expected given the large EGT uncertainty, and perhaps the EGT uncertainty is overly conservative.

Kinetic energy

The kinetic energy was assumed to be negligible. This assumption only affected the compressor outlet pressure, which was measured; and the exhaust pressure, which was equated to the ambient pressure. The compressor pressure was measured at the main air casing, where the flow area is large. Thus the difference between the stagnation and static pressure is negligible (less than 0.2 kPa), as shown in Table 5.2.

In a turboshaft engine, most of the kinetic energy of the exhaust gases is recovered by a diffuser located after the turbine (Saravanamuttoo *et al.*, 2009). Hence the exhaust stagnation pressure can be approximated by the ambient pressure ($v_4 \approx 0$). For example, the exhaust rate of kinetic energy for standard engine operation is 1.9 kW (from Table 5.2), or less than 0.5 % of the fuel heating rate ($\dot{Q}_{in}$ in Table 6.4).

Oil cooler fan

An oil cooler was connected to the gas turbine, and an unused blower fan was attached to the cooler. The fan was found to be underpowered for sustained engine testing. If prolonged tests are to be run, then it is recommended to upgrade the fan. Refer to Appendix C.5 for details and a recommended product.

High inlet air temperatures

The exhaust gases were not entirely exhausted through the exhaust duct, and a portion flowed back into the test cell. This resulted in elevated air inlet temperatures, and several tests were stopped when these temperatures reached a critical level (50 °C). A more detailed description and recommendations are discussed in Appendix C.6.

7. CFD Analysis

7.1   Introduction

The combustor was modelled in CFD to evaluate the effect of the fuel conversion on the flow pattern. The geometry was modelled in Autodesk Inventor, and the CFD simulation was configured and run using the Design Modeller, Meshing and Fluent software, which are part of the ANSYS Workbench suite.

The air and fuel flows were modelled for both the original liquid atomiser and the custom gas injector, without combustion. The two different models/simulations will be differentiated with the terms *kerosene* and *propane*, as these fuels were injected into flow domains with the atomiser and injector, respectively.

The intention was to simulate combustion, most likely with the finite-rate EDM (eddy dissipation model), and some of the model settings were selected in preparation. However, due to time constraints, no useful results were obtained.

7.2   Geometry

The Rover combustor components were geometrically modelled and assembled in CAD. The outer air casing (OAC), flame tube, igniter, shroud cap and injectors were modelled by taking measurements of the components. The CAD models of the main air casing (MAC) and volute that Homann (2015) obtained from a 3D imaging process were used, instead of trying to measure their complex surfaces.

A sectioned view of the combustor assembly with the original simplex atomiser and shroud cap is illustrated in Figure 7.1. The figure also illustrates the CFD flow domain, which was a half model, with the MAC and volute truncated just below the flame tube outlet.

Simplifications

Several simplification were made to the CAD models to aid the CFD simulation. The original MAC and volute models had of a lot narrow and complex surfaces, which resulted in poor mesh quality. To improve mesh quality, the geometry was re-modelled in CAD to approximate the original files. The resulting geometry was simpler, while remaining representative. The MAC

66
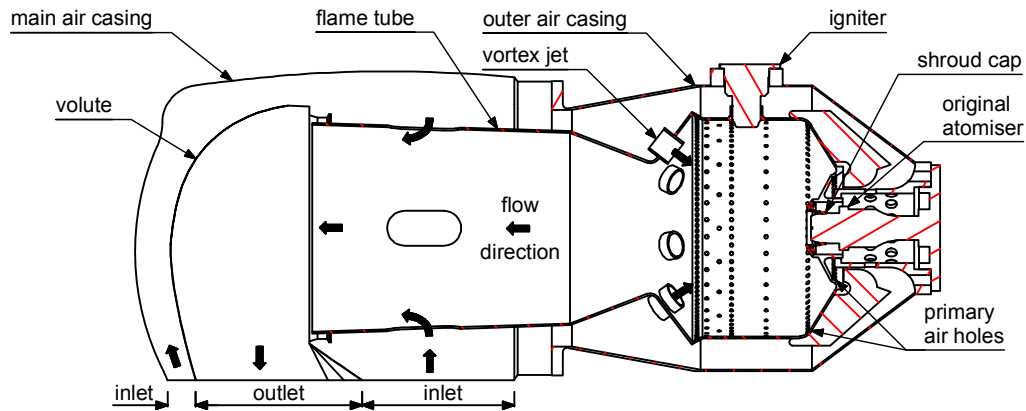
Figure 7.1: Combustor assembly, with original liquid atomiser and shroud cap

and volute geometry were not considered too critical, given their distance from the main area of interest; which was the flow within the flame tube.

The flame tube, volute, main air casing and the outer air casing have thin wall construction, and were represented by surfaces in the CFD simulation. The wall thicknesses were specified in Fluent, which were used for one-dimensional thermal conduction.

7.3   Mesh

The geometry was a mix of large voids and small features, and the most successful approach was to use unstructured mesh. The following non-default settings were used for both models.

Description	Setting	Description	Setting
Size function	curvature	Use uniform size function for sheets	no
Relevance centre	fine	Transition	slow
Span angle centre	fine	Min size	0.5 mm
Max face size	5 mm	Max tet size	10 mm
Growth rate	1.1	Automatic mesh based defeaturing	on
Defeature size	0.5 mm		

In addition, a uniform size function of 2 mm was applied to the flame tube interior of both models. A curvature size function of 0.5 mm was applied to the injector interior (fluid) of the propane model.

The kerosene domain was meshed with a patch conforming method applied to the atomiser region (surrounding fluid and porous zone of the OAC), which is recommended for clean geometry (Introduction to ANSYS Fluent, 2016). A uniform size function of 0.75 mm was also applied to the porous

zone of the OAC.

The Introduction to ANSYS Fluent (2016) recommend that the minimum orthogonality should be greater than 0.1, while a range of 0.15 to 0.20 is considered acceptable. The maximum aspect ratio should be less than 100. The resulting mesh had the following quality.

Description	Criteria	Kerosene	Propane
Cell count		2 498 512	2 675 040
Orthogonality, min (average)	> 0.1	0.16 (0.775)	0.12 (0.774)
Aspect ratio, max (average)	< 100	9.87 (1.82)	9.81 (1.82)

While most geometrical features were radially symmetric (about their central axis), it was impossible to sweep this geometry due to asymmetric features. If these had been defeatured, then a neater mesh may have have been possible. For example, the internal volume of the flame tube is defined by the revolution of a profile. However, there are several holes on the flame tube surface that prohibit the volume from being swept.

Initial simulations used porous jumps to represent the multitude of small holes on the flame tube. However, the resulting flow lacked the localised and jet nature that should be present. Consequently the holes were modelled in the final simulations.

7.4   CFD Model

A multi-species non-reacting simulation was run for the kerosene and propane geometries. The simulations were used to compare the flow patterns and flammable zones.

7.4.1   Settings

This section describes the final CFD configuration used in the simulations.

Solver settings

The realizable k-ε viscous model was used with enhanced wall treatment and the production limiter activated. All other settings were default. The species transport model was used monitor the flow and mixing of fuel vapour. The following simulation settings were common to both simulations.

Description	Setting	Description	Setting
Solver	pressure based		
Time	steady		
Pressure-velocity	coupled		
Discretisation		Physical models	
- gradient	least squares cell based	- energy	on
- pressure	PRESTO!	- viscosity	k-ε
- others	second order upwind	- species transport	on

Boundary settings common to both simulations

The simulation was run to match the engine specification for standard operating conditions. The engine analysis described in Section 5.1 was used to determine the fuel consumption and combustor inlet temperature (refer to the first row in Table 5.1 & 5.2).

A pressure inlet boundary was used for the *air inlet*, and a mass flow outlet was used for the combustor *outlet*. The mass flow-rate at the fuel inlet and combustor outlet were specified explicitly. The mass flow-rate at the air inlet was implied by the difference between the fuel and outlet flow-rates. This implied value was 0.3015 kg/s for both simulations.

The Fluent material library was used to defined the *material properties*. All of the solids and wall boundaries were specified as steel. All *wall boundary* conditions were specified as adiabatic, stationary, smooth, and non-slip. The following thicknesses were specified for walls represented as surfaces; 1 mm for the flame tube and volute, 1.1 mm for the OAC, and 1.5 mm for the MAC. Symmetrical boundaries were used for fluid surfaces on the plane of symmetry.

The predefined kerosene-air mixture was used for the kerosene simulation, and the propane-air-2step mixture was used for the propane simulation. The mixture density was specified as ideal gas, and the specific heat was calculated with the mixing law, which uses the specific heats of the gas species. The individual species' specific heats were calculated from temperature dependent polynomials, with default coefficients. The default values for the mixture thermal conductivity, viscosity, and mass diffusivity were used.

Kerosene boundary settings

The discrete phase model was used to model kerosene droplets in the combustor. The pressure dependent boiling, interaction with continuous phase, droplet coupled heat-mass solution, and linearise source terms options were used.

Table 7.1: Boundary conditions for the propane simulation

		Air inlet	Fuel inlet	Outlet
Mass flow-rate[1]	[kg/s]		4.89×10^{-3}	0.3064
Gauge total pressure [2]	[kPa]	0.1		
Supersonic/initial gauge pressure [2]	[kPa]	0.0	266.3	
Total temperature	[°C]	157.7	25	
Hydraulic diameter	[mm]	73.49	9.8	
Turbulent intensity		10 %	5 %	
Oxygen mass fraction		0.23		
Propane mass fraction			0.9999	

[1] Mass flow-rates are half the real values to account for the half-model.
[2] Gauge pressures are relative to the operating pressure of 283.6 kPa.

The pressure-swirl-atomiser model was used to inject liquid kerosene into the combustor. The cone angle of the Rover swirl atomiser was unknown, so an assumed half angle of 45° was specified at the point of the atomiser orifice. The measured orifice diameter of 1 mm, and the average fuel pressure of 3.0 MPa for the peak power jet fuel test data were used in the simulation. This test data was summarised in Table 6.3. The default atomiser dispersion angle, and the sheet and ligament constants were used, because these parameters were unknown for the Rover atomiser.

A kerosene flow-rate of 5.15×10^{-3} kg/s, and an outlet flow-rate of 0.3067 kg/s were used. Because a half-model was simulated, these values are half the real flow-rates. The same air inlet conditions were used for the kerosene and propane simulations, and are listed in Table 7.1.

Propane boundary settings

The only difference between the two simulations was the fuel and outlet flow-rates. A mass flow inlet boundary condition was applied upstream of the custom injector orifice. The boundary parameters are listed in Table 7.1. The air inlet flow-rate was not listed in the table, because, as discussed earlier, this value was implied.

The oxygen and propane mass fractions were specified at the inlets, and the nitrogen fraction was automatically set so that the sum of fractions would equal one.

7.4.2 Justification

This section covers the reasoning behind the CFD configuration (settings), most of which was based on information from the Fluent User's Guide (2017) and Introduction to ANSYS Fluent (2016). Refer to Appendix D for a summary of this information.

Solver

The *pressure based solver* was used as all of the combustion models are available with it, whereas only the volumetric models are available with the density based solver. A shock wave might occur downstream of the custom injector orifice, which may be better resolved with the density based solver, however, the shock was not of primary interest.

The *least squared cell based* spacial discretisation scheme was used, because it is as accurate as the Green-Gauss Node Based discretization (for irregular grids), but computationally faster (Fluent User's Guide, 2017).

Turbulence model

SST k-ω and Realizable k-ϵ are recommended for most internal flow simulation. The boundary layer can be modelled more accurately with the k-ω model, however, a finer mesh is required to realise the benefit (near-wall mesh with a y^+ of 1).

The k-ϵ turbulence model was used, as it is robust, suitable for internal flows, and it works with a coarser mesh (near-wall mesh with a y^+ between 30 and 500). Only the gross flow effects were of interest. The production limiter option was used as it can limit excessive generation of turbulence energy near stagnation points, which is typical of the standard two-equation turbulence models.

Material properties

The change in air density across the combustor was fairly small (about 4 %), which could justify the use of an incompressible gas model. However, due to the large change in propane pressure, it was necessary to account for compressibility. Air behaves as an ideal gas, with a compressibility factor close to 1 for the combustor temperatures and pressures. However, propane is less ideal, with a compressibility factor closer to 0.9 at the fuel inlet for the present case, but it will get closer to 1 as it enters the combustion chamber (Moran and Shapiro, 1998). The propane flow-rate might be inaccurate by a margin of 5 %, because it is proportional to the square root of density (see Equation 6.3).

About 99 % of air is made up of oxygen and nitrogen. On a mass basis, air contains approximately 76.7 % nitrogen and 23.3 % oxygen (Saravanamuttoo *et al.*, 2009).

Boundary conditions

The outlet pressure of the combustion chamber was unknown, but the air and fuel inlet pressures and mass flow-rates were known. Mass flow boundaries were used for the combustor outlet and fuel inlet to ensure that the flow-rates were correct. A pressure boundary was used for the air inlet.

A mass flow boundary does not allow reverse flow, while a pressure outlet does. Neither option accurately reflects the outlet flow. Recirculation on the outlet plane is possible due to the 90° bend and expansion in the volute. However, the downstream geometry, which was not included in the model, will prevent/reduce recirculation. The true flow might therefore be between the modelled flow for the two boundary types.

The flow in the combustion zone was the main interest (refer to Figure 2.2). The choice of outlet boundary was considered to have limited affect on the macroscopic flow behaviour in this region.

Discrete phase model

Liquid kerosene was modelled with the discrete phase model. The *interaction with the continuous phase* option was used because it couples the two phases, allowing momentum and energy to be transferred between the phases. Without this option the particles experience drag due to the gas flow, but the gas flow remains unaffected (i.e. no momentum exchange).

The particle heat and mass equations are solved separately with an implicit Euler integration by default. The *coupled heat-mass solution* solves the equations with an ordinary differential equation solver. This option increases the solution accuracy, but increases the computational time.

Particles will boil if their temperature reaches the boiling point defined for that material by default. In contrast, the *pressure dependent model* determines whether the particle should evaporate or boil based on its temperature and vapour pressure. This requires appropriate vapour pressure data for the range of temperatures and pressures of the simulation.

The source terms of the discrete phase momentum, energy and species can be linearised, with the *linearise source terms* option, to increase the numerical stability of steady flows.

7.5   Results

The most significant result was the difference between the flow patterns of the kerosene and propane simulations (Figure 7.2). Refer to Figure 7.1, and Figure A.2 (in the appendix) for the respective terminology used to describe the combustor hardware and propane injector.

The vortex jets created a strong toroidal vortex in the combustion zone of the kerosene model, as shown in Figure 7.2 (a). The primary air holes on the head of the flame tube contribute to the vortex, and result in a cool layer of air along the tube surface.
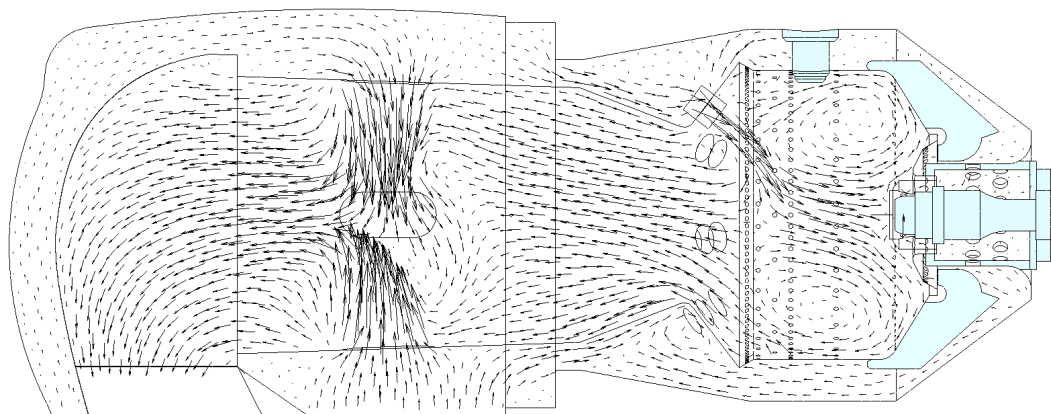
(a) original atomiser
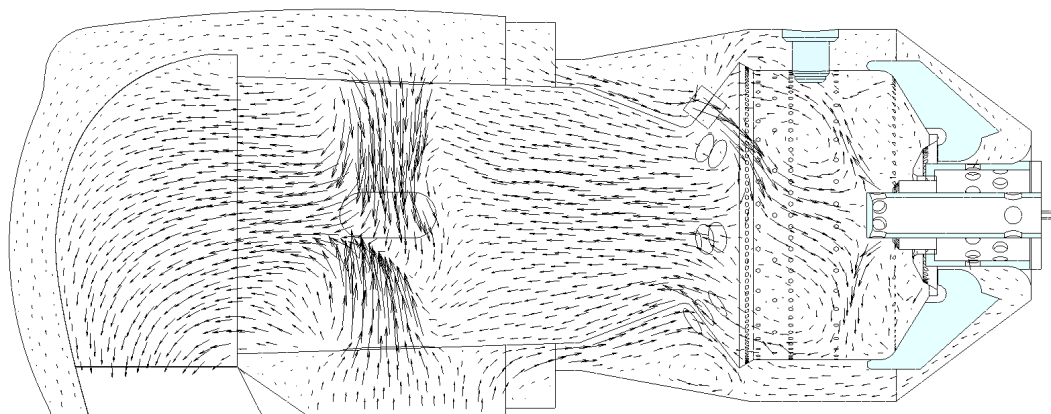
(b) custom injector

Figure 7.2: Combustor flow patterns on the plane of symmetry

The propane injector was designed to partially premix the propane with air, and to direct the mixture towards the igniter to facilitate ignition (Figure 7.2 (b)). This mixture flows through the point where the vortex centre occurred

in the kerosene model. The primary air holes might be less effective without the vortex circulating past them.

The kerosene spray was quickly swept into the air vortex, without noticeably affecting the air flow (Figure 7.3). The accuracy of its trajectory will depend on the accuracy of droplet momentum (size and velocity). The vortex carries the droplets along the flame tube perimeter, and then passed the igniter (important for ignition).
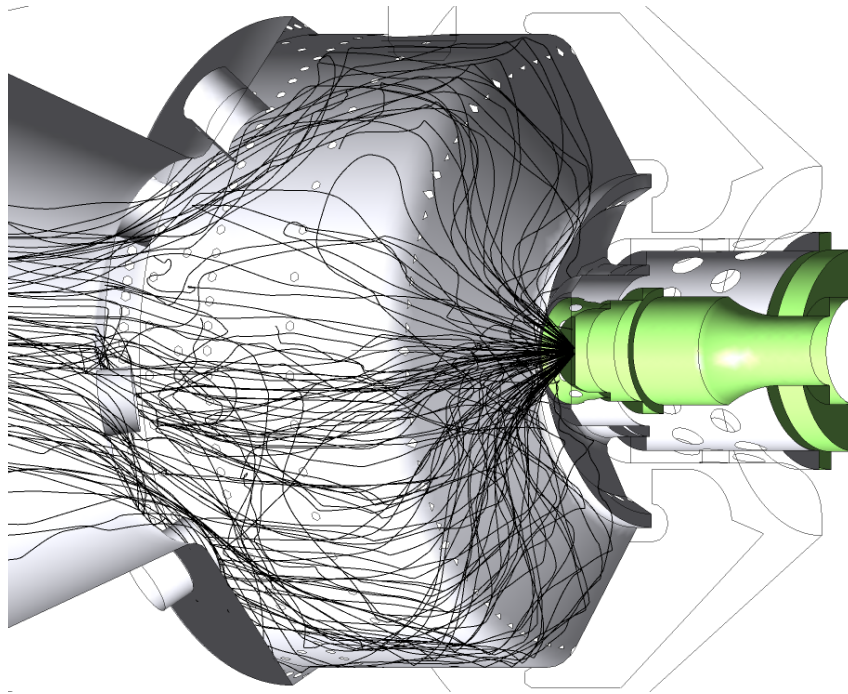
Figure 7.3: Kerosene spray swept backwards (to the right) by air vortex

Table 7.2 lists the kerosene droplet parameters at the atomiser and outlet plane. Most of the droplets evaporated by the outlet, which is indicated by the difference in flow-rate ($\dot{m}$) and mean diameter ($\overline{D}$). The sample standard deviation of velocity (S_v) and diameter (S_D), and the Sauter mean diameter (SMD) have also been tabulated. The SMD is the droplet diameter with the same volume-surface ratio as the entire spray (Lefebvre, 1983),

$$\text{SMD} = \frac{\sum nD^3}{\sum nD^2} \tag{7.1}$$

7.5.1   Validation

The engine testing did not provide data that could be used to validate the CFD models. However, the CFD work was a small part of the project,

Table 7.2: Kerosene droplet

	Atomiser					Outlet	
$\dot{m}_f$	v	S_v	$\overline{D}$	S_D	SMD	$\dot{m}_f$	$\overline{D}$
[kg/h]	[m/s]	[m/s]	[μm]	[μm]	[μm]	[kg/h]	[μm]
37.5	51.5	6.9	22	8	29	1.69	16

and models were only used to investigate changes in the flow due to the conversion. General CFD recommendations were followed, and the change in the gross flow is considered indicative of the actual flow. The detailed flow is probably inaccurate.

Versteeg and Malalasekera (2007) recommend that the near-wall mesh y^+ value stays greater than 11.63, and recommend values between 30 and 500, for accurate use of wall functions. This recommendation is applicable to the k-ϵ turbulence model.

This criteria was not met throughout the domain due to regions of low velocity and small features, which resulted in small y^+ values. The mesh was sized to capture small features, and the growth rate was kept small (1.1) to achieve the recommended orthogonality and aspect ratio.

The results were checked for mesh independence, as shown for the kerosene model in Table 7.3. The percentage of near-wall mesh that is compliant with the y^+ criteria has been included for different regions, where the remaining percentage was for $y^+ < 30$.

Table 7.3: Kerosene mesh independence

Mesh	Cell count	Δp [kPa]	$\dot{m}$ [kg/s]	$30 < y^+ < 500$[1]			
				All	Tube	OAC	MAC
Coarse	533 020	15.75	0.003 88	77 %	79 %	89 %	99 %
Medium	1 621 459	11.88	0.049 47	64 %	77 %	77 %	96 %
Fine	2 498 512	11.85	0.049 42	56 %	65 %	51 %	88 %

[1] Non-compliant mesh had $y^+ < 30$

The pressure difference between the air inlet and outlet (Δp), and the flow-rate through the cooling holes ($\dot{m}$) were used to check for independence. The fine and medium mesh results were similar, while the coarse mesh results differ significantly. The flow-rate for the coarse mesh was much smaller, because the cooling holes were only represented by a single cell. By comparison the fine mesh used about four cells. Despite being too coarse,

23 % of the y^+ values were below 30. The gross features/patterns of the air flow was similar for all these meshes.

The presented data in the results section was calculated with the fine mesh, and obtained from a converged solution. The residuals and monitored quantities were used to judge convergence. The Fluent User's Guide (2017) recommends that all globally scaled residuals decrease to 10^{-3}, except for the energy residual, which should reach 10^{-6}. It also states that there is no universal metric for judging convergence, and that a few quantities should be monitored and be seen to stabilise.

The globally scaled residuals were seen to reach the recommended values; and the temperature at the centre of the outlet, and the mass flow-rates were monitored for convergence. The temperature monitor was used for combustion simulations, however, it also worked for cold flow because the fuel and air inlet streams were at different temperatures.

The deviation from the input parameters, and the continuity errors were also used to check for convergence. These are listed in Table 7.4. The deviation is the difference between the specified values and the CFD result, as a percentage of the specified valves. The the fuel and outlet (exhaust gas) flow-rates ($\dot{m}_f$ & $\dot{m}_g$) were specified explicitly, whereas the air mass flow-rate ($\dot{m}_a$) results as the difference between the two.

The deviations were all very small, except for the kerosene fuel flow. This is most likely a result of the atomiser model, which randomises the velocities and droplet size. The propane fuel pressure (p_f) was not specified, but it was calculated to be 549.9 kPa and 505.4 kPa from the fuel flow analysis (Section 5.2) and CFD model, respectively. The former result is based on test data, and was measured about a metre upstream of the point used in the CFD model.

The continuity error (mass balance of the flow domain) was expressed as a fraction of the fuel and outlet flow-rates. The errors were considered to be a small fraction of the fuel and total flows.

Table 7.4: Deviation and continuity error of simulations

	Deviation from input				Continuity error	
Description	$\dot{m}_a$	$\dot{m}_f$	$\dot{m}_g$	p_f	$\Delta\dot{m}/\dot{m}_f$	$\Delta\dot{m}/\dot{m}_g$
Kerosene	0.06 %	1.3 %	-0.04 %		2.4 %	0.04 %
Propane	0.06 %	-0.03 %	0.07 %	-8.1 %	-0.8 %	-0.01 %

7.6 Discussion

The CFD models were not validated with test data. However, given validation that was possible, and the similarity of the kerosene and jet fuel models, a qualitative comparison was considered valid. Clearly the conversion has resulted in a change to the flow pattern, within the combustion zone of the flame tube.

The change may influence the exhaust gas temperature distribution, flame tube temperature, emissions, and flame stability. Combustion simulations could be useful in determining whether the flame tube temperature, or emissions changed significantly. However, combustor testing would probably be required to quantify the change.

The engine test data indicates that the exhaust gas temperature distribution was more uniform with propane than jet fuel. The difference in exhaust gas thermocouple readings (ΔT_4) was averaged for the stable data that was plotted in the Section 6.4 (engine test results). The propane average was lower than the jet fuel average (67 vs 120 °C). The same result can be seen in Table 6.3 and 6.4, which both compare propane and jet fuel tests.

The change in the flow pattern was not intended. Without any apparent benefit in changing the flow, it is recommended to change the gas injector such that the flow is more similar to that of the original atomiser. The volumetric flow-rate through the original atomiser (liquid fuel) was far less than the premixed flow through the gas injector. The flow-rate through the gas injector, and hence the change in combustor flow, could be reduced by changing the gas injector to a design that does not premix the air and fuel.

Alternatively, the gas injector nozzle could be modified to reverse the mixture flow, so that it matches the toroidal vortex observed with the original atomiser (Figure 7.2 (a)). The nozzle was designed to direct the fuel towards the igniter, at 60° to the combustor axis, to facilitate ignition. For example, this angle could be changed to 135° (i.e. redirect the flow to right most part of the flame tube in the illustration). As was seen with the kerosene flow path (Figure 7.3), it is possible for the fuel to reach the igniter by flowing along the flame tube surface, from the injector to the igniter.

The kerosene droplets were injected at 45° to the combustor axis, but rapidly changed direction due to the vortex flow. The accuracy of the flow depends on the atomiser model that was used. The Sauter mean diameter (SMD) was 29 µm, which is within the range of modern gas turbines (10 to 400 µm), according to Lefebvre (1983). While Saravanamuttoo *et al.* (2009) state that 50 to 100 µm is used in practice. The atomiser model was sensitive to the supply pressure, with the droplet diameter increased by an order of magnitude for a

change in supply pressure from 3 to 1 MPa.

The air pressure drop across the combustor was calculated to be 11.85 kPa (see Table 7.3), which is 4.2 % of the air inlet pressure (283.6 kPa). This value lies between the typical pressure loss fractions of industrial (2-3 %) and aeronautical (6-8 %) gas turbines given by Saravanamuttoo *et al.* (2009).

The CFD result could be used to update the assumed value (8 %) that was used in the engine analysis (Section 5.3). The actual pressure loss between the compressor and turbine should be slightly higher than the CFD result. Only a portion of the flow path between the compressor and turbine was modelled, but the pressure drop across the omitted regions will be small due to large flow areas compared to the combustor. Only cold flow was simulated, and the pressure loss will be higher with combustion. However, Saravanamuttoo *et al.* (2009) state that the pressure loss due to combustion is about 5 to 10 % of the cold flow pressure loss.

8. Conclusion

8.1 Overview

This project was intended to gain insight into gas turbine combustion, and to run a gas turbine on propane, with the ultimate goal to run it on biogas. The project was motivated by research into a combined gas and steam cycle that is powered by concentrated solar power, and hydrocarbon combustion. The ideal is to use biogas as fuel, as this will result in zero nett carbon emissions.

The project objectives were to determine a method to convert a gas turbine from liquid to gaseous fuel, and to run a Rover 1S/60 gas turbine on propane to match the results Zhang (2016) obtained with jet fuel. A conversion method was presented in Chapter 3 that should provide adequate guidance in the preliminary stages of a conversion. The conversion of modern gas turbines, which must conform to industry specific standards, will be far more complex than suggested by the method.

Zhang (2016) ran the Rover gas turbine on jet fuel, before converting the fuel supply system and running the engine on LPG at low speed. In this study, the Rover engine was successfully run on propane up to its top speed and under load. The engine performance with propane and jet fuel were successfully matched within the operational limits of the engine.

The project was considered a success within the project scope. An evaluation of the objectives, and recommendations for future work are presented in the following sections.

8.2 Conversion method applied to the Rover

In this section the conversion of the Rover gas turbine is summarised and evaluated against the conversion methodology presented in Chapter 3.

8.2.1 Fuel characteristics

It was necessary to consider the fuel characteristics in the conversion. The fuels considered in this project (jet fuel, LPG, propane, natural gas and biogas) have similar calorific values (refer to Table A.1), and the required mass flow-rates differed slightly.

The vapour pressures of propane and LPG are sufficient to achieve high velocity injection into the Rover combustor; the vapour pressures at 20 °C are more than double the combustor pressure. Propane was used instead of LPG because it has a higher vapour pressure at the same temperature. The difference in calorific values is negligible; less than 0.5 % (Afrox, 2016).

As distillates, LPG and propane are clean fuels, however, natural gas and biogas typically contain sulphur compounds. The sulphur will need to be removed before combustion to avoid creating air pollution, and to avoid corrosion in heat recovery equipment (if used).

8.2.2   Injection

The custom gas injector partially premixes fuel and air (i.e. a rich mixture) before the fuel enters the combustion zone. The liquid atomisers (simplex and air-assisted), which were originally supplied by Rover, did not premix air and fuel, and produced a diffusion flame.

The change to premixed injection might improve the quality of combustion, but could also reduce stability. The Rover engine ran well with the gas injector, and instability was not evident. Stability tests were however, not performed. Figure A.2, in the appendix, is an illustration of the gas injector.

8.2.3   Fuel control

The final fuel control system met all of the requirements, and most of the non-essential criteria specified in Section 4.2. The system was required to provide safe operation, a range of flow-rates, compatible operation with the test facility, and sufficient fuel to match the jet fuel results obtained by Zhang (2016). To match the jet fuel results, the fuel rate was increased from 11 kg/h of LPG (initial system) to 36 kg/h of propane (final system).

The system was suitable for engine testing, where the dynamometer controller varied the load to keep the engine speed below a specified limit. Manual throttle adjustment was used to adjust the engine speed while below the limit, and to adjust the power output while at the limit. The engine test software was used to monitor various engine parameters, and shut off the gas supply if any reading became critical. A propane detector, which was installed in the test cell, was also able shut off the gas supply. The solution was cost effective, and is suitable for natural or biogas, as per the non-essential criteria.

Recommendations

The final fuel control system is unsuitable for general applications, which have variable load (e.g. power generation). An automated controller, together with a proportional valve, would overcome this shortfall. It would also enable the torque to be varied manually during engine testing, which might avoid the speed measurement error (refer to Appendix C.3).

It might be possible to vary the fuel flow by rapidly opening and closing the solenoid valves with a controller, as was considered with LPG injectors (Appendix A.5.3). However, the solenoid valves were not designed for a high number of operations. Instead, it is recommended to use a proportional control valve, which would also be be able to handle changes in the supply pressure. Refer to Appendix C.2 for more information.

The propane cylinder pressures can be a limiting factor on cold days, or when the cylinders are low on fuel. A vaporiser should be considered if propane/LPG testing is to continue, and if test durations are to be prolonged. Refer to Appendix C.1.

8.2.4   Isolated combustor testing and modelling

The combustor was not tested in isolation, however, cold flow CFD models of the combustor were created for the simplex atomiser and the custom injector. The flow regime was seen to change substantially, given the higher volumetric flow-rate of the air-propane mixture through the custom injector, compared to the liquid kerosene (jet fuel) through the atomiser. The change was not intentional, and it might affect the flame tube cooling.

Recommendations

The injector nozzle splits the toroidal vortex, observed with the original atomiser, with the air-fuel mixture (refer to Figure 7.2). It is recommended to use a nozzle that will reverse the flow of the mixture such that it will join/enhance the toroidal vortex.

Combustion efficiency, emissions, flame tube and outlet temperatures could be measured more easily if the combustor was tested in isolation. These measurements would be useful in validating a CFD model. To determine the combustion efficiency from the temperature rise, a specialised temperature measurement probe would be required, as discussed in Section 2.3. The outlet temperature distribution can be measured with regular high temperature thermocouples, if the relative values are more important than the true temperatures. Accurate values will be more valuable for CFD validation.

8.2.5   Engine testing

Engine testing was used to validate the fuel conversion. The shaft power, fuel consumption, and the average and variation in the exhaust gas temperatures were used as performance indicators. The engine specifications, and test results that Zhang (2016) obtained with jet fuel were used as benchmarks for the conversion to propane.

Unfortunately Zhang (2016) was unable to obtain valid jet fuel flow-rates, thus it was not possible to compare the thermal or combustion efficiencies. Although the uncertainty in the combustion efficiency for propane was too large to be of use, as discussed Section 6.5.

There was a large uncertainty in the average exhaust gas temperatures (EGT), because a small number of thermocouples (3) were used to measure the exhaust gases, and the readings varied significantly. As a result the uncertainty in the combustion efficiency was also large. Isolated combustor tests would probably enable the most accurate measurement of combustion efficiency.

Recommendations

The power measurement was undervalued by about 15 % due to signal noise on the speed sensor. It is recommended to add a signal conditioner/filter, or to add a secondary speed sensor. Refer to Appendix C.3 for more information.

Future engine testing could be limited by high ambient temperatures, because a portion of exhaust gases vent into the test cell; or high oil temperatures, because of an undersized oil cooler fan. Refer to Appendix C.5 and C.6 for a detailed description and recommendations.

8.2.6   Emissions

Propane is a clean fuel, and combustion should be complete. The only emissions that could be significant are oxides of nitrogen (NO_x) and carbon dioxide (CO_2). If the engine is run on unrefined biogas, then sulphur oxides (SO_x) could be a problem, while nett CO_2 emissions would be zero.

NO_x emissions were not measured (not within the project scope), and, given the age of the technology employed in the Rover gas turbine, NO_x emissions were probably not considered in the design of Rover gas turbine. CFD combustion models could be used to determine the change NO_x with the conversion. However, tests would be required to validate the models.

8.3   Engine performance

The performance with propane was similar to that of jet fuel, although the peak power produced with jet fuel was higher (88% vs 77% of rated power). The peak power with jet fuel occurred at 39 190 RPM with an EGT of 686 °C. The peak power with propane occurred at 45 310 RPM with an EGT of 664 °C. The speed was closer to the design speed (46 000 RPM), and the EGT was lower, but it still exceeded the maximum intermittent EGT (610 °C).

The difference in speed is due to the different fuel hardware, and torque control. Zhang (2016) increased the power output by reducing the engine speed, because the jet fuel system had a governor, but no throttle. In this study, the dynamometer held the engine speed constant (torque mode), while the throttle was increased to produce more power.

It was not reasonable to pursue higher power output, while the EGT limit was being exceeded. In conclusion, the jet fuel results were successfully matched within the operational limits of the engine.

Recommendation

The Rover gas turbine underperformed with jet fuel and propane, when compared to the engine specifications. Several factors were considered (see the Validation heading in Section 6.5), and the cause is most likely related to the engine. An engine inspection and service is recommended.

A. General Information

A.1   Fluid properties

Table A.1 is a summary of the fluid properties used in calculations. The natural gas and jet fuel properties were taken from Staffell (2011), which referenced several sources, and listed the variations of these. According to ExxonMobil [s.a.], Jet A-1 has a minimum LHV (lower heating value) of 42.8 MJ/kg, and a density between 775 and 840 kg/m^3, which are in agreement with those in Staffell (2011).

Table A.1: Fluid properties

Variable	Units	Air	LPG	Propane	Natural gas	Jet A-1
M	kg/kmol	28.97	49.7	44.09	19.0	
R	kJ/kg-K	0.2870	0.167	0.1886	0.438	
ρ^1	kg/m^3	1.225	2.10	1.86	0.712	807 ± 7
$-\Delta h_{25}$	MJ/kg		45.8	46.0	45.86 ± 3.95	43.69 ± 0.51

1. Gas densities are at 15 °C & 1 atm, while Jet A-1 density is at 0 °C & 1 bar.

The LPG and propane properties were obtained from Afrox (2016), as these products were procured from Afrox, but it is worth noting that Staffell (2011) has a LHV of 46.28 ± 0.74 MJ/kg for LPG. The energy density of LPG will vary with the mixture ratio of propane and butane, but propane was assumed to have a similar variance.

A.2   Engine specifications

A.2.1   Performance

The following engine specifications were taken from the Maintenance Manual (1967), and are relevant for a Rover 1S/60 engine operating under standard conditions and running on an approved fuel. The fuel flow-rate appears to be in imperial gallons (when compared to the SFC).

- Max continuous power, $\dot{W} = 44.74$ kW (60 bhp)
- Pressure ratio, $p_r = 2.8$
- Air mass flow-rate, $\dot{m} = 0.603$ kg/s
- Max specific fuel consumption, $SFC = 0.852$ kg/kWh (0.635 kg/bhp h)

- Fuel flow-rate, $\dot{m}_f = 36.6$ to 42.0 kg/h (10.4 to 11.0 gal/h)
- Max continuous EGT, $T_4 = 580\,°C$

The standard operating conditions are defined as:

- Rated turbine speed, $n = 46\,000$ RPM
- Output shaft speed; **3000** (applicable to this study), 3600 or 8000 RPM
- Altitude, sea level
- Barometric pressure, $p_a = 101.3$ kPa
- Ambient air intake temperature, $T_a = 15\,°C$
- Air intake depression, $\Delta p_i = 0$
- Exhaust back pressure, $p_4 - p_a = 0.498$ kPa (50.8 mm H_2O)

One of the recommended fuel specifications is D.Eng.R.D.2494, which has been superseded by the DEF STAN 91-91 specification (Shell, 2003). This standard defines a Jet A-1, a kerosene fuel grade, which was assumed to be applicable to the above specifications. The fuel properties listed in Table A.1 were used to evaluate the performance curves and to determine the following:

- Specific power, $w = \dot{W}/\dot{m} = 74.20$ kJ/kg
- Fuel flow-rate, $\dot{m}_f = SFC \cdot \dot{W} = 38.1$ kg/h
- Combustion heat rate, $\dot{Q}_{in} = -\Delta h_{25} \cdot \dot{m}_f = 462.6$ kW
- Thermal efficiency, $\eta = \dot{W}/\dot{Q}_{in} = 9.67\,\%$

The Maintenance Manual (1967) states that the engine rating will diminish by 2.5 % for every 300 m increase in altitude (up to 4500 m). The rating will also diminish by 1 % for every 0.25 kPa increase in exhaust pressure or decrease in intake pressure. And an increase in power output is possible with an increase in humidity.

The Rover engines either used a simplex (swirl) or an air assisted atomiser. The engine used in this study originally used the simplex atomiser.

A.2.2 Operating conditions

The following information is taken from the engine test section in the Overhaul Manual (1972). The air intake operating limits are between -55 and 50 °C. The oil consumption should not exceed $57\,cm^3$/h, and the maximum temperature difference between the four exhaust thermocouples is 150 °C.

On start up, the starter motor relay can be opened once the main air casing pressure reaches 34.5 kPa (5 psi). Above these pressures the engine should be self powering. In this study, a corresponding engine speed of about

24 000 RPM was measured, while in practice the starter relay was opened just below 10 000 RPM.

No-load operation

Originally the Rover 1S/60 engine was governed under no-load conditions, and once the engine speed was stable the following parameters were specified (Overhaul Manual (1972)):

- Engine speed, 47 000 ± 500 RPM
- Oil pressure, 124 kPa (18 psi); minimum pressure, 48.3 kPa (7 psi)
- Bearing seal pressure, 16.9 to 27 kPa (5 to 8" Hg)

After the exhaust gas temperature has stabilised the following conditions apply:

- Engine speed, 47 000 ± 300 RPM
- Exhaust gas temperature, below 400 °C
- Oil temperature, below 110 °C
- Compressor delivery pressure, 179.3 to 214 kPa (26 to 31 psi)

On-load tests

The no-load conditions are also applicable for a load with a corresponding exhaust gas temperature (EGT) of 560 °C, except for the following differences:

- Engine speed, 46 000 ± 500 RPM
- Oil pressure, 110 to 124 kPa (16 to 18 psi); minimum pressure, 48.3 kPa (7 psi)

The same conditions still apply for a further increase in load such that the EGT is 600 °C, and the compressor pressure should not drop with the increased load. The maximum continuous EGT is 580 °C, while the maximum intermittent EGT is 610 °C. The intermittent rating is permissible for periods of up to 2 hours for 24 hours of consecutive running. However, this operation is regarded as an overload on the engine.

A.3   Original fuel control system - liquid fuel

The original fuel system as supplied by the engine manufacturer is described herewith. The information was taken from the Maintenance Manual (1967) and Overhaul Manual (1972). The system was not used in this research, but the data obtained by Zhang (2016) was used to analyse the engine, and as comparison to the test results (Section 5.3 & 6.4).

The original fuel system provided continuous fuel injection into the combustion chamber. Rover engines either used a simplex (swirl) or an air assisted atomiser. The fuel system regulated the fuel pressure to limit the top speed, exhaust gas temperature (EGT), and fuel flow during the acceleration period. Zhang (2016) used the original simplex atomiser when running the engine on jet fuel.

The fuel pump was driven by the compressor shaft, and thus the pump flow-rate was dependent on the engine speed. A governor incorporated in the fuel pump, opened a bleed valve as the engine reached its *top speed* (47 000 ± 500 RPM). As load is applied to the engine, the engine speed drops, which partially shuts the bleed valve, resulting in increased fuel injection. The peak power rating was specified at a *design* or *rated speed* of 46 000 ± 500 RPM, at which point the bleed valve is totally shut (i.e. maximum fuel supply).

A temperature control unit limited the EGT. A mercury bulb was located in the exhaust, and the resulting vapour pressure would cause a Bourdon tube to actuate a bleed valve. A pressure relief valve limited the fuel pressure as the engine got up to speed on start-up. Once at speed, the relief valve would be isolated either with a solenoid valve, or an alternate design used the compressor pressure to shut the relief valve (which would only occur once the engine speed was sufficiently high).

Some engine variants were fitted with a variable speed valve and/or a speed trim valve. The variable speed valve could be used to reduce the on-load engine speed by 16 000 RPM (i.e. on-load speed range of 30 000 to 46 000 RPM). The on-load speed is listed on the master build card for each engine (factory test results). However, the cards for the engine used in this study have been lost. The speed trim valve allowed adjustment of the no-load speed between the governed and full load speed.

The test engine was not supplied with the variable speed or speed trim options. So Zhang (2016) and/or Luiten (2015) added a needle valve to the fuel line, but the valve failed to throttle the fuel. Thus the jet fuel tests were effectively done with the OEM (original equipment manufacturer) system.

Electric start engines would automatically shut-off the fuel supply if the oil pressure was inadequate. The electrical controls were replaced by a PLC and software interface for engine testing (see Section 6.1), which were configured to shut off the fuel supply if any engine reading became critical. For example, insufficient oil pressure or high oil temperature.

A.4 Initial system - LPG

The initial fuel system was developed and used by Zhang (2016) to run the engine on LPG. It was also used at the start of this study to run the engine on LPG. LPG was supplied to the engine from a 9 kg LPG cylinder, and was manually controlled. Downstream from the cylinder were a quick release valve; a needle valve; a ball valve; and the custom injector, which was mounted onto the combustion chamber.
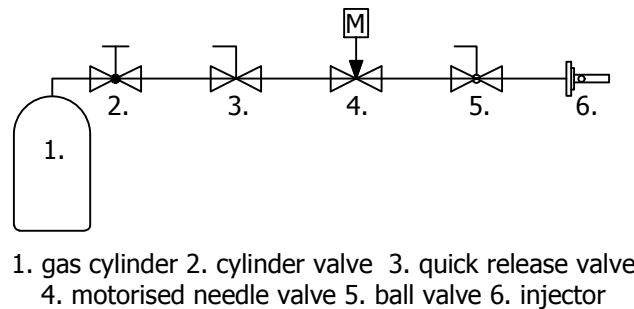

1. gas cylinder 2. cylinder valve 3. quick release valve
4. motorised needle valve 5. ball valve 6. injector

Figure A.1: Initial fuel system

The quick release valve had to be opened by hand from inside the test cell (engine room), but could be shut off from the control room. The needle valve was remotely actuated by an electric motor. A boat throttle actuator was connected to the ball valve, which, effectively, was either open or closed. The gas cylinder was located and operated in the control room during testing.

The *custom gas injector* was manufactured for gas injection, and had a similar design to a Bunsen burner (Figure A.2); a gas port at its base, followed by a 2 mm orifice to create a jet of gas down the length of a tube. Air was drawn through cross-holes at the base of the tube. A nozzle was threaded into the end of the tube to direct flow outwards.

A.5 Final system - propane

The final system is described in the body of the report (Section 4.3). This section covers some of the control options and factors that were considered, and the decisions made in improving the fuel control system. Table A.2 contains a list of the products used in the system.
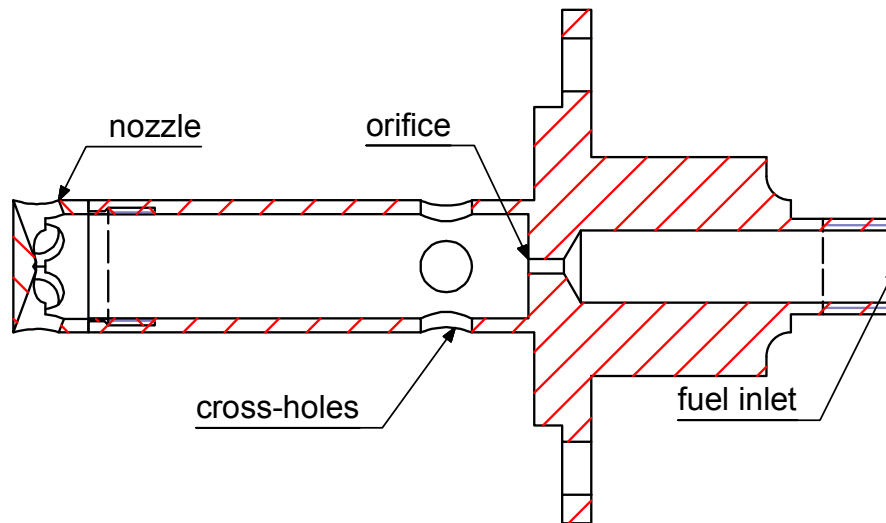
Figure A.2: Custom gas injector

Table A.2: Product detail

Device	WP [bar][1]	Reference size	Product
Regulator[2]	3.1 - 8.6	½" NPT ports	Rego 1584VH
Master valve[3]	0.20 - 16	13 mm restriction	bürkert 6281-EV-A13
Control valve	30	3.2 mm restriction	OMB Star 6 mm
Needle valve	345	¼" NPT ports	Parker N400S
Supply line	40	15 & 22 mm OD	Copper tubes, SANS460[4]
Control lines	35	8 mm OD	Copper tubes, EN1057
Quick release valve		¼ & ½" NPT ports	Unknown
Other valves		½" NPT ports	Various

[1] WP - working pressure.
[2] Regulator inlet pressure limit unknown; outlet pressure range listed above.
[3] Solenoid requires a minimum pressure to seal.
[4] Tubing conforms to class 1 or better, as required by SANS10087.

A.5.1 Fuel supply

Zhang (2016) ordered two 48 kg propane cylinders, and arranged the installation of an outdoor enclosure and gas line for the cylinders, but did not have the time to use them. The propane cylinders were used in this study because of the increased capacity and vapour pressure (compared to the 9 kg LPG cylinder), and because of the additional benefit of removing the fuel from the control room.

Another benefit of using propane over LPG is that there is less uncertainty

with vapour composition. LPG is stored as a liquid under pressure, with LPG vapour filling the space in the storage tank that is not filled with liquid. LPG vapour is normally drawn from storage tanks (unless a vaporiser is used), and the remaining liquid evaporates to replace the consumed vapour.

Handigas (LPG product from Afrox (2016)) consists of at least 60 % propane (by mass), at most 40 % butane, and up to 2 % of other hydrocarbons. The mass fraction of liquid propane was calculated to be 58 % from the vapour pressures at 20 °C (Afrox, 2016), with Dalton's law of partial pressures and Raoult's law (Brown *et al.*, 2003). This value is close to the claimed mass fraction of propane (60 %).

However, a propane vapour fraction of 82 % was calculated for the same temperature. The propane concentration is expected to drop as the fuel is consumed, because of the higher concentration of propane in the vapour than the liquid. However, no reference to this was found in the literature.

Pressure regulation

The initial system drew LPG vapour from the 9 kg cylinder, which displayed a gradual drop in cylinder temperature and pressure due to the evaporation. Thus the engine would gradually slow down as well. The pressure decline was retarded by partially submerging the cylinder in warm water.

The LPG flow-rate was 10 kg/h from a 9 kg cylinder, where a propane flow-rate of 36 kg/h was required from 96 kg (see Section 5.3.2). However, as the cylinder levels drop, the thermal capacity drops and the evaporative cooling becomes more significant. Afrox (2016) recommend a maximum consumption rate of 1 kg/h for a 48 kg bottle. This recommendation is for continuous consumption, and as was found with the 9 kg bottle, short tests can be performed on much less. Tests could also be prolonged by placing cylinders in water.

This problem can be avoided by using a *vaporiser*. A suitable vaporiser was found, but it was considered too expensive because the propane system was a temporary arrangement before running the engine on biogas. Refer to Appendix C.1 for more information, including the product details.

It was decided to use a regulator to operate below the vapour pressure. Thereby reducing the affect of vapour pressure variation with ambient temperature and consumption rate, and avoiding condensation within the fuel line. An absolute pressure of 600 kPa was selected, which has a corresponding saturation temperature of less than 8 °C. Ambient temperatures of less than 8 °C are uncommon in Stellenbosch (Stellenbosch University, [s.a.]).

Autogas systems are designed to convert piston engines to run on LPG or natural gas. Autogas hardware was appealing as it was suitable for propane, readily available and reasonably priced. Autogas *reducers* (pressure regulators) reduce the tank pressure (vapour pressure in the case of LPG) to the injector working pressure for indirect injection. LPG reducers are supplied with liquid LPG and include vaporisers to ensure sufficient injector pressure, and hence they are also called vaporisers. They use engine coolant to vaporise the LPG.

In the case of CNG, where the fuel can be stored up to 20 MPa, it is also necessary to use engine coolant to heat the fuel in the reducer, as the large pressure reduction would otherwise cause subzero temperatures, potentially leading to ice formation on the outside of the reducer and downstream gas line.

Most auto gas reducer outputs were limited to 250 kPa. Two CNG reducers were found with outputs up to 1000 kPa, unfortunately, one product had been discontinued by the manufacturer, and no distributor was found for the other. It was unclear whether it would be suitable for propane, especially given the low tank pressure of propane (relative to CNG). One product was said to have stable outlet pressure for an inlet pressure range of 1.5 to 24.8 MPa, but that range is still well above the vapour pressure of propane; 0.71 MPa at 20 °C (Afrox, 2016).

Emergency shut-off

The external propane line had an emergency shut-off valve on the exterior of the building, but it lacked remote control. The quick release valve that was used in the LPG system (Appendix A.4) was relocated just below the point where the external line entered the test cell. It could be shut from the control room, but still required manual actuation, and was at risk of damage in the event of fire or engine failure.

To address these limitations, a *master valve* (normally closed solenoid valve) was installed in the outside section of the supply line. It was thus located away from the test cell hazards, and could be actuated from the control room. A gas detector was also installed in the room, which would shut the valve in the case of gas detection. The engine testing software would shut the valve in the case of any sensor reading exceeding a specified limit.

A.5.2 Fuel injection

The custom gas injector that was used for LPG was also used for propane. Zhang (2016) intentionally undersized the injector orifice to limit the fuel supply so that initial tests could be conducted safely. In the current study,

the flow-rate was increased by increasing the line pressure and increasing the orifice size. The initial injector orifice was 2 mm in diameter, and the final size was 3.2 mm (refer to Section 5.3.3).

Injector pressure

The custom gas injector was sized to choke the flow. Under this condition, the flow rate is linearly dependent on the supply pressure, and independent of the combustor pressure. The flow becomes choked when the pressure downstream of a restriction has been reduced such that the fluid velocity through the restriction has become sonic. The flow-rate will not increase with further reduction in downstream pressure, as the change in pressure cannot propagate faster than the speed of sound.

Propane will choke at the narrowest flow section for a stagnation to static pressure ratio of 1.73 (refer to Section 5.2). An upper combustor pressure of 280 kPa (absolute) was expected, because the Rover engine has a 2.8 pressure ratio. The stagnation pressure upstream of the custom injector would need to be at least 484 kPa to achieve a choked condition. A high speed jet was considered beneficial as it would aid mixing and entrain more air through the pre-mix holes.

A higher pressure would allow a smaller orifice, for the same flow-rate. If the pressure for the maximum required flow was sufficiently high, then at lower flow-rates, the reduced pressure might still be high enough for sonic flow. The drop in combustor pressure (and engine speed) with reduced fuel flow, would extend the flow range at which the flow was choked. The upper limit of the pressure would be restricted by the propane vapour pressure, and the valve and supply line pressure ratings.

Fuel flow-rate

Early tests with the initial LPG system found that the engine speed could be reduced to about 10 000 RPM, with an LPG flow-rate of about 7 kg/h. The speed was stable, without any ill effects being noted, and was about the speed the engine would reach with the starter motor. It was decided to have a pilot flow-rate of around 7 kg/h.

The intention was to momentarily run the engine at idle with the pilot flow-rate. Once stable ignition had been achieved, then the flow-rate would be gradually increased to the top speed (requiring about 23 kg/h). To achieve the rated power, 35.3 kg/h was estimated as necessary (see Section 5.3.2).

A.5.3   Throttle options

Different throttle mechanisms were considered. Metering valves refer to valves that are good for gradual changes in flow-rate, such as needle and globe valves. Valves either require manual actuation, otherwise valve actuators allow for remote actuation. Actuators can be electrically, pneumatically or hydraulically operated.

Proportional valves are metering valves with automated control, and can be used to regulate flow or pressure under varying conditions. A controller will regulate the valve's position to match the input signal to the output (flow or pressure). Typical proportional control valves consist of spool valves actuated by either force or stroke-controlled solenoids. However, proportional valves might also refer to other valve types (e.g. a globe valve) that achieve the same behaviour. A proportional valve was not used due to price, but might be beneficial for future work, as discussed in Appendix C.2.

Gas turbine throttle mechanisms for gaseous fuels were sought, as presumably they would suit the application well. However, limited success resulted from such searches as the throttles were often too large for the current application, as presumably they catered for large industrial gas turbines.

The initial system used an electric motor coupled to a needle valve. The coupling was prone to slip if the valve was fully opened or closed, and it was difficult to judge the valve position from the control room. The coupling often slipped before completely shutting the valve, and it took several seconds to move from a fully open to closed position. So this mechanism required a secondary valve for rapid and complete closure of the fuel supply.

Autogas injectors are able to be opened and shut rapidly, and can meter flow by adjusting the ratio of time spent opened to that spent closed, similar to DC voltage regulation with pulse width modulation (PWM). Fuel could be injected into a manifold, which would function as an accumulator, and the supply pressure to the custom injector should appear steady. Multiple injectors would be required to supply sufficient flow.

Most autogas injectors are used for indirect injection of LPG or CNG, with a typical working pressure of 250 kPa, which is too low for this application. A CNG injector was found that was rated up to 1000 kPa. Unfortunately, the injector duty cycle was unknown, and it would be necessary to keep it open during full load operation. This is unlike the intermittent injection used in a piston engine.

Indirect LPG injection has successfully been used on diesel engines, where about 20% diesel is injected for ignition. There are a few direct injection

systems for petrol engines that inject liquid LPG. They use the existing petrol injectors, and the existing petrol system can remain, allowing the engine to be run on petrol or LPG (a dual fuel system). One of the benefits of direct (liquid) injection is that the engine can be started cold on LPG, as vaporisation is not required. Some of the difficulties are the potential of vapour locks on a hot start, and accounting for the density variation of LPG, which is far greater than petrol or diesel (Ariztegui *et al.*, 2015).

Some research is being done into direct CNG injection (Abdullah *et al.*, 2017), which may hold more promise for general gas turbine conversions, as they would require operating at higher pressures, and hence may be able to accommodate a wider range of gas turbines, which generally have much higher combustor pressures than the Rover engine.

A.5.4   Throttle decisions

Manual or automatic control

It was decided to use a manual throttle as the dynamometer controller was capable of torque control - where a speed set-point is entered and the controller adjusts the brake load to achieve that speed. Below this speed, no load is applied to the engine, the speed is manually controlled. The test software (ETA) was configured to shut the master valve in the event of any measured parameter exceeding its limit (e.g. engine speed or power).

Throttle mechanism

The selected throttle mechanism was a parallel network of four solenoid valves, each with a flow limiting orifice. One of the valves was earmarked as a pilot valve to provide 7 kg/h. Three other valves were used with equal orifice diameters, such that when all the valves were open, the total flow should allow the engine to match the Rover specifications.

The motorised needle valve from the initial system was used for gradual throttle changes. The pilot flow rate was guaranteed by bypassing the needle valve. The intention was to start the engine with the pilot valve, and then open some of the other solenoids, followed by the needle valve. The change to propane, and changes to injector or valve orifice sizes, were tested gradually by opening a limited number of solenoid valves, and then opening the needle valve.

This arrangement was insufficient to meet the target flow-rate, but this was addressed in the final system (refer to Section 5.3.3). The final system, which is described in Section 4.3, was very similar to this arrangement, but the needle valve was not used as it was no longer seen as necessary.

B. Engine Testing and Data Analysis

B.1   Dynamometer and PLC products

Table B.1 lists the product descriptions of the dynamometer and PLC (programmable logic controller) that were used to test the Rover gas turbine.

Table B.1: Dynamometer and PLC product descriptions

Item	Product
Dynamometer	Schenck W130
Dyno controller	Schenck LSG2000
Dyno power supply	Schenck LEW2000
PLC	MicroLogix 1200 series 1762-L40AWA
PLC modules (MicroLogix)	Analogue input 1762-IF4
	Thermocouple input 1762-IT4
	Analogue output 1762-OF4
	DC input 1762-IQ16

B.2   Uncertainty analysis

This section describes how uncertainties of measured and calculated parameters were quantified. The following information was taken from Coleman and Steele (1999).

The distribution of an infinite number of readings is defined as the parent population or distribution. If the variation in the readings is due to many small errors, that are as likely to be greater or less than the true value, then the readings will have a Gaussian or normal distribution. The distribution mean and standard deviation are respectively defined as,

$$\mu = \lim_{N \to \infty} \frac{1}{N} \sum_{i=1}^{N} X_i \qquad\qquad \sigma = \lim_{N \to \infty} \sqrt{\frac{1}{N} \sum_{i=1}^{N} (X_i - \mu)^2} \qquad (\text{B.1})$$

For a finite number of measurements, the sample mean and sample standard deviation are defined as,

$$\overline{X} = \frac{1}{N} \sum_{i=1}^{N} X_i \qquad\qquad S_X = \sqrt{\frac{1}{N-1} \sum_{i=1}^{N} (X_i - \overline{X})^2} \qquad (B.2)$$

For brevity, these are simply referred to as the mean and standard deviation. The probability (C) of a measurement being within t standard deviations of the population mean can be expressed as,

$$C = \text{Prob}(\mu - tS_X \leq X_i \leq \mu + tS_X) = \text{Prob}\left(-t \leq \frac{X_i - \mu}{S_X} \leq t\right) \quad (B.3)$$

which is referred to as confidence intervals. The term $(X_i - \mu)/S_X$ follows a t-distribution, where the value t depends on the degree of freedom ($\nu = N - 1$) and the level of confidence (C). The following expression is for the normalised sample mean distribution about the population mean,

$$C = \text{Prob}\left(-t \leq \frac{\overline{X} - \mu}{S_X/\sqrt{N}} \leq t\right) \qquad (B.4)$$

The inaccuracy, or total error (δ_i), of a measured parameter is the difference between the measured and true value ($\delta_i = X_i - X_{true}$). The error will include a systematic error (β), or bias, that remains constant with multiple readings. And a random component (ε_i), or precision error, that varies with each measurement (Coleman and Steele, 1999, pp6),

$$\delta_i = \beta + \varepsilon_i \qquad (B.5)$$

The confidence interval can be used to estimate the random uncertainty of either a single measurement or sample mean,

$$P_X = tS_X \qquad\qquad P_{\bar{X}} = tS_X/\sqrt{N} \qquad (B.6)$$

The bias uncertainty (B) can be estimated with a confidence interval by assuming that the bias also has a normal distribution (e.g. selecting a sensor from a large population with varied accuracy). This implies that the bias error will be less than the bias uncertainty ($|\beta| \leq B$), with a probability C.

The overall uncertainty is calculated from the bias and random uncertainties,

$$U_X = \sqrt{B^2 + P_X^2} \qquad (B.7)$$

which is used to define a confidence interval for the true value

$$C = \text{Prob}\left(X - U_X \leq X_{true} \leq X_i + U_X\right) \qquad (B.8)$$

Most engineering experiments have degrees of freedom large enough to justify a constant t value for a confidence level. For a 95 % confidence level and a degree of freedom greater than 9, $t \approx 2$ (Coleman and Steele, 1999, pp41). If a calculated parameter f depends on J variables,

$$f = f(X_1, X_2, ..., X_J) \tag{B.9}$$

then the uncertainty in f can be calculated from,

$$U_f^2 = \left(\frac{\partial f}{\partial X_1}^2\right) U_{X1}^2 + \left(\frac{\partial f}{\partial X_2}^2\right) U_{X2}^2 + ... + \left(\frac{\partial f}{\partial X_J}^2\right) U_{XJ}^2 \tag{B.10}$$

where the absolute uncertainties U_{Xi} should have the same level of confidence. If the function f takes the following form,

$$f = k \prod_{i=1}^{J} X_i^{a_i} \tag{B.11}$$

then becomes easier to solve for U_f from the relative uncertainties,

$$\left(\frac{U_f}{f}\right)^2 = \sum_{i=1}^{J} a_i^2 \left(\frac{U_{Xi}}{X_i}\right)^2 \tag{B.12}$$

The uncertainty analysis presented here was used in the calibration process, which is discussed in the next section, and Equations B.12 and B.10 were used to evaluate the uncertainty of calculated parameters in the test data analysis (Section 6.3).

Exhaust gas temperature

The exhaust gas temperature deserves a special mention, because the uncertainty was determined in a unique way. The exhaust gas temperature (EGT) will be represented by T (i.e. without the usual subscript). Three thermocouples were used to measure the EGT. The mean and standard deviation ($\overline{T}$ & S_T) were calculated with Equations B.2.

Equation B.6 was used to determine the random uncertainty of the average EGT. This implies that the temperature follows a normal distribution. The thermocouple uncertainty (U_T) was taken to be the bias. Equation B.7 was used to find the overall uncertainty,

$$U_{\overline{T}} = \sqrt{B^2 + P_{\overline{T}}^2} = \sqrt{U_T^2 + \left(tS_T/\sqrt{N}\right)^2} \tag{B.13}$$

The standard deviation was typically large, due to the temperature distribution at the turbine outlet. Thus the overall uncertainty was typically large.

B.3   Calibration

Table B.2 is a list of the sensor, calibration and test data ranges. Variable and product descriptions can be found in Table 6.1. Specifications for the shaft encoder and fuel differential pressure gauge could not be found. The torque sensor was a load cell with a load rating of 200 kg on a moment arm of 293 mm, hence the tabulated sensor range of 0 to 575 N m. However, the dynamometer was limited to 400 N m and 10 000 RPM.

The calibration ranges were selected on expected and historical ranges, and were mostly greater than the tested data. Exceptions were the dynamometer shaft speed, fuel differential sensor, and the exhaust and fuel thermocouples. The test data ranges represent all of the captured data, however, the data of interest mostly fell within calibration ranges. This is covered in more detail in the sensor specific subsections below.

Table B.2: Sensor, calibration and test data ranges

Property	Units	Sensor	Calibration	Test data	Comment
n	RPM	unknown	0 ... 2992	0 ... 3684	
τ	N m	0 ... 575	0 ... 201	0 ... 120	
Δp_a	kPa	0 ... 5	0 ... 4.7	0 ... 3.6	
p_{2x}	kPa	0 ... 250	0 ... 200	0 ... 61	
p_2	kPa	0 ... 400	0 ... 354	0 ... 256	
p_f	MPa	0 ... 6	n/a	0 ... 6.0	jet fuel data
			0 ... 4	0 ... 0.8	propane data
Δp_f	kPa	unknown	0 ... 4.7	0 ... 20.6	differential pressure
	MPa	20	n/a	0 ... 0.8	max working pressure
p_{oil}	kPa	0 ... 600	0 ... 500	0 ... 413	
T_1	°C	-40 ... 1000	-2 ... 121	-1 ... 64	
T_2	°C	-40 ... 1000	0 ... 350	-1 ... 297	
T_4	°C	-40 ... 1000	16 ... 650	-1 ... 927	
T_{oil}	°C	-40 ... 1000	-1 ... 121	-1 ... 107	
T_f	°C	-40 ... 750	-2 ... 121	-23 ... 50	
T_d	°C	-40 ... 750	-2 ... 121		
$\dot{m}_f$	kg/h	n/a	0 ... 40.4	0 ... 39.3	

Sensors were calibrated with a reference device. The rated accuracies of the sensors and the reference devices are listed in Table B.3. Where a device accuracy was specified as a percentage of the measured value, the greatest uncertainty for the calibration range was listed. For example, the thermocouples had uncertainties of at least ±1.5 °C or ±0.4 %, so the uncertainty of T_4

was $\pm2.6\,°C$ for a calibration range up to $650\,°C$. One exception is the fuel pressure sensor uncertainty, which is only valid for a range up to 1 MPa as the calibration range was much larger the propane data.

The rated accuracies were assumed to be the overall measurement uncertainties for a 95 % confidence. The regression column contains twice the standard estimate error for a linear regression of the calibration data, which was used to estimate of the random uncertainty ($P_X = 2S_X$). The standard estimate error is the standard deviation of the error between the measured and predicted values of the linear regression. It would also include the nonlinearity error of the sensor, although this could be compensated by using linear interpolation rather than linear regression with the data acquisition software (ETA).

The overall uncertainty is the combination of the sensor or regression uncertainty (which ever was greater), and the reference device uncertainty. The reasoning for this was that the calibration process did not test for hysteresis, repeatability or temperature sensitivity, while the sensor ratings generally included these factors and were often greater than the regression uncertainty. One exception was T_2.

The uncertainties were combined by taking the square root of the sum of squares. This similar to Equation B.7, except that instead of quantifying the bias and random uncertainties separately, both the reference and sensor (or regression) ratings were overall values.

Shaft encoder   The dynamometer shaft speed, n, was calibrated with an RM-1501 tachometer, with an accuracy of 0.04% $\pm$ 2 dgts $\pm$ 0.06 RPM and a 5 digit display. For a calibration range up to 2992 RPM this equates to an accuracy within $\pm1.5\,$RPM. It was difficult to calibrate the speed sensor while running the engine, and monitoring the inlet and exhaust temperatures. So the calibration was only run up to 2992 RPM, which is just short 3000 RPM (or the rated on-load engine speed of $46\,000\,$RPM).

Load cell   The dynamometer torque, τ, was calibrated by suspending weights on the calibration levers that are mounted to the dynamometer housing. The load cell was directly calibrated as a torque measurement. The reading was initially zeroed before adding the calibration levers and weights. Once the levers and weight trays were mounted to the dynamometer, they were balanced such that the reading was again zero. Thereafter weights were added to the weight tray, resulting in a known torque.

$$\tau = mgr \tag{B.14}$$

Table B.3: Sensor, reference device and calibration uncertainties for the calibration range

Property	Units	Sensor	Reference	Regression	Overall
n	RPM	unknown	1.2	8.1	8.2
τ	N m	1.4	0.39	1.0	1.5
Δp_a	Pa	48	2.0	6.7	48
p_{2x}	kPa	4	7	0.44	8.1
p_2	kPa	7	7	1.9	9.9
p_f	kPa	20 [1]	7	4.3	21
Δp_f	Pa	unknown	2.0	3.5	4.4
p_{oil}	kPa	10	7.0	1.2	12.2
T_1	°C	1.5	0.1	1.1	1.5
T_2	°C	1.5	5	8.8	5.2
T_4	°C	2.6	5	2.6	5.6
T_{oil}	°C	1.5	0.1	1.8	1.8
T_f	°C	1.5	0.1	0.95	1.5
T_d	°C	1.5	0.1	0.99	1.5
$\dot{m}_f$[2]	kg/h	n/a	0.89	0.11	0.90

[1] Uncertainty only applicable for a range of 0 to 1 MPa.
[2] Values are based on propane.

where m is the mass, g gravitational acceleration, and r the moment arm of the calibration lever about the dynamometer's centre. Equation B.12 was used to determine the relative uncertainty of torque,

$$\left(\frac{U_\tau}{\tau}\right)^2 = \left(\frac{U_m}{m}\right)^2 + \left(\frac{U_g}{g}\right)^2 + \left(\frac{U_r}{r}\right)^2 \tag{B.15}$$

The mass uncertainty was set to that of the scale used to measure the weights. The local gravitational acceleration was calculated from (NPL, 2010),

$$g = 9.780327(1 + A\sin^2(L) - B\sin^2(2L)) - 3.08610 - 6H \tag{B.16}$$

where A = 0.005 302 4, B = 0.000 005 8, L is the latitude, and H is the altitude in metres. For the mechanical engineering department of Stellenbosch University, $g = 9.79609 \pm 0.00015 m/s^2$, based on a 50 m latitude and a 0.01° altitude tolerance. The length of the moment arm was measured to within 2 mm.

The largest torque uncertainty of 0.39 N m was for the largest torque (201 N m). This uncertainty was used as the reference uncertainty.

Differential pressure transducers   A Betz Micromanometer 5000 was used to calibrate the differential pressure transducers (Δp_a & Δp_f). The pressure differential was calculated from the water density, gravitational acceleration, and the manometer's water level, which could be read to within 0.1 mm.

$$p = \rho g h \tag{B.17}$$

The reference uncertainty of this was determined from

$$\left(\frac{U_p}{p}\right)^2 = \left(\frac{U_\rho}{\rho}\right)^2 + \left(\frac{U_g}{g}\right)^2 + \left(\frac{U_h}{h}\right)^2 \tag{B.18}$$

The density was interpolated from water density data for varying temperature at one atmosphere. As an example, the density for a temperature of $18 \pm 2\,°\text{C}$ was calculated as $998.7 \pm 0.4\,\text{kg m}^{-3}$ (Moran and Shapiro, 1998). The gravitational accuracy calculated for the torque calibration was used in the above equation.

This resulted in an error up to 2.0 Pa for the range of pressures measured for both sensors. The calibration range for the fuel transducer was much smaller than the test range, however, the reading was only used to determine the propane flow-rate, the calculation of which was calibrated with a flow-meter.

Gauge pressure transducers   A Fluke 2700G-70M reference pressure gauge and P5514 hydraulic pressure comparator were used to calibrate the pressure transducers (p_{2x}, p_2, p_f & p_{oil}). The reference gauge had a range of 0.1 to 70 MPa, with an uncertainty of 7 kPa.

Thermocouples   A Fluke 9150 field metrology well was used for high temperature calibration, the temperature of which could be set between 150 and 1200 °C to within 5 °C. While a Fluke 9142 was used for low temperature calibration, with a temperature range of -25 to 150 °C, together with a RTD (resistance temperature detector). The combined measurement accuracy of the well and RTD was 0.065 °C for the test range.

It was necessary to calibrate the compressor outlet thermocouple (T_2) with both wells due to the compressor outlet temperature range. This resulted in an offset between the calibration trend lines produced with the two wells. The standard deviation error for the combined data sets was 4.4 °C, resulting in a regression uncertainty of 8.8 °C (see Table B.3). The standard deviation was considered the result of the inaccuracy of the high temperature well (5 °C), hence the offset trend lines. For this reason, the regression uncertainty was neglected, and rather the sensor and reference uncertainties were used (resulting in a combined uncertainty of 5.2 °C, as shown in Table B.3).

The high temperature calibration was limited by excessive noise on the readings. Small disturbances were noted at 650 °C, but higher than that and it became impossible to get a reasonable reading. For this reason, the exhaust thermocouples were only calibrated up to 650 °C. The metrology well would create more noise with increasing temperature (and hence power output). The noise would disappear if the temperature set-point of the well was lowered or if the well was switched off. When this was done, the thermocouple temperature would drop rapidly compared to the temperature displayed on the well, as its temperature sensor had greater insulation. Calibration under these conditions was unlikely to be accurate.

Furthermore, the thermocouples were connected to the PLC modules, which had built in filters. The resulting reading did not simply contain random noise, but had gradual and large stepped oscillations that appeared far removed from the true temperature. Perhaps related to the creation of a lower frequency beat from the interference of two waves with similar frequencies. A hand held data logger with a sampling rate of 1 Hz would record a stable reading, closely matched to the metrology well reading.

Fuel flow-meter   The fuel flow-rate was comprised of three t-pieces in the fuel line. The first (or most upstream) t-piece housed a thermocouple, and a flow restriction (or venturi) was inserted into the third t-piece. The differential pressure was measured across the second and third t-pieces, and gauge pressure was measured at the second t-piece. The following equations were used to calculate the mass flow-rate,

$$\dot{m} = C_d Y_a A_d \sqrt{\frac{2\rho_f \Delta p_f}{1 - \beta^4}} \qquad A_d = 0.25\pi d_f^2, \quad \beta = d_f/D_f \qquad \text{(B.19)}$$

The coefficient of discharge was determined from the calibration process; $C_d = 0.929 \pm 0.020$. A_d is the flow area of the venturi throat, and β is the ratio of the venturi throat diameter to the pipe diameter; where $d_f = 4.6\,\text{mm}$ and $D_f = 6.3\,\text{mm}$. Y_a is the compressibility factor, which accounts for the density variation through the venturi,

$$Y_a = \left[r^{2/\gamma} \left(\frac{\gamma}{\gamma - 1} \right) \left(\frac{1 - r^{(\gamma-1)/\gamma}}{1 - r} \right) \left(\frac{1 - \beta^4}{1 - \beta^4 r^{2/\gamma}} \right) \right]^{\frac{1}{2}} \qquad \text{(B.20)}$$

where r is the ratio of venturi to upstream pressure ($r = (p_f - \Delta p_f)/p_f$), and γ is the specific heat ratio. These equations were taken from Fluid Meters (1959). The fuel density ρ_f was determined from temperature and pressure measurements upstream of the venturi (T_f & p_f). Property data was interpolated to determine the density and specific heat ratio when calibrating

the flow-meter, and when measuring propane flow-rates. Otherwise for general measurements of air or LPG flow, the ideal gas law and constant specific heat ratios were used.

Initially two Festo flow sensors were used to calibrate the flow-meter (with compressed air). A Festo SFE1-LF-F200-HQ8 (flow sensor) was used for 0 to 200 SLPM, with an uncertainty of 3% + 1 SLPM. And a Festo MS6-SFE-F5-P2U-M12 was used for 200 to 406 SLPM, while having a span of 5000 SLPM and an uncertainty of 3% + 15 SLPM. The unit SLPM refers to a standard litre per minute, which is the equivalent volumetric flow-rate at 15 °C and 101.325 kPa.

The difference in flow-rate between either flow sensor and flow-meter, once calibrated, did not exceed more than 3%. However, at high flow-rates the calibration uncertainty was large, as it included the uncertainty of the second flow-meter (see Figure B.1). The flow sensors had not been calibrated recently, and their inaccuracy might have been greater than the product specifications.

Due to these limitations, the flow-meter was recalibrated with a venturi (DISA Type 55D41) that was used to calibrate hot wire anemometers. This is referred to as the DISA venturi to avoid confusion with the venturi used in the fuel flow-meter. Compressed air was used to calibrate the flow-meter, as was done with the earlier calibration.

Equation B.19 is also applicable to the DISA venturi. The coefficient of discharge is used to adjust for real flow conditions, where a C_d of 1 would be for ideal flow. The actual flow is reduced by friction and a vena contracta, which effectively reduces the flow area. A C_d was not listed in the DISA specifications, as it was only intended to measure the flow velocity at the centre of the venturi (on which the vena contracta will have little effect).

The coefficients of discharge depend on the Reynolds number and diameter ratio (β). The Reynolds number is either specified at the upstream pipe (Re_D) or at the venturi throat (Re_d). Modern venturi tubes have constant C_d values for $1.5 \times 10^5 < Re_D < 2.0 \times 10^6$ (White, 1988). Unfortunately, the fuel flow-meter was much smaller than the DISA venturi, and $2.7 \times 10^3 < Re_D < 10^4$ for the calibration process (where Re_D refers to the Reynolds number of the DISA upstream pipe). The DISA diameter ratio was $\beta = 0.2336$.

A C_d value of 0.95 ± 0.02 **was used for the DISA venturi.** This value covers the following range of values found in literature, applicable to the calibration Reynolds number. $C_d \in (0.95; 0.97)$ for various types of venturis (Herschel, Schoder, and Ledoux) and for $\beta \in (0.333; 0.5)$; taken from Fluid Meters (1959, Fig. 38). $C_d \in (0.937; 0.961)$ for smooth and sharp radius venturis with $\beta = 0.661$ (Hollingshead, 2011). And $C_d \in (0.936; 0.966)$ for a long radius

nozzle from the following equation (White, 1988),

$$C_d \approx 0.9965 - 0.00653 \beta^{\frac{1}{2}} (10^6 / Re_D)^{\frac{1}{2}} \tag{B.21}$$

The venturi equation (Equation B.19) was used to evaluate the uncertainty of the calibration. The ideal gas equation was used to determine the air density flowing through the DISA venturi, and so this equation was substituted into the venturi equation. The compressibility factor (Y_a) for the DISA remained between 0.99 and 1, so this term was omitted when evaluating the uncertainty,

$$\dot{m} = C_d A \sqrt{\frac{2\rho \Delta p}{1 - \beta^4}} \qquad A_d = \frac{\pi d^2}{4}, \quad \beta = \frac{d}{D}, \quad \rho = \frac{p_1}{R_a T_1} \tag{B.22}$$

$$\therefore \dot{m} = C_d \sqrt{\frac{(\pi^2/8) p_1 \Delta p}{(d^{-4} - D^{-4}) R_a T_1}} \tag{B.23}$$

$$\left(\frac{U_{\dot{m}}}{\dot{m}} \right)^2 = \left(\frac{U_{C_d}}{C_d} \right)^2 + \left(\frac{U_{p_1}}{2 p_1} \right)^2 + \left(\frac{U_{\Delta p}}{2 \Delta p} \right)^2$$
$$+ \left(\frac{d^{-5} U_d + D^{-5} U_D}{0.25 (d^{-4} - D^{-4})} \right)^2 + \left(\frac{U_{T_1}}{2 T_1} \right)^2 \tag{B.24}$$

The gauge pressure at the upstream pipe (p_1) and the differential pressure (Δp) were measured with the Betz Micromanometer, and their uncertainties were calculated in the same manner described for the differential pressure transducers. The ambient pressure (p_a) was measured with a mercury barometer, and was added to the gauge pressure reading. The absolute pressure uncertainty included the ambient pressure uncertainty,

$$U_{abs}^2 = U_{gauge}^2 + U_{ambient}^2 \tag{B.25}$$

The upstream pipe and venturi diameters were measured with telescopic gauges and a micrometer; $d = 14.00 \pm 0.02$ mm and $D = 59.94 \pm 0.02$ mm.

The calculated discharge coefficients for fuel flow-meter are plotted against the Reynolds number at the upstream pipe in Figure B.1. The coefficient uncertainties have been indicated with error-bars. The uncertainty with the DISA calibration (about 2.2 %) is primarily due to the uncertainty of its coefficient of discharge (2.1 %). The uncertainty with the Festo calibration is primary due to the rate accuracy of the flow-sensors; clearly the high flow sensor had greater uncertainty than the low flow sensor.

It is a bit concerning that the error-bars do not overlap at lower Reynolds number, as this may indicate the use of an incorrect discharge coefficient for
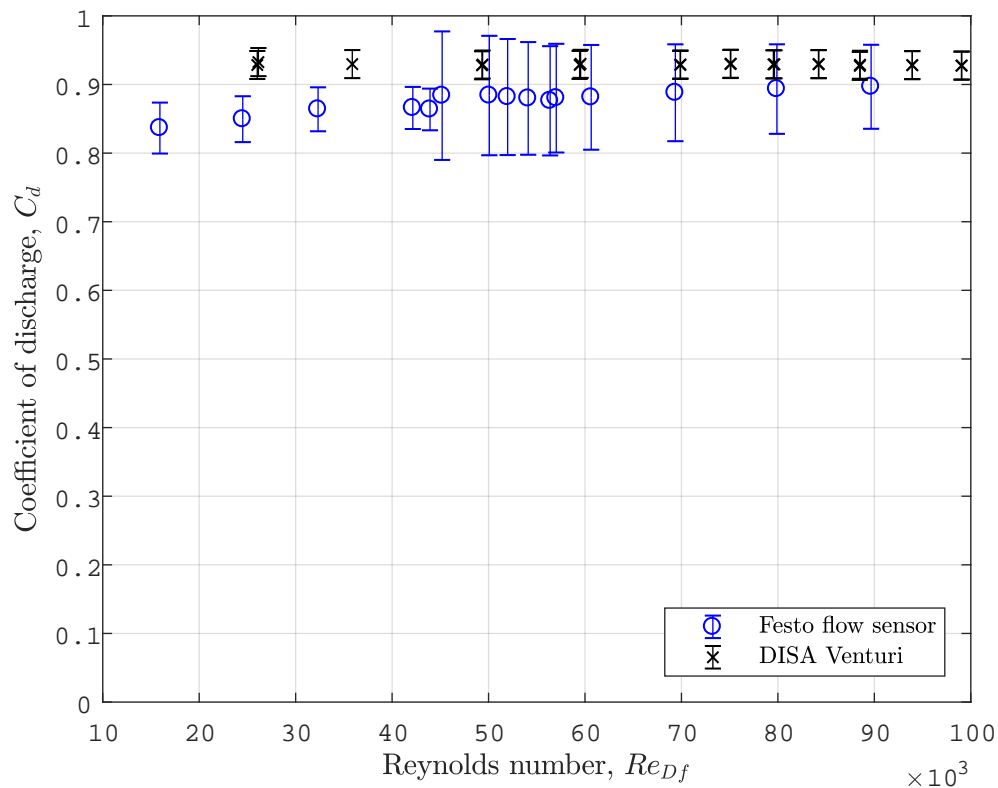
Figure B.1: Fuel flow-meter coefficient of discharge with error-bars

the DISA venturi. Although, without a calibration certificate for the Festo flow sensor, the DISA results at low flow may still be valid. The coefficients from the Festo calibration have an upward trend with Reynolds number, which is typical of venturis. While the DISA results remain fairly constant. This is partly due to assuming a constant C_d for the DISA venturi, while it would actually increase with flow (given the low DISA Reynolds numbers during calibration process).

Another uncertainty with the flow-meter, is that it was calibrated with air, while it was used with propane. The calibration with one fluid can be used for another fluid if the Mach and Reynolds numbers are similar (Fluid Meters, 1959). It was easier to calibrate the flow-meter at low pressure (compared to normal operation) when using the DISA venturi. In retrospect it would have been better if the flow-meter pressure during calibration was the same as normal operation or higher.

If the temperature and pressure were the same for calibration and operation, then the propane Mach number would be about 1.1 times that of air, and the propane Reynolds number 2.8 times that of air. The higher propane Reynolds

number for propane is due to its higher density. The actual operation to
calibration ratios are listed Table B.4.

Table B.4: Mach and Reynolds ratios between air and propane

Ratio of Propane to air			
Ma_D	Ma_d	Re_D	Re_d
0.82	0.85	2.92	1.86
0.38	0.37	1.45	0.73

B.4   Compressor intake pressure estimate

Barometric data and a pressure loss coefficient (for the air intake) were used
to estimate the compressor intake pressure. This improved the accuracy,
and reduced the uncertainty in the test data analysis. The intake pressure
estimate was used to correct the rated power to compare test data.

Barometric data from a Stellenbosch weather station were used as the am-
bient pressure for engine test data analysis (Stellenbosch University, [s.a.]).
The drop in pressure due to the ventilation system was measured as part of
investigating the high test cell temperatures. This was measured as 69 Pa
without the engine running. The drop in pressure with the engine running
was estimated to reach 97 Pa, assuming that all the exhaust gases exhaust
through the exhaust duct. However, this was not the case. Regardless, this
number was used as the barometric pressure uncertainty (0.1 kPa) as the
barometric data accuracy was unknown.

A couple of tests were run to measure the pressure loss across the air intake
duct and filters (Δp_i). The differential sensor used on the air flow-meter
was used to measure the pressure loss. A pressure loss coefficient K_L was
calculated from the data, and it was used to predict the pressure loss in other
tests.

Prinsloo (2008) designed and tested the intake duct, and used the throat of
the flow-meter as the reference area when calculating the loss coefficient.

$$\Delta p_i = K_L(\tfrac{1}{2}\rho v_t^2) = K_L(\tfrac{1}{2}\dot{m}^2/\rho A_t^2) \qquad \text{where } A_t = 0.25\pi d_t^2 \qquad (B.26)$$

The bracketed terms are the dynamic pressure, in terms of velocity and mass
flow-rate at the flow-meter throat, respectively. A_t is the throat area, and
$d_t = 0.11\,\text{m}$. As the flow-meter differential sensor was used to measure Δp_i,
a separate test was used to correlate the flow-meter differential pressure Δp_a
to the compressor outlet pressure p_2.

$$\Delta p_a = a p_2 \qquad\qquad\qquad\qquad (B.27)$$

where $a = (14.63 \pm 0.05) \times 10^{-3}$, p_2 is gauge pressure, and p_2 & Δp_a have the same units.

The Maintenance Manual (1967) states that the engine was intended to be run without filters, and the loss of performance was specified for a reduced compressor inlet pressure, relative to operating without filters. The inlet static pressure was not specified. Instead the ambient pressure was specified, which is equal to the inlet pressure stagnation (without filters). Thus the manual effectively specified the performance loss based on the total pressure loss.

The stagnation pressure loss was determined by calculating the dynamic pressure at the pressure measurement point, and subtracting it from the static pressure loss (ambient air assumed to be static).

$$\Delta p_{0i} = (p_a + \tfrac{1}{2}\rho v_a^{\cancel{2}}{}^0) - (p_i + \tfrac{1}{2}\rho v_i^2) = \Delta p_i - (\tfrac{1}{2}\dot{m}^2/\rho A_i^2) \tag{B.28}$$

where A_i is the cross-sectional area of the duct where the pressure was measured. The duct had a single intake, which split into two symmetrical ducts that was connected to opposite sides of the engine. At the measurement point, the duct was rectangular with internal dimensions of 199 x 72 mm. Thus $A_i = 2 \times (0.199 \times 0.072) = 0.0287\,\mathrm{m}^2$, which is about three times larger than the throat area ($A_t = 0.0095\,\mathrm{m}^2$).

Figure B.2 is a plot of the stagnation pressure drop versus the dynamic pressure (at the flow-meter throat) for a few steady operating points in the test. The data presented by Prinsloo has been reproduced in the figure, where the data from the current study has been labelled *Current*.

Prinsloo included plots with pressure loss, loss coefficient, and mass and volumetric flow-rates. These plots were used in this study to infer the density and dynamic pressure. Prinsloo tested at the CSIR in Pretoria, which has an altitude of about 1400 m. In this study, the ambient pressure was estimated as 85.6 kPa for that altitude (White, 1988, Table A.6). Ambient temperatures between 19.8 and 23.7 °C were calculated from the density and estimated pressure (using the ideal gas law for air), which seem plausible.

The loss coefficients are plotted against Reynolds number in Figure B.3, where $Re_t = 4\dot{m}/(\pi d_t \mu)$. A constant viscosity of $\mu = 1.885 \times 10^{-5}\,\mathrm{N\,s\,m^{-2}}$ was used to calculate the Reynolds number. This is the median viscosity for the temperature range of both data sets (20 to 50 °C), and does not differ by more than 4 % of the viscosity for that temperature range (Munson *et al.*, 2002, Table B.4).

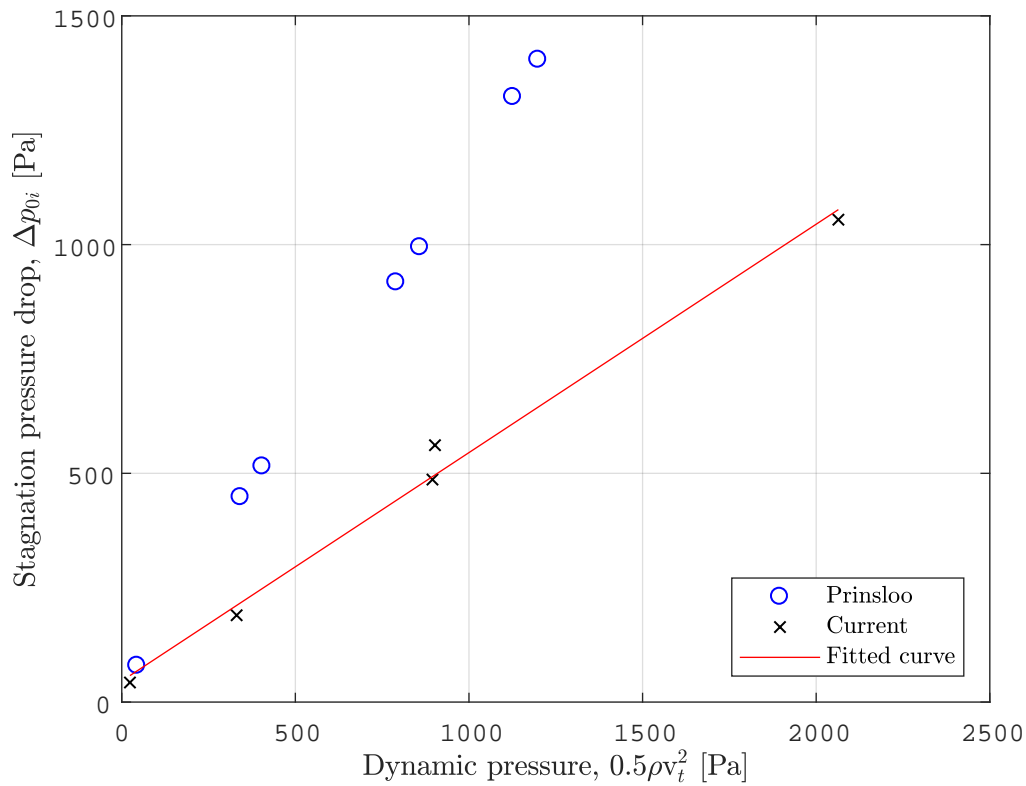The measured pressure drop was about half that measured by Prinsloo for

Figure B.2: Total intake pressure drop vs dynamic pressure

similar dynamic pressure or Reynolds number at the flow-meter throat. As the duct may have been changed slightly in the 10 years since Prinsloo reported his findings, the data obtained during this study was used instead of that reported by Prinsloo.

The coefficients from Prinsloo's data dropped with Reynolds number, until stabilising at 1.17 for $Re > 150 \times 10^3$ (refer to Figure B.3). Whereas the coefficients obtained in this study appeared constant, with one outlier at 50×10^3 Re. The average loss coefficient (excluding the first data point) was 0.56. The equation to the fitted curve in Figure B.2 was,

$$\Delta p_{0i} = a(\tfrac{1}{2}\dot{m}^2/\rho A_t^2) + b \qquad \text{where } a = 0.4992 \,\&\, b = 46.08\,\text{Pa} \qquad \text{(B.29)}$$

The gradient of the fitted curve differs slightly from the average loss coefficient, as the curve has a non-zero y-intercept. Both the average coefficient (*constant K_L*) and fitted curve (*variable K_L*) were used to calculate the pressure loss for the entire test (see Figure B.4), and the root mean square errors were 81.0 and 64.1 Pa for the averaged and fitted approaches, respectively. However, a large part of the error is due to the fluctuations of the intake
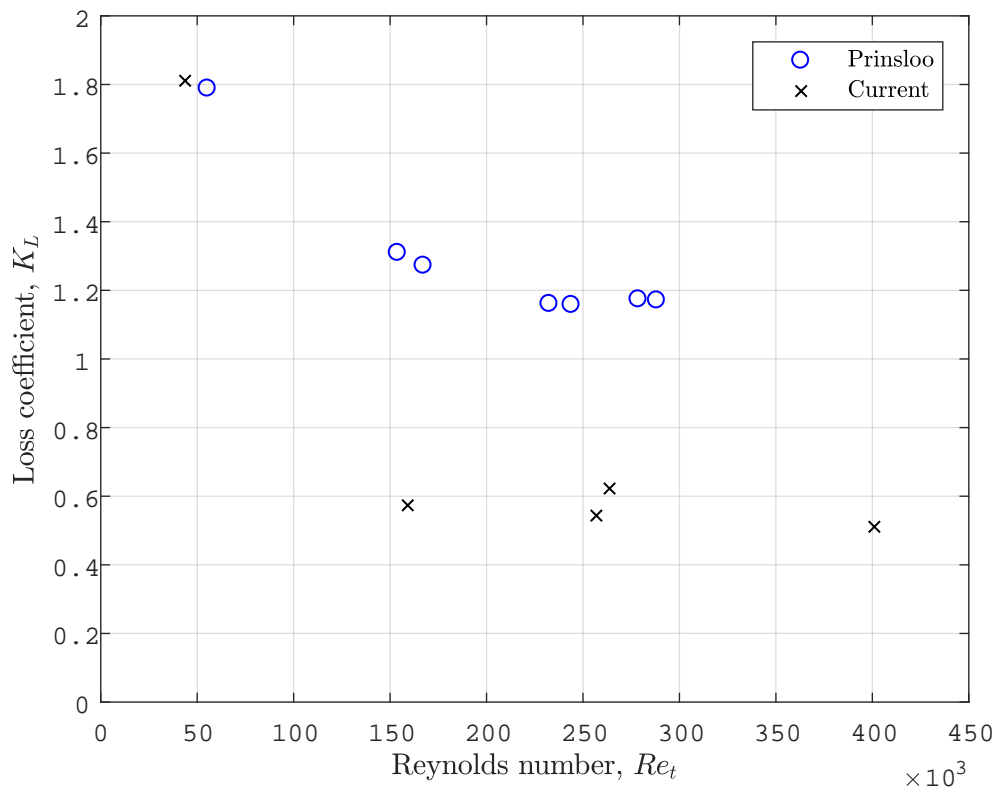
Figure B.3: Loss coefficient vs. Reynolds number

pressure compared to that of the compressor outlet pressure (which was used to determine the flow-rate). Given that the engine power is derated by 1 % for every 250 Pa drop in intake pressure, the errors seem negligible. Due to the smaller error, especially at higher speeds (and pressure drop), **the fitted curve was used to calculate the pressure drop in all test data analyses.**

B.5   Test results

Table B.5 is a sample of the key measured and calculated parameters, obtained from engine tests. The average and the standard deviation for a two second time interval are shown, together with the typical values listed in the Rover documentation. The on-load data was taken from the time interval when the peak power was produced, while the no-load data is typical of the engine running at top speed. Both data sets are for propane tests. Table 6.2 is a truncated version.
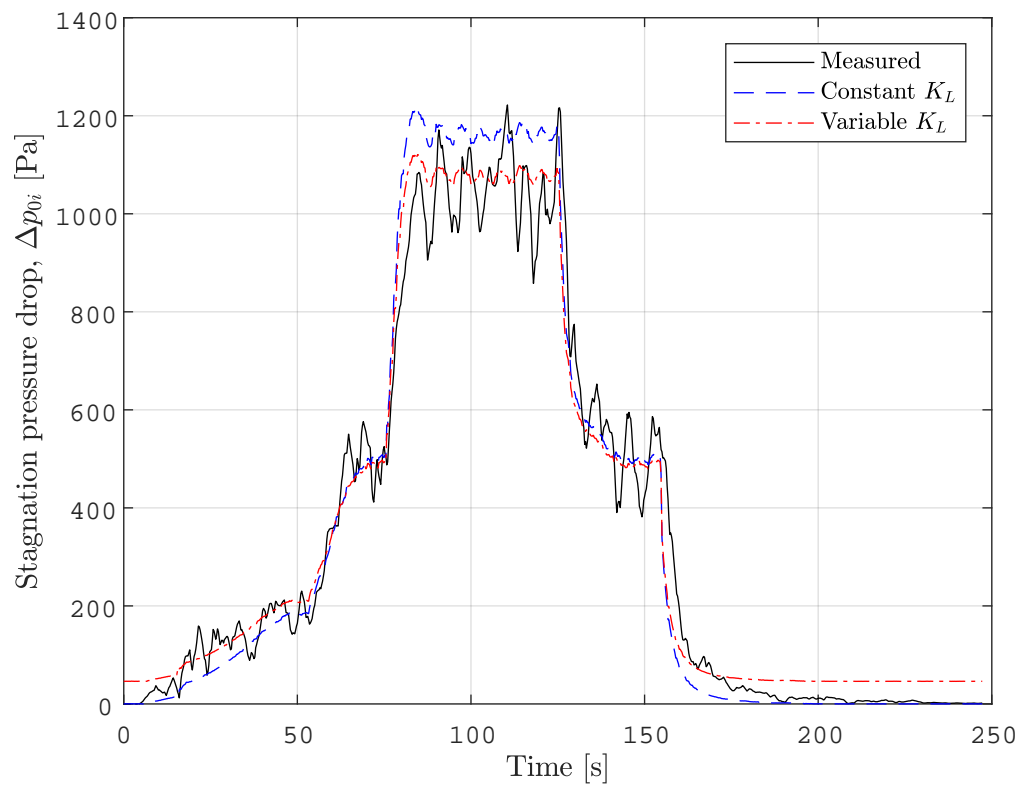
Figure B.4: Measured vs calculated intake pressure drop

Table B.5: Analysis results

Var	Units	On-load Mean	On-load Std dev	On-load Typical	No-load Mean	No-load Std dev	No-load Typical
n	kRPM	45.2	±1.8	45.5 to 46.5	47.2	±0	46.7 to 47.3
T_1	°C	37.3	±0.2	-55 to 50	37.8	±0.2	-55 to 50
T_2	°C	285	±0.3		229	±0.8	
T_2'	°C	154	±0.7		136	±0.2	
T_3	°C	920	±3		636	±1	
T_4	°C	663	±0.6	< 610	471	±0.4	< 400
T_4'	°C	629	±3.1		443	±0.9	
ΔT_4	°C	72	±0.3	< 150	87	±0.4	< 150
p_a	kPa	100.0		58 to 101	101.5		58 to 101
Δp_i	kPa	1.2	±0.09	0 to 0.5	1.2	±0.03	0 to 0.5
p_2	kPa	202	±1.4	179 to 214	160	±0.5	179 to 214
r		3.1	±0.02		2.6	±0.00	
$\dot{W}$	kW	34.4	±1.8	0 to 44.74	-0.2	±0.0	0
$\dot{W}_c$	kW	171	±6		130	±2	
$\dot{W}_t$	kW	205	±5		130	±2	
$\dot{Q}_{in}$	kW	530	±0.9		357	±0.4	
$\dot{Q}_{in,calc}$	kW	537	±17		342	±5	
$\dot{m}_a$	kg/s	0.686	±0.025	0.603	0.678	±0.009	0.603
$\dot{m}_f$	kg/h	41.5	±0.07		28.0	±0.03	
$\dot{m}_{f,calc}$	kg/h	42.1	±1.3		26.8	±0.4	
p_f	kPa	577	±0.7		399	±0.3	
T_f	°C	7.3	±0.1		12.5	±0.0	
SFC	kg/kW h	1.2	±0.1		N/A	±1.4	
η	%	6.5	±0.3		-0.1	±0.0	
η_c	%	47	±0.3		51	±0.3	
η_t	%	88	±1		86	±0.3	
T_{oil}	°C	95	±0.2	< 110	52	±0.3	< 110
p_{oil}	kPa	138	±0.4	110 to 124	167	±0.8	124

All pressures are gauge except for p_a.

C. Detailed Recommendations

C.1   LPG/propane vaporiser

The control system was designed for an absolute supply pressure of 600 kPa, which is the vapour pressure of propane at 8 °C. Daytime temperatures in Stellenbosch are seldom below this value (Stellenbosch University, [s.a.]), and an excess of pressure was expected. Although the cylinder temperature and pressure were expected to drop rapidly once the liquid level in the cylinders got low.

However, in midwinter the cylinder pressures were only about 600 kPa prior to any test runs, during which the pressure dropped further. The cylinders were sheltered from direct sunlight and stored outside in an alleyway that is mostly in shade. As a result the cylinders were slow to warm up from night-time temperatures, and remained below the average ambient temperature.

The rapid temperature drop due to low liquid levels was overcome by placing the cylinder in containers of water. The water was warmed on particularly cold days. It was not ideal to remove the cylinders at the end of each day, due their size and enclosure; and leaving the cylinders in the containers will increase the rate of corrosion.

A *vaporiser* would be a better solution for prolonged use of propane/LPG. Liquid fuel is supplied to a vaporiser, which evaporates the fuel. The only evaporation occurring within the cylinder is that required to displace the volume of the consumed liquid. The propane cylinders would work with a vaporiser, because they had two outlet valves; one to supply vapour, and the other liquid.

Autogas vaporisers were typically well priced, but their outlet pressure is too low for the Rover gas turbine. An industrial vaporiser was found, but the capital cost was large, as shown in the following table. A quote was obtained from ADCENG for the industrial vaporiser, otherwise the information was taken from the LPG Shop ([s.a.]) and ADCENG Gas Equipment ([s.a.]).

Type	Model	Capacity	Outlet Pressure	Price
Autogas	ALEX Shark 1500	$\approx$ 30 kg/h	2.5 bar	R1300
Industrial	ADCENG 30E	30 kg/h	17 bar	R50 000

C.2   Proportional valve

The greatest limitation with the final fuel control system was that the venturis were sized for a particular supply pressure. If the propane cylinder pressure dropped, or if the regulator setting was changed, then the flow-rate for all valve combinations would be affected.

Whereas the position of a metering/proportional valve can be adjusted to correct limited supply pressure variations. A proportional valve would be a good choice if the system is to be automated. Several proportional valves were found that would suit the flow and pressure requirements of the system. However, only one of them was rated for propane (and methane).

The valve was very expensive compared to the solenoid valves, so instead the solenoid network was used. However, if the control system is to automated, then a proportional valve, or metering valve with an actuator, would be ideal. Samson Controls (Pty) Ltd provided a quote for a suitable proportional valve, and the OMB Star valves were ordered from the LPG Shop ([s.a.]).

Description	Price
OMB Star 6 mm solenoid valve (for five valves)	R1157
Samson proportional valve (type 3241)	R27 309

C.3   Speed and power measurement error

The engine speed was measured with a hall sensor that sensed the passing of a toothed wheel on the dynamometer shaft. The signal from the speed sensor was interpreted by an frequency to analogue converter in the dynamometer controller. The controller output an analogue signal to the PLC, which would digitised the analogue output.

A single test was run with a secondary device to obtain a speed measurement that was independent of the dynamometer controller and PLC. It was connected to a DAQ (data acquisition device), that would determine the speed from the interval between the voltage pulses. This was a more direct measurement of the speed, and was considered more accurate.

The speeds were found to closely match while no load was applied, but once load was applied both signals were affected by electrical noise and their averaged values began to diverge. This was only tested up to about 20 kW of brake power, where the secondary measurement was found to be 10 to 15 % higher than that of the original measurement. This suggests that the calculated power was undervalued by the same percentage. This problem was only quantified (with the secondary measurement) towards the end of

the project, and there was no time left to address the issue.

It is recommended that the noise is filtered from the signal before it reaches the dynamometer controller, because the noise could affect the speed regulation (applied load). Alternatively a secondary device should be used to measure to the engine speed, so that the data is more accurate.

C.4   Unrepresentative measurement of the compressor outlet temperature

A thermocouple was fixed to the main air casing to measure the compressor outlet temperature T_2. The casing housed the inner volute, through which the combustion gases flow to the turbine. As such the sensor and casing were exposed to radiation from the hot volute, and these heat sources may result in a reading that is higher than the air temperature that should be measured.

If the air is significantly warmed by the hot surfaces, then the measurement might be closer to the air temperature. However, the value will not be representative of the compressor outlet temperature. If this concern is valid, then the calculated compressor work will be too high, and the calculated compressor efficiency too low. The calculated work done by the turbine, and its efficiency, will also be too high.

The compressor efficiency η_c in Figure C.1 remains below 50 % (excluding the spikes). The engine speed was about 46 500 RPM for the highest pressure plateau. The efficiencies for the on-load and no-load data in Table 6.2 are 48 and 52 %, respectively. The same data, apart from T_2, were used in the comparative analysis (Section 5.1.1), and the calculated efficiencies were 87 and 67 %, respectively. Luiten (2015) ran a CFD model of the Rover compressor at 46 000 RPM, and calculated a 63.8 % efficiency.

The efficiencies in the sixties were considered to be realistic, while the test data efficiencies were regarded as too low. The high values from the comparative analysis are due to the limitations of the compressor temperature rise approximation (Equation 2.24).

The temperature measurement was also seen to have higher lag than other sensors. This is illustrated by Figure C.1, where after 100 seconds, and again after 175 seconds, the compressor pressure has stabilised while the temperature is still rising. T_2 stabilised towards the end of the first pressure plateau, but not the second. At times data intervals were analysed where T_2 had not stabilised.

If the turbine inlet temperature T_3 had been measured, then the accuracy
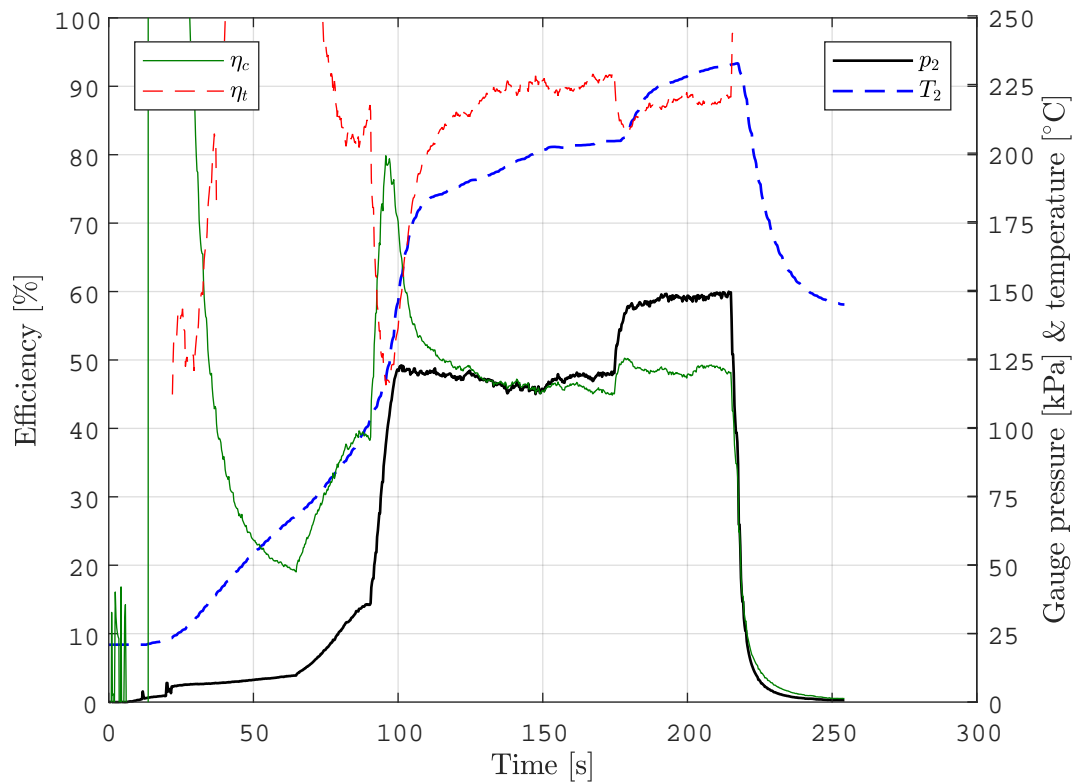
Figure C.1: Slow response time of compressor outlet temperature

of T_2 would have been relevant in assessing the temperature rise across the combustor, and hence the combustion efficiency. However, T_2 was used to estimate T_3, and the compressor and turbine efficiencies. The temperatures were also used as a CFD boundary condition.

C.5   Oil cooler fan

An NDM oil cooler was connected to the engine. A spare blower fan was available to be used with the oil cooler, but its specifications were unknown. The fan was used to determine whether it would meet the requirements. Engine tests were limited by excessive air intake temperatures, rather than the oil becoming too hot. However, it was noted during an on-load test that the oil temperature reached 100 °C, and was still climbing.

If the test cell ventilation is improved such that continuous on-load tests can be run, then the fan will need to be upgraded. Although, if the room temperatures are reduced, then the oil cooler will become more effective. The following calculations were used to specify a suitable fan.

The Overhaul Manual (1972) recommends an oil cooler with a minimum heat transfer rate of 2.93 kW (5550 CHU/h). Performance curves for an Airflow Systems AS-2006X oil cooler were found. The oil cooler was of a similar construction and size as the NDM oil cooler, except for its length being only 80 % of the NDM cooler (Airflow Systems, 2008).

The oil flow-rate of the Rover engine was unknown, so the lower oil flow-rate performance curve was used. The lowest performance point of the oil cooler was 3.3 kW (190 BTU/min) for an oil flow-rate of 15.88 kg/min, air flow-rate of 0.0756 kg/s with a 250 Pa pressure drop across the oil cooler, and an initial temperature difference of 55.6 °C between the air and oil (Airflow Systems, [s.a.]). Thus if the flow-rates can be achieved, then the oil temperature can be kept at 100 °C for an ambient temperature up to 44 °C, with a slightly smaller oil cooler than the one installed, and at a higher heat transfer rate than required.

A blower fan was found that could deliver 350 m^3/h (or 0.1 kg/s assuming air at 44 °C & 1 atm) with a pressure increase of 250 Pa with a price tag of R5995.50. Manufacturer ebm-papst Mulfingen GmbH & Co. KG, part number D2E133-AM47-01, RS stock code 826-1118 (RS Components, [s.a.]).

C.6   Test cell ventilation and flue

Engine inlet temperatures often reached critical levels and required test abortion. Air was extracted from the test cell with fans, while fresh air was drawn into the room through vents by the lower room pressure (compared to outside). The engine would exhaust into a flue, or duct, that would channel the flow outside. There was a gap between the jet pipe of the engine and the flue. If the extractor fans were on, and the engine was not running, then there would be back-flow through the flue due to the lower room pressure. On start up the engine would have to overcome this draught/back pressure. On shut down, the hot gases in the flue would be drawn back into the room, and flow over the engine.

When the engine ran, not all of the exhaust gases would enter the flue, and a portion was seen to overflow the flue inlet. At low speed (about 20 kRPM), the ventilation system could keep up with overflow. At higher speeds (about 30 to 40 kRPM), the overflow became excessive and the room temperature would rise. The problem appeared to go away at top speed (46 kRPM), but as load and fuel was increased, the room temperature would rise until the limit was reached (50 °C).

There was a significant gap between the engine outlet and the flue inlet (about 15 cm), and fresh air entering the room through a vent would flow

directly towards this gap. The cross flow was potentially blowing some of the exhaust stream off its course, and into the room.

A screen was placed in front of the vent to shield the exhaust stream, and direct the fresh air towards the engine inlet. At certain engine speeds, there may have been an improvement, but in general the room temperatures were still getting too high. With the screen in place, it was more apparent how the exhaust would choke in the flue inlet. The inlet was conical, with the entrance larger than the engine jet pipe. The exhaust jet flowed into the centre of the inlet cone, while a portion would reverse in the outer region, resulting in an annular back-flow across the engine. The screen only blocked the fresh air from flowing over the engine and blowing the back-flow away. Plastic tubing and wire sheaths melted. It also made the moment the engine stopped worse, as exhaust fumes were drawn back down the flue and into the test cell.

The flue inlet was moved closer to the engine, such that it enclosed the edge of the jet pipe. Although it appeared as though more exhaust gases were exhausted through the flue (the duct insulation appeared to smoulder more), the back-flow was better directed towards the engine and instrumentation, and better protected from the fresh air stream. Again some plastic tubing and wire sheaths were damaged.

The flue was inspected for obstruction, and found to be clear and clean. The room pressure was measured without the engine running, and the vacuum was small compared with the dynamic pressure of the exhaust flow. The vacuum would depend on the number of extractor fans that were used, and was measured to be between 33 and 76 Pa (without the engine running). Whereas the dynamic pressure of the exhaust was calculated to be 1.6 kPa for standard operation (0.603 kg/s at 580 °C). Refer to Table 5.2.

The flow resistance through the duct is more significant than the partial vacuum of the test cell. The exhaust velocity is not effectively slowed down as it enters the duct, losing some dynamic pressure. The rain cover on the flue outlet will create a significant pressure loss too, and might reduce the beneficial buoyancy effect.

A very simple assessment was made to quantify the effect. After the duct inlet (conical section) the flow area remains mostly constant. Neglecting heat losses, which would reduce the volumetric flow-rate along the duct, the velocity (v) will remain constant. The pressure difference between the end/throat of the inlet (point 1) and at the flue outlet (point 2) will be,

$$\Delta p_{12} = 0.5\rho v^2(fL/D + K_L) \tag{C.1}$$

Where f is the friction factor, L is the duct length, D the flue diameter, and K_L

the loss coefficient. The friction factor was determined from the Colebrook equation (Munson *et al.*, 2002),

$$1/\sqrt{f} = -2.0 \log \left(\frac{\epsilon}{D_2/3.7} + \frac{2.51}{Re\sqrt{f}} \right) \text{ where } Re = \rho v D / \mu \qquad \text{(C.2)}$$

The loss coefficient was approximated as 3.5; which includes 0.5 for the expansion from the jet pipe in the duct, plus 0.4 for each of the 5 elbows, plus 1 for the restriction at the flue outlet. The flue roughness ϵ was assumed to be 9 mm, which was listed as the upper limit for riveted steel (Munson *et al.*, 2002, Table 8.1). The flue cross-sectional area was 0.054 m^2, and its length was roughly 15 m.

For an exhaust flow of 0.603 kg/s at 580 °C, the resulting back pressure would be 1.1 kPa, which is 69 % of the dynamic pressure in the jet pipe for the same flow. While the calculation is simple, it does indicate that the actual problem was excessive flow resistance of the duct, and the lower room pressures are less significant when the engine is at top speed.

The most certain way of addressing the problem would be to increase the flue diameter, or to add an extractor fan, suitable for high temperature, into the flue.

C.7 Method to stop compression fitting leaks

A serious installation difficulty was the elimination of leaks in fittings. Copper pipes and brass compression fittings were used to construct the valve flow network, or manifold. A nut gets tightened onto the body of the compression fitting, and together they compress a ferrule onto the pipe. (see Figure C.2).
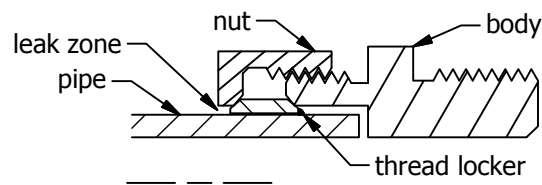

Figure C.2: Compression fitting

The seal of compression fittings was found to be affected by slight misalignment of the pipe and fitting. This proved to be problematic given the close valve proximity, and hence short connecting pipes that were too rigid to compensate for the misalignment. The problem was exacerbated by mounting the valves on a support plate, where misalignment of one fitting could apply

bending moments on several other fittings. It was essential to minimise the torque and bending moments applied to pipes while tightening fittings.

Some leaks were eliminated by wrapping the ferrules in thread tape. However, correcting one leak, often resulted in leaks in other fittings. Ultimately the threaded fittings were considered unsuitable for the manifold. However they worked well where the connecting pipe was longer, such as between the injector and flow-meter.

After discarding two manifolds constructed with compression fittings, the fittings were changed to capillary (or solder) fittings. Compression fitting were still used between the valves and pipes. The capillary fittings should remain leak free, even if the flow network is stripped and then reassembled (excluding the capillary fittings). The change to the capillary fittings was effective.

Once the switch to capillary fittings was made, a technique was found to address the leaks on the few remaining compression fittings. It was reasoned that the leaks were most likely occurring between the ferrule and pipe, since there was line contact between the ferrule and fitting (body and nut), while surface contact between the ferrule and pipe. Leaks were also observed between the nut and pipe, and not between the threads. The addition of thread tape would aid the ferrule-fitting seal, but would do little to aid the seal between the pipe and ferrule. It was found that adding a drop of thread locker to the pressurised pipe-ferrule gap stopped these leaks (see Figure C.2).

D. CFD Literature Review

The following is a summary of the information that was used to set up the CFD simulation. The information was taken from Fluent User's Guide (2017), unless stated otherwise.

D.1   Solver

Fluent can either use a pressure or density based solver. Traditionally the pressure based solver was for incompressible or mildly compressible flows, while the density based solver was for high-speed compressible flow. However, both solvers are now applicable for a wide range of flows (from incompressible to highly compressible). The density based solver may be more accurate for shock resolution.

Some physical models are limited to one solver, and the solver choice will most probably be based on this limitation. For example the combustion models are limited to the pressure based solver. The solvers use different algorithms to link the flow and pressure. Pressure based algorithms:
  • coupled; faster convergence
  • segregated; requires less memory

Density based formulations:
  • implicit; faster convergence
  • explicit; requires less memory

D.2   Spacial discretisation

Available options:
  • Green-Gauss cell based
  • Green-Gauss node based
  • Least squares cell based (recommended option)

Green-Gauss cell based requires the least amount of computation, but is less accurate than the other schemes (particularly for irregular grids). Green-Gauss node based and least squares cell based can maintain second order accuracy for irregular grids (skew or distorted), but least squares cell based is faster than Green-Gauss node based.

D.3 Turbulence models

Turbulence can be modelled with Direct Numerical Simulation (DNS), Large Eddy Simulation (LES), or Reynolds Average Navier-Stokes Simulation (RANS). DNS and LES models are much more computationally intense than RANS models. RANS suitable when the effects, rather than the details, of turbulence are required. LES and DNS are too demanding for the level of detail required for this project, and are not discussed further.

RANS models effectively filter turbulence out of the Navier-Stokes equation, by taking the time average of the equations. Additional equations are introduced to model the affects of turbulence.

The k-ω and the k-ϵ models are popular two-equation models. They fall into the Eddy Viscosity Model (EVM) category, where the viscosity is increased with eddies/turbulence.

k-ϵ works well away from boundary surfaces. Wall functions are used to model the boundary layer. Wall cells should lie in the log-layer, with a y+ value of 30 to 300. For higher Reynolds numbers, y+ can be on the larger end of the range. For very low Reynolds numbers, but still turbulent, wall functions might not be valid as the real log-layer may be too small.

k-ω is superior for modelling the boundary layer, and is recommended where boundary layer accuracy is critical (e.g. flow separation and heat transfer). To achieve higher accuracy, the viscous sub-layer needs to be resolved. This requires the first cell to have a y+ value of about 1. A Prism layer with growth rate no higher than about 1.2 is recommended.

If the mesh is too coarse near the wall, with the first cell occurring in the log-layer, then the k-ω model will apply wall functions. This will negate the benefit of the k-ω model, and it would preferable to use the k-ϵ model.

SST k-ω and Realizable k-ϵ are recommended for standard cases. The standard k-ϵ is fine for crude turbulence modelling. SST k-ω is preferred choice for accurate boundary layer effects (e.g. heat transfer).

The Realizable variant is better than the standard k-ϵ, as it is less dependent on the boundary cell thickness. Mesh independence is more easily achieved with the Realizable variant.

The Shear Stress Transport (SST) model is accurate at predicting turbulence transportation and flow separation. This is achieved by blending k-ω near the wall, and k-ϵ away from the wall, as this is where the strengths of the respective models lie.

The standard two-equation models tend to produce excessive turbulence energy near stagnation points. This problem can be compensated for by using the production limiter option, which limits the production of turbulence in the turbulence equations. This option is on by default.

Two-equation models fail to accurately model flows with significant swirl. This is because these models are limited to isotropic turbulence, while the Reynolds stresses become anisotropic in swirling flows.

The Reynolds Stress Model (RSM) is recommended for swirl dominant flow (e.g. a cyclone), as the model allows for anisotropic turbulence. The model consists of seven equations, as is thus more computationally intense than two equation models. Unfortunately the model is also prone to divergence.

The Spallart-Almaras model (a one equation model) is effective for external flow, and is often used in aerodynamic modelling. It is not useful for modelling internal flow, as was done in this project.

List of References

Abdullah, S., Mahmood, W.M.F.W., Aljamali, S. and Shamsudeen, A. (2017). Compressed natural gas direct injection: Comparison between homogeneous and stratified combustion. In: Al-Megren, H. (ed.), *Advances in Natural Gas Emerging Technologies*, chap. 7. InTech, Rijeka.
Available at: `https://doi.org/10.5772/67336`

ADCENG Gas Equipment ([sa]). Adceng lpg vapourisers: Product information. [Online]. Available: `https://www.adceng.co.za/lpg-nh3-equipment/vapourisers/71-adceng-lpg-vapourisers/39-product-information.html` [2018, November 16].

Afrox (2016). *Product Reference Manual*, 7th edn.
Available at: `http://www.afrox.co.za/en/customer_service/publications/product_reference_manual/index.html`

Airflow Systems (2008). X-series drawings. [Online]. Available: `http://www.airflow-systems.com` [2018, February 6].

Airflow Systems ([sa]). X-series oil cooler competition performance chart. [Online]. Available: `http://www.airflow-systems.com` [2018, February 6].

Ariztegui, J., Gutierrez, J., Fürhapter, A. and Friedl, H. (2015 Oct). LPG Fuel Direct Injection for Turbocharged Gasoline Engines. *MTZ worldwide*, vol. 76, no. 10, pp. 10–15. ISSN 2192-9114.
Available at: `https://doi.org/10.1007/s38313-015-0052-4`

Bejan, A. (1996). *Entropy Generation Minimization*. CRC Press.

Biogas (2013). An introduction. Tech. Rep. 329, Fachagentur Nachwachsende Rohstoffe e.V. (FNR). 3rd edn.

Boyce, M.P. (2006). *Gas Turbine Engineering Handbook*. 3rd edn. Gulf Professional Publishing.

Brown, T.L., LeMay, H.E., Bursten, B.E. and Burdge, J.R. (2003). *Chemistry - The Central Science*. 9th edn. Prentice Hall.

Cho, J.H., Yang, J., Kim, D.Y. and Kim, H.-C. (2009 April). Maximized Values of LNG Specifications in the LNG Industry: Producer and Buyer Perspectives. In: *9th Topical Conference on Gas Utilization*. Tampa, Florida.

123

Coleman, H.W. and Steele, W.G. (1999). *Experimentation and Uncertainty Analysis for Engineers*. 2nd edn. John Wiley & Sons, Inc.

Department of Energy (2017). *2016 South African Energy Price Report*, 9th edn. Available: `http://www.energy.gov.za/files/media/explained/Energy-Price-Report-2016.pdf` [2018, May 25].

Department of Energy (2018). Latest fuel prices. [Online]. Available: `http://www.energy.gov.za/files/esources/petroleum/petroleum_fuelprices.html` [2018, May 25].

Engine Catalogue ([sa]). *Single Shaft*. Rover Gas Turbines Limited. Publication no. SP100, Issue 2.

ESCAP (1993). *Guidelines for Conversion of Diesel Buses to Compressed Natural Gas*. Economic and Social Commission for Asia and the Pacific, United Nations. ST/ESCAP/1361.

ExxonMobil ([sa]). Exxonmobil jet fuel. [Online]. Available: `https://www.mobil.com/English-GB/Commercial-Fuel/pds/GLXXJetFuel-Series?p=1` [2018, January 10].

Fluent User's Guide (2017). *ANSYS*. Release 18.1.

Fluid Meters (1959). *Their Theory and Application*. 5th edn. The American Society of Mechanical Engineers.

Hollingshead, C.L. (2011). *Discharge Coefficient Performance of Venturi, Standard Concentric Orifice Plate, V-Cone, and Wedge Flow Meters at Small Reynolds Numbers*. Master's thesis, Utah State University.

Homann, C. (2015). *Effects of Solar Hybridization on the Performance of a Gas Turbine*. Master's thesis, Stellenbosch University.

Introduction to ANSYS Fluent (2016). *Training manual*. Release 17.0.

Jayasuriya, J. and Manrique, A. (2005). Gas turbine combustor lab exercise. Laboratory Notes, Kungliga Tekniska Högskolan.

Kröger, D.G. (2012). The stellenbosch university solar power thermodynamic cycle. Available: `http://sterg.sun.ac.za/wp-content/uploads/2012/10/SUNSPOT_July_20121.pdf` [2018, September 25].

Kurz, R.X. and Mokhatab, S. (2012 June). Important properties for industrial gas turbine fuels. *Pipeline & Gas Journal*, vol. 239, no. 6, pp. 28–32. Available: `https://pgjonline.com/magazine/2012/june-2012-vol-239-no-6/features/important-properties-for-industrial-gas-turbine-fuels` [2018, May 23].

Lefebvre, A.W. (1983). *Gas Turbine Combustion*. McGraw-Hill.

LPG Shop ([sa]). Alex shark 1500 reducer 200hp. [Online]. Available: `https://www.lpgshop.co.uk/alex-shark-1500-reducer-200hp/` [2018, November 16].

Luiten, R.V. (2015). *Performance Improvement of the Rover 1S/60 Gas Turbine Compressor*. Master's thesis, Stellenbosch University.

Maintenance Manual (1967). *Engines Type 1S/60 & 1S/90*. Rover Gas Turbines Limited.

Meyers, B.C. (2009). *The Experimental Flowfield and Thermal Measurements in an Experimental Can-Type Gas Turbine Combustor*. Master's thesis, University of Pretoria.

Miller, D.S. (1984). *Compressible Internal Flow (BHRA fluid engineering series)*. British Hydromechanics Research Association. ISBN 0906085918.

Miller, D.S. (1990). *Internal Flow Systems*. 2nd edn. British Hydromechanics Research Association. ISBN 0-947711-77-5.

Moran, M.J. and Shapiro, H.N. (1998). *Fundamentals of Engineering Thermodynamics*. 3rd edn. Wiley. ISBN 0-471-97960-0.

Munson, B.R., Young, D.F. and Okiishi, T.H. (2002). *Fundamentals of Fluid Mechanics*. 4th edn. Wiley.

NPL (2010). How can i determine my local values of gravitational acceleration and altitude? [Online]. Available: `http://http://www.npl.co.uk/reference/faqs/` [2018, February 17].

Overhaul Manual (1972). *Engines Type 1S/60 & 1S/90*. Rover Gas Turbines Limited.

Perry, R.H. and Green, D.W. (2008). *Perry's Chemical Engineers' Handbook*. 8th edn. McGraw-Hill.

Prinsloo, L. (2008). *The Commissioning of the Rover 1S/6 Gas Turbine*. Undergraduate research, University of Pretoria.

Quarta, N.J. (2012). *Simulation of a Hybridised Solar Gas Turbine System*. Master's thesis, University of the Witwatersrand.

RS Components ([sa]). Centrifugal blower. [Online]. Available: `https://za.rs-online.com/web/p/blowers/8261118/` [2018, February 6].

Saravanamuttoo, H.I., Rogers, G.F., Cohen, H. and Straznicky, P.V. (2009). *Gas Turbine Theory*. 6th edn. Pearson Education Limited.

Shell (2003). The aeroshell book. [Online]. Available: `https://www.shell.com/aviation` [2018, January 10].

Staffell, I. (2011). The energy and fuel data sheet. Available: `http://www.claverton-energy.com/wordpress/wp-content/uploads/2012/08/the_energy_and_fuel_data_sheet1.pdf` [2018, March 19].

Stellenbosch University ([sa]). Weather data. [Online]. Available: `http://weather.sun.ac.za` [2018, September 11].

Versteeg, H.K. and Malalasekera, W. (2007). *An Introduction to Computational Fluid Dynamics, the Finite Volume Method*. 2nd edn. Pearson Education.

White, F.M. (1988). *Fluid Mechanics*. 2nd edn. McGraw-Hill.

Zhang, Y. (2016). *Pre-Study for conversion of a gas turbine from liquid to gaseous fuel*. Master's thesis, Stellenbosch University.